The role of the tumor microenvironment in the progression of desmoplastic cancers in subcutaneous and orthotopic injection models

Institute of Translational Immunology

Inaugural Dissertation

to obtain the academic degree

Doctor of Natural Sciences (Dr. rer. nat.)

submitted to the Department of Biology

of Johannes Gutenberg-University Mainz

by

Emma Eichler

born on October 19, 1992 in Tumen, Russia

Date of submission: April 15, 2025

Dean: Prof. Dr. Eckhard Thines

1. Referee: Prof. Dr. Dr. Detlef Schuppan

2. Referee: Prof. Dr. Walter Stöcker

Date of oral examination:

Table of Contents

Abbreviations

%	
%	Percent
µ	
µ	Micro
4	
4E-BP1	eIF4E-Binding Protein 1
4-MU	4-Methylumbelliferone
7	
7-AAD	7-amino-actinomycin D
A	
ACT	Adoptive cell transfer
ADFs	Adipocyte-derived fibroblasts
ADM	Acinar-to-ductal metaplasia
Akt	Protein kinase B
ALAT	Alanine aminotransferase
ALD	Alcohol-associated liver disease
ALK	Anaplastic lymphoma kinase
α-SMA	Alpha-amooth muscle actin
AP-1	Activator protein-1
ASAT	Aspartate aminotransferase
ASOs	Antisense oligonucleotides
B	
BCA	Bicinchoninic acid
BM-MSCs	Bone marrow-derived MSCs
bp	Base pair
BRAF	B-Raf proto-oncogene
BSA	Bovine serum albumin
bZIP	Basic-region leucine zipper
C	
CCL	Chemokine (C-C motif) ligand

CD	Cluster of differentiation
CDKN2A	Cyclin-dependent kinase inhibitor 2A
CO_2	Carbon dioxide
Col1a1	Collagen type I alpha 1 chain
Col3a1	Collagen type III alpha 1 chain
CTGF	Connective tissue growth factor
CTL	Cytotoxic T lymphocyte
Ctrl	Control
CXCL12	CXC motif chemokine 12

D

DAB	3,3'-Diaminobenzidine
dl	Deciliter
DKK-1	Dickkopf-related protein 1
DMEM	Dulbecco's modified eagle medium
DMSO	Dimethyl sulfoxide
DNA	Deoxyribonucleic acid
DPBS	Dulbecco's phosphate buffered saline

E

ECM	Extracellular matrix
EDTA	Ethylenediaminetetraacetic acid
EGFR	Epidermal growth factor receptor
eIF4e	Eukaryotic translation initiation factor 4E
EMT	Epithelial-mesenchymal transition
Erk1/2	Extracellular signal-regulated kinases 1/2

F

FAP	Fibroblast activation protein
FC	Flow cytometry
FCS	Fetal calf serum
FFPE	Formalin-fixed paraffin-embedded
FGF-2	Fibroblast growth factor-2
FKBP12	FK506-binding protein 12
fl/fl	Floxed
FOLFIRINOX	Folinic acid, fluorouracil, irinotecan and oxaliplatin
Fos	Finkel-Biskis-Jinkins sarcoma virus oncogene
FoxP3	Forkhead box P3
Fra-2	Fos-related antigen-2
FSC	Forward scatter

G

g	Gram
GEMMs	Genetically engineered mouse models
GSK-3β	Glycogen synthase kinase-3 beta

H

H&E	Hematoxylin and eosin
H_2O_2	Hydrogen peroxide
H_2Odd	Double-distilled water
HASCs	Human adipose tissue-derived stem cells
HCC	Hepatocellular carcinoma
HGF	Hepatocyte growth factor
HRP	Horseradish peroxidase
HSCs	Hepatic stellate cells

I

ICIs	Immune checkpoint inhibitors
iDTR	Inducible diphtheria toxin receptor
IFN-γ	Interferon-γ
IgG	Immunoglobulin G
IHC	Immunohistochemistry
IL	Interleukin
iNOS	Inducible nitric oxide synthase
IRFs	Interferon regulatory factors

J

JAK/STAT	Janus kinase/signal transducer and activator of transcription
JNK	c-Jun amino-terminal kinase
Jun	Ju-nana

K

K.O.	Knockout
kb	Kilobase
kg	Kilogram
$KHCO_3$	Potassium bicarbonate
KRAS	Kirsten Rat sarcoma viral oncogene homolog

L

l	Liter

LGR5/6	Leucine-rich repeat-containing G-protein coupled receptor 5 / 6
LKB1	Liver kinase B1
loxP	Locus of crossover P
LPS	Lipopolysaccharide
LUA	Landesuntersuchungsamt
LUAD	Lung adenocarcinoma
LZD	Leucine zipper domain

M

M	Molar
MAPKs	Mitogen-activated protein kinases
MASH	Metabolism associated steatohepatitis
M-CSF	Macrophage-colony stimulating factor
MDSCs	Myeloid-derived suppressor cells
MET	Mesenchymal-epithelial transition factor
MF	Myofibroblast
mg	Milligram
ml	Milliliter
mm	Millimeter
MMPs	Matrix metalloproteinases
MSCs	Mesenchymal stem cells
mTOR	Mammalian target of rapamycin
mTORC1	mTOR complex 1
MU-Gal	4-Methylumbelliferyl-β-D-galactopyranoside

N

NaCl	Sodium chloride
NF-κB	Nuclear factor-kappa B
NH_4Cl	Ammonium chloride
NSCLC	Non-small cell lung cancer

O

O_2	Oxygen

P

p38/MAPK	p38 mitogen-activated protein kinase
P53	Tumor protein 53
PanIN	Pancreatic intraepithelial neoplasia
PBS	Phosphate-buffered saline
PCR	Polymerase chain reaction
PDAC	Pancreatic ductal adenocarcinoma

PDGF	Platelet-derived growth factor
PD-L1	Programmed death-ligand 1
Pdx-1	Pancreatic and duodenal homeobox 1
pen/strep	Penicillin/streptomycin
PFA	Paraformaldehyde
pH	Potential of hydrogen
PI3K	Phosphatidylinositol-3-kinase
PIK3CA	Phosphatidylinositol 3-kinase catalytic subunit alpha
PPAR-γ	Peroxisome proliferator-activated receptor-γ
pRPS6	Phospho-ribosomal protein S
PRRs	Pattern recognition receptors
PSCs	Pancreatic stellate cells
Ptf1	Pancreas specific transcription factor 1 alpha

R

RBC	Red blood cell
RET	Rearranged during transfection
RICTOR	Rapamycin-insensitive companion of mTOR
ROS	Reactive oxygen species
rpm	Revolutions per minute
RPMI	Roswell park memorial institute medium
RT	Room temperature

S

S6K1	S6 kinase 1
SCLC	Small cell lung cancer
SD	Standard deviation
SDF-1	Stromal-derived factor-1
sec	Second
Smad	Sma and Mad related
SPF	Specific pathogen-free
SR	Sirius Red
SREBP-1	Sterol regulatory element-binding protein-1
SSC	Sideward scatter

T

TACE	Transarterial chemoembolization
TAD	Transactivation domain
TAE	Tris-acetate-EDTA
Tam	Tamoxifen
TAMs	Tumor-associated macrophages
TARC	Translational animal research center

TFs	Transcription factors
TGF-β	Transforming growth factor-β
TGFβR	Transforming growth factor beta receptor type
TILs	Tumor-infiltrating lymphocytes
TLRs	Toll-like receptors
TME	Tumor microenvironment
TPA	12-O-tetradecanoylphorbol-13-acetate
TRE	TPA-responsive element
Tregs	Regulatory T cells
Tris	Tris(hydroxymethyl)aminomethane

U

U	Unit
UV	Ultraviolet

V

VEGF	Vascular endothelial growth factor

W

WHO	World Health Organization
Wnt	Wingless-type MMTV integration site family

List of Figures

List of Tables

List of Formulas

Abstract

Cancer remains one of the leading causes of mortality worldwide, with an estimated 10 million deaths in 2022 according to the World Health Organization. Despite significant advances in cancer research and treatment, certain types of cancer, particularly those characterized by a dense stromal reaction, continue to pose significant challenges in terms of treatment efficacy and patient outcomes. This thesis focuses on three such desmoplastic cancers: lung cancer, hepatocellular carcinoma (HCC), and pancreatic ductal adenocarcinoma (PDAC). While PDAC and certain forms of lung cancer are highly desmoplastic, HCC shows significantly less desmoplastic activity with little intratumoral extracellular matrix (ECM), though its characteristic capsule formation should be noted. These cancers are known for their aggressive nature, poor prognosis, and resistance to conventional therapies, largely due to their complex tumor microenvironment (TME).

The urgent need for new therapeutic strategies for these cancer types stems from their unique biological characteristics. Lung cancer, particularly non-small cell lung cancer (NSCLC), the leading cause of cancer-related deaths globally, often develops resistance to targeted therapies. HCC, typically arising in the context of chronic liver disease, presents challenges due to its heterogeneity and the compromised liver function of patients. PDAC is notorious for its late diagnosis and extreme resistance to current treatment modalities, largely attributed to its dense stromal component.

This study investigates the complex roles of cancer-associated fibroblasts (CAFs) and tumor-associated macrophages (TAMs) in the progression of these desmoplastic cancers. Various subcutaneous and orthotopic injection models were established to study tumor-stroma interactions *in vivo*. A key aspect involved using a bi-transgenic Col3a1-CreERT2/TGFβRII fl/fl mouse model to selectively inactivate TGF-β signaling in CAFs, revealing its impact on tumor growth and the TME. The study also explored innovative therapeutic strategies, Fra-2 antisense oligonucleotide and the mTOR inhibitor rapamycin, to target different components of the tumor microenvironment. Combination therapy showed promising results in reducing tumor burden and modulating the TME in an orthotopic HCC model. The post-treatment mRNA expression profiles unveiled striking alterations, with notable changes in collagen transcripts. Histological examination provided additional data on collagen distribution within the tumor tissue, confirming this observation. Combination therapies elicited more pronounced effects on several measured parameters compared to single-agent treatments, highlighting synergistic effects. Additionally, novel murine models for HCC and PDAC research were established, and a new Col3a1-CreERT2/iDTR mouse strain was developed for future CAF depletion studies. The findings highlight the intricate interplay between tumor cells and stromal

components, offering insights into potential therapeutic approaches for desmoplastic cancers and paving the way for more effective treatment strategies in these challenging malignancies.

Zusammenfassung

Krebs bleibt weltweit eine der häufigsten Todesursachen, mit schätzungsweise 10 Millionen Todesfällen im Jahr 2022 laut der Weltgesundheitsorganisation. Trotz bedeutender Fortschritte in der Krebsforschung und -behandlung stellen bestimmte Krebsarten, insbesondere jene mit dichtem Stroma, weiterhin erhebliche Herausforderungen hinsichtlich der Behandlungseffizienz und der Überlebensrate dar. Die vorliegende Arbeit konzentriert sich auf drei Krebsarten: Lungenkrebs, hepatozelluläres Karzinom (HCC) und duktales Adenokarzinom des Pankreas (PDAC). Während PDAC und bestimmte Lungenkrebsformen stark desmoplastisch sind, zeigt HCC eine deutlich geringere desmoplastische Aktivität mit wenig intratumoraler extrazellulärer Matrix (ECM), wobei jedoch die charakteristische Kapselbildung zu beachten ist. Diese Krebsarten sind bekannt für ihre Aggressivität, schlechte Prognose und Resistenz gegenüber konventionellen Therapien, größtenteils aufgrund ihrer komplexen Tumormikroumgebung (TME).

Der dringende Bedarf an neuen therapeutischen Strategien für diese Krebsarten ergibt sich aus ihren einzigartigen biologischen Eigenschaften. Lungenkrebs, insbesondere das nicht kleinzellige Lungenkarzinom (NSCLC), die weltweit führende Ursache für krebsbedingte Todesfälle, entwickelt oft Resistenzen gegen zielgerichtete Therapien. Das HCC, das typischerweise im Kontext chronischer Lebererkrankungen auftritt, stellt aufgrund seiner Heterogenität und der beeinträchtigten Leberfunktion der Patienten eine besondere Herausforderung dar. PDAC ist berüchtigt für seine späte Diagnose und extreme Resistenz gegen aktuelle Behandlungsmethoden, was größtenteils auf seine dichte stromale Komponente zurückzuführen ist.

Diese Studie untersucht die komplexen Rollen von Krebs-assoziierten Fibroblasten (CAFs) und Tumor-assoziierten Makrophagen (TAMs) bei der Progression dieser desmoplastischen Krebsarten. Verschiedene subkutane und orthotope Injektionsmodelle wurden etabliert, um Tumor-Stroma-Interaktionen *in vivo* zu untersuchen. Ein zentraler Aspekt beinhaltete die Verwendung eines bi-transgenen Col3a1-CreERT2/TGFβRII fl/fl Mausmodells zur selektiven Inaktivierung des TGF-β-Signalwegs in CAFs, was dessen Auswirkungen auf das Tumorwachstum und die TME offenbarte. Die Studie erforschte auch innovative therapeutische Strategien, Fra-2-Antisense-Oligonukleotid und den mTOR-Inhibitor Rapamycin, um verschiedene Komponenten der Tumormikroumgebung zu beeinflussen. Die Kombinationstherapie zeigte vielversprechende Ergebnisse bei der Reduzierung der

Tumorlast und der Modulation der TME in einem orthotopen HCC-Modell. Die mRNA-Expressionsprofile nach der Behandlung enthüllten auffällige Veränderungen, mit bemerkenswerten Änderungen in Kollagen-Transkripten. Die histologische Untersuchung lieferte zusätzliche Daten zur Kollagenverteilung im Tumorgewebe und bestätigte diese Beobachtung. Die Kombinationstherapie zeigten im Vergleich zu Einzelwirkstoffbehandlungen ausgeprägtere Effekte auf mehrere gemessenen Parameter, was ihr synergistisches Wirken bestätigt. Zusätzlich wurden neue Mausmodelle für die HCC- und PDAC-Forschung etabliert und ein neuer Col3a1-CreERT2/iDTR Mausstamm für zukünftige CAF-Depletionsstudien generiert. Die Ergebnisse unterstreichen das komplexe Zusammenspiel zwischen Tumorzellen und Stroma-Komponenten und bieten Einblicke in potenzielle therapeutische Ansätze für desmoplastische Krebsarten, wobei sie den Weg für effektivere Behandlungsstrategien bei diesen herausfordernden Malignomen ebnen.

1 Introduction

1.1 Cancer as significant public health threat

Despite significant advancements in scientific research, cancer continues to pose a profound threat to global health. After cardiovascular diseases, cancer ranks as the second leading cause of mortality worldwide, claiming approximately 10 million lives in 2022, according to data from the World Health Organization (WHO; [1]; Fig. 1). Among all cancer types, lung cancer remains one of the deadliest, responsible for nearly two million deaths. Additionally, primary liver cancer (predominantly hepatocellular carcinoma, HCC) accounted for 760,000 fatalities, while pancreatic cancer, with ductal adenocarcinoma (PDAC) representing more than 90% of cases, claimed 470,000 lives in the same year. These three cancer types, despite their differences in origin and mortality rates, display varying levels of desmoplastic characteristics. PDAC and certain lung cancers exhibit pronounced desmoplastic reactions, characterized by dense fibroblastic extracellular matrix (ECM) infiltrating between the tumor cells. In contrast, HCC typically presents with significantly lower desmoplastic activity and minimal intratumoral ECM, although its characteristic capsule formation remains a notable feature. This characteristic not only complicates treatment but also contributes to their aggressiveness. Each of these cancer types exhibits distinct underlying risk profiles. Non-small cell lung cancer (NSCLC) demonstrates a strong association with tobacco exposure [2]. HCC development predominantly results from viral hepatitis B infection and alcohol-related liver disease [3], while pancreatic cancer involves multiple, less well-characterized factors including certain environmental chemicals and toxins [4].

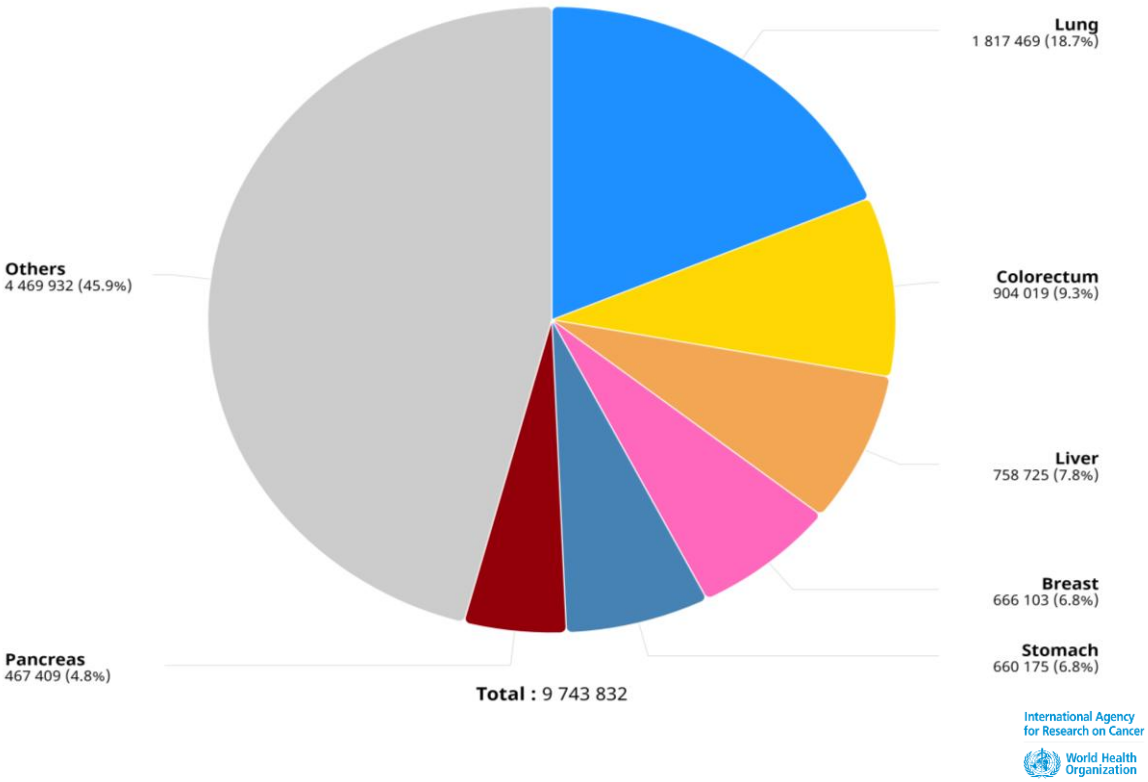

Figure 1: Global cancer statistics. Pie chart depicting cancer mortality rates across genders and all age groups worldwide in 2022 (adapted from [1]).

1.1.1 Lung cancer

As previously stated, lung cancer exerts a profound negative impact on global health, as evidenced by the enormous two million deaths worldwide reported in 2022 alone [1]. It is classified into two main types based on histology: small cell lung cancer (SCLC) and non-small cell lung cancer (NSCLC), with NSCLC being the most prevalent subtype, accounting to 85-90% of cases [5]. NSCLC comprises various histological subtypes, including lung adenocarcinoma (LUAD), lung squamous cell carcinoma, and large-cell lung carcinoma [6]. Notably, LUAD predominantly originates in the distal regions of the lung, while squamous cell carcinoma tends to occur in the central lung, demonstrating distinct growth pattern characteristics.

The mutational landscape of lung cancer is unique, characterized by numerous molecular alterations, encompassing both oncogenes and tumor suppressor genes. Genomic changes, such as somatic mutations, translocations, homozygous gene deletions, amplifications as well as epigenetic silencing, drive alterations in different pathways. These changes transition normal cells to premalignant states and ultimately lead to the formation of lung tumors [7]. Genetic profiling reveals significant heterogeneity among lung cancer patients. Several

oncogenes and tumor suppressor genes have been identified in NSCLC, including EGFR, KRAS, LKB1, ALK, MET, BRAF, PIK3CA, RET, ROS1, and P53 genes, which serve as actionable targets [7], [8], [9]. Recommended treatment for early-stage (stage I or II) NSCLC typically involves surgical tumor resection followed by adjuvant therapy, whereas advanced-stage (stage III or IV) disease often can only be treated in a palliative approach using chemotherapy or radiotherapy [10,11]. However, conventional chemotherapeutic agents face limitations such as non-specific targeting and low efficacy. In recent years, remarkable progress has been achieved, especially in the fields of personalized medicine and cancer therapy. Immunotherapy, including adoptive cell transfer (ACT) and immune checkpoint inhibitors (ICIs), utilizes components of the immune system to target tumor cells [12], [13]. However, only a small subset of patients experiences long-term benefits. Treatments of such desmoplastic cancers often show decreased efficiency compared to those targeting stroma-poor tumors. Through intricate crosstalk with tumor cells, cancer-associated fibroblasts (CAFs) significantly drive tumor proliferation, invasion, and metastasis, as will be explained in more detail below [14]. In NSCLC, the presence of a fibrotic, CAF-rich stroma is common and correlates negatively with patient prognosis [15], [16]. However, CAF-targeted interventions are considered as promising novel strategies in cancer treatment [17], [18].

1.1.2 Liver cancer

Hepatocellular carcinoma (HCC) ranks among the most prevalent malignant tumors worldwide, representing the second leading cause of mortality [3]. Chronic inflammation, triggered by various factors like chronic viral hepatitis B and C infections, obesity, alcoholism leading to alcohol-associated liver disease (ALD), and iron accumulation and resultant oxidative stress in hemochromatosis, serve as key promoters of malignant hepatocyte transformation. In metabolism associated steatohepatitis (MASH), which usually goes along with metabolic syndrome, mainly with overweight, insulin resistance or overt type 2 diabetes, the process starts with steatohepatitis (fatty liver inflammation), which can progress to fibrosis and cirrhosis if left untreated [19], [20], [21]. Cirrhosis is characterized by extensive scarring of the liver tissue, compromising liver architecture and vascular organization and finally impairing liver function and causing portal hypertension. As in the other chronic liver diseases, cirrhosis is a major predisposition for the development of HCC, and most HCCs develop within the cirrhotic liver (Fig. 2). This leads to fatal outcomes, contributing to approximately two million deaths worldwide, representing 4% of total global mortality due to cancer [22].

The complex etiology of HCC, involving multiple risk factors and a prolonged disease course, presents significant challenges for early detection and effective treatment [23]. Current

therapeutic approaches for HCC encompass a range of options, depending on the stage of the disease and the patient's overall liver function. For early-stage HCC, curative treatments such as surgical resection, liver transplantation, and radiofrequency ablation are the primary options [24]. However, the majority of HCC cases are diagnosed at advanced stages, limiting the applicability of these curative treatments [25].

For intermediate-stage HCC, transarterial chemoembolization (TACE) is the standard of care, while advanced-stage disease is typically treated with systemic therapies. The approval of the poly-tyrosine kinase sorafenib in 2007 marked a significant milestone in the systemic treatment of HCC, offering the first effective targeted therapy for advanced disease [26], [27], although it prolongs survival only by a few months and often incurs significant side effects. Since then, several other multikinase inhibitors have been approved, including growth factor targeted therapies with lenvatinib as a first-line treatment, and regorafenib, cabozantinib, and ramucirumab as second-line options [28], [29], [30], [31]. Recent advancements have greatly enhanced the treatment options available for patients with late-stage HCC. The combination of atezolizumab (anti-PD-L1) and bevacizumab (anti-VEGF) has emerged as the standard first-line systemic therapy, demonstrating superior overall survival compared to sorafenib [32]. Lenvatinib remains an alternative first-line option [33]. In the second-line setting, multiple options are available, including regorafenib, cabozantinib, ramucirumab, pembrolizumab, and dual combinations providing tailored approaches based on individual patient characteristics [34], [35], [36].

Despite these advances, the prognosis for many HCC patients remains poor, with a 5-year survival rate of only 18% [37]. This underscores the urgent need for continued research into novel therapeutic strategies, improved methods for early detection, and a better understanding of the molecular mechanisms driving HCC progression [38].

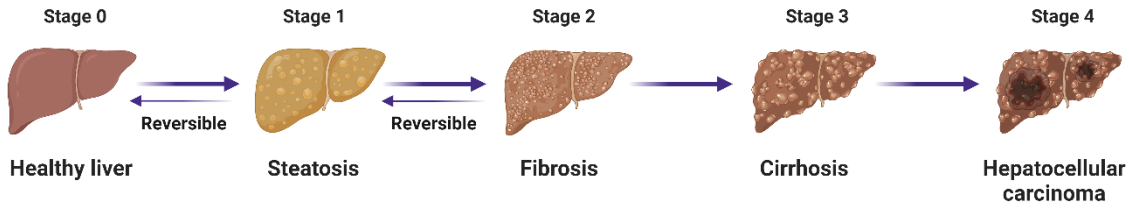

Figure 2: Stages of liver disease progression from healthy liver to hepatocellular carcinoma. Progression from a healthy liver (Stage 0) to hepatocellular carcinoma (Stage 4) through steatosis, fibrosis and cirrhosis, with indications of reversibility in early stages and irreversibility in advanced stages (created with BioRender.com).

1.1.3 Pancreatic cancer

Pancreatic cancer is a highly lethal very aggressive malignancy originating in the pancreas, an organ crucial for digestive and endocrine functions. Ranked as the seventh leading cause of cancer-related deaths worldwide, it has an alarming five-year survival rate of under 10% [39]. The most common and deadly form is pancreatic ductal adenocarcinoma (PDAC), accounting for over 90% of all cases. A leading hypothesis regarding the cellular origin of PDAC suggests that acinar cells, known for their remarkable plasticity within the pancreas, undergo a process known as acinar-to-ductal metaplasia (ADM). This transformation, during which acinar cells acquire a ductal-like epithelial phenotype, is considered an early event in the development of PDAC. This cellular reprogramming is usually triggered by various stressors such as inflammation or tissue injury [40], [41].

The most prevalent mutation occurs in the KRAS oncogene, present in over 90% of cases, which drives aberrant signaling pathways that promote cell proliferation, survival and invasion [42]. This mutation plays a critical role in the transformation of metaplastic cells into pancreatic intraepithelial neoplasia (PanIN). Additionally, inactivating mutations in tumor suppressor genes such as TP53, CDKN2A, as well as disruptions in the TGF-β signaling pathway are contributing to the loss of cell cycle control, genomic instability and evasion of apoptosis [43], [44]. This sequential acquisition of mutations ultimately results in the development of invasive PDAC [45] (Fig. 3).

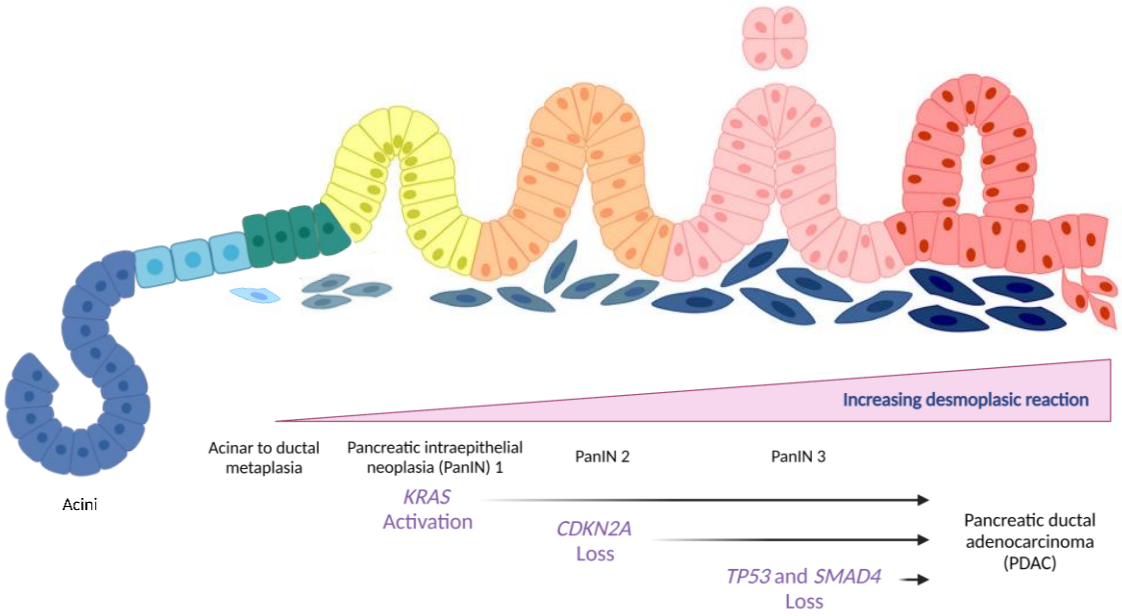

Figure 3: Development of pancreatic ductal adenocarcinoma. Morphological changes and key genetic alterations associated with each stage of pancreatic intraepithelial neoplasia (PanIN). The progression is marked by increasing desmoplasia and mutations in KRAS, CDKN2A, TP53 and SMAD4 genes (adapted from [45], with modifications).

PDAC is characterized by a dense desmoplastic stroma, which contributes to therapeutic resistance by impairing drug delivery and promoting an immunosuppressive microenvironment. Early detection of PDAC remains challenging due to its anatomical location and unspecific symptoms, including jaundice, unintentional weight loss and abdominal pain [46]. As a result, the majority of patients are diagnosed at an advanced stage, where the tumor has either metastasized or is locally advanced. Therefore, surgical resection - the only potentially curative procedure - is no longer feasible for most of the patients [47]. Even if surgical resection is possible, the recurrence rate remains high.

Usually, palliative systemic chemotherapy remains the primary treatment for advanced PDAC. The two standard first-line options are gemcitabine combined with nanoparticle albumin-bound (nab)-paclitaxel and the FOLFIRINOX treatment scheme with multiple drugs. While these therapies provide some benefits, they have only modestly improved patient survival rates [48],[49]. Due to high radioresistance radiotherapy is less commonly used to treat PDAC [50]. However, it can be used as a neoadjuvant approach to render the tumors operable [51].

While immunotherapy, particularly immune checkpoint inhibitors, has transformed the treatment landscape for various cancers like melanoma and NSCLC, its impact on PDAC has shown to be limited [52], [53]. Only a small subset of PDAC patients, specifically those exhibiting microsatellite instability, showed relevant responses [54], [55].

Thus, the need for novel therapeutic strategies in PDAC management. For the stroma-rich PDAC, stroma-targeted interventions have potential. These approaches belong to therapies that address the tumor microenvironment (TME) that is composed of immune cells and cancer-associated fibroblasts (CAFs), potentially enhancing drug delivery and overcoming pancreatic cancer's intrinsic resistance mechanisms such as the immune suppressive TME.

Hence, there is a pressing need for innovative therapeutic strategies in managing PDAC, such as stroma-targeted interventions. These approaches seek to reconfigure the TME, potentially improving drug delivery and overcoming the inherent resistance mechanisms of pancreatic cancer.

1.2 Components of the TME

The tumor microenvironment (TME) is a dynamic milieu comprising an intricate network of cellular and non-cellular components that influence tumor initiation, progression, metastasis and therapeutic response [56,57]. Desmoplastic tumors exhibit distinctive features within their TME, marked by a prominent stromal reaction and extensive remodeling of the extracellular matrix (ECM). One of the most important cell types for shaping the ECM are fibroblasts, mesenchymal cells that are essential for the synthesis and modification of the ECM and the

typical histopathologic features to desmoplastic tumors. While maintaining a quiescent state in non-pathological tissues, they play a pivotal role in processes such as wound healing, tissue fibrosis and tumor fibrosis [58–60]. Following injury, fibroblasts can transition into myofibroblasts (MF) through the activation of the transforming growth factor-β (TGF-β) signaling pathway, thereby contributing to the synthesis of diverse ECM molecules during tissue repair and inflammation [61]. In the context of tumor biology, activated fibroblasts, referred as CAFs, play a crucial role in mediating communication between tumor cells and the surrounding stroma, facilitating ECM deposition, remodeling and also stiffening [62,63], as also illustrated in Fig. 4. ECM remodeling, characterized by excessive deposition of collagen, fibronectin, and other matrix proteins, creates physical barriers that hinder drug uptake and immune cell infiltration, further driving disease progression and therapeutic resistance. By secreting a variety of cytokines, chemokines and growth factors, CAFs influence tumor cell behavior, promoting proliferation, invasion and metastasis [58, 60, 62]. Moreover, CAF-mediated promotion of neo-angiogenesis, the formation of new blood vessels, facilitates tumor growth and nutrient supply, which is critical for the expansion of cancer [65], [66]. However, the contribution of CAFs to tumorigenesis is not exclusively pro-tumorigenic, but can also display anti-tumorigenic effects, depending on the context [67], [68–70]. In addition to CAFs, the immune landscape within the TME of desmoplastic cancers is complex and diverse. Tumor-infiltrating lymphocytes (TILs), myeloid-derived suppressor cells (MDSCs) and tumor-associated macrophages (TAMs) constitute key immune cell populations within the TME, exhibiting diverse phenotypic and functional characteristics [71] . Effector T cells are involved in initiating anti-tumor immune responses, while regulatory T cells (Tregs) and immunosuppressive cytokines such as TGF-β and interleukin-10 (IL-10) create an immunosuppressive environment supporting tumor immune evasion and resistance to different therapeutic approaches [72], [73]. TAMs represent one of the most abundant immune cell populations within the TME communicating with various cell types [74], [75]. The presence of TAMs within the TME has been consistently linked to unfavorable clinical outcomes across different cancer types [76], [77],[78]. TAMs are actively involved in the secretion of numerous cytokines, growth factors and enzymes. These molecules include but are not limited to vascular endothelial growth factor (VEGF), fibroblast growth factor-2 (FGF-2), and matrix metalloproteinases (MMPs), which also facilitate angiogenesis, extracellular matrix remodeling and metastasis [79], [80], [81].

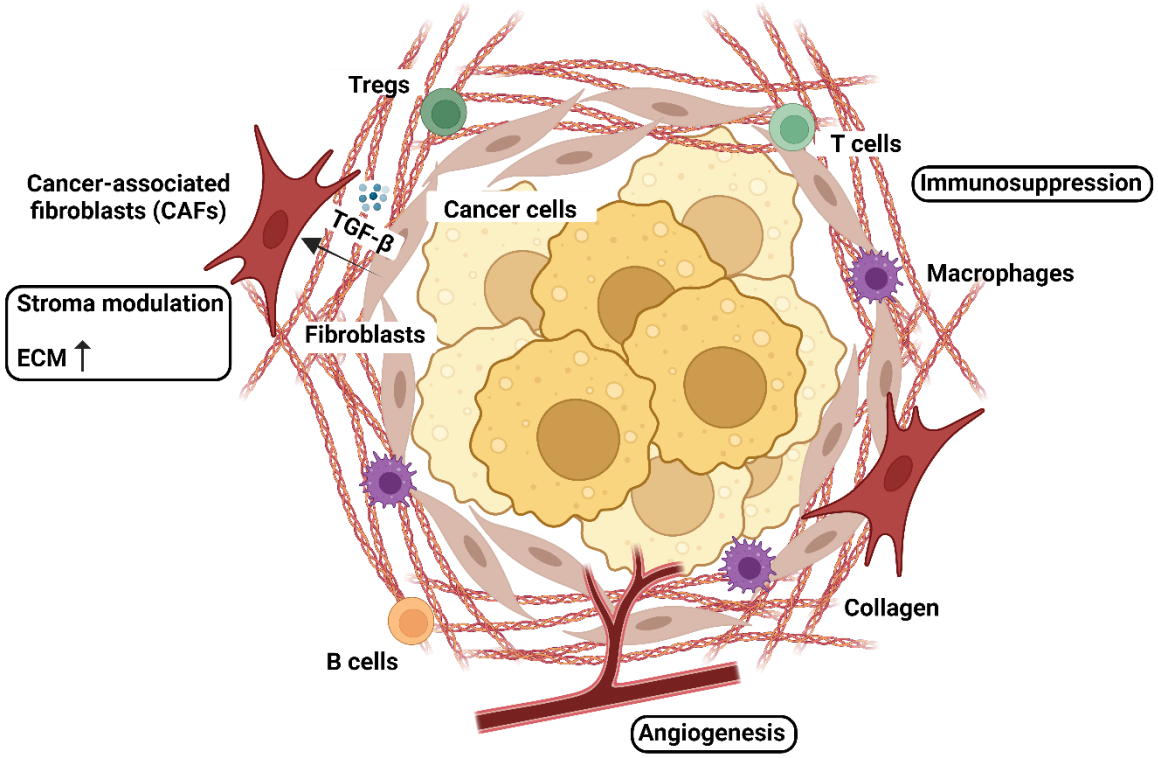

Figure 4: Schematic representation of the tumor microenvironment. Illustrated is a complex interplay of tumor cells, various immune cells, activated fibroblasts, and excessive extracellular matrix (ECM). Excessive desmoplasia is the main feature that promotes neo-angiogenesis, immunosuppression, and therapy resistance (created with BioRender.com).

1.2.1 Origins and activators of CAFs

The heterogeneous populations of CAFs within the TME are characterized by their diverse origins, activation pathways and expression of specific markers [82], [83], [84]. Tissue-resident fibroblasts, typically viewed as a major contributor to CAF populations, remain dormant until triggered by various stimuli, such as TGF-β, PDGF, FGF-2, stromal-derived factor-1 (SDF-1) and reactive oxygen species (ROS) [85], [86],[87]. Notably, CAFs themselves are important producers of hepatocyte growth factor (HGF) [85], [86], [87]. Furthermore, pulmonary mesenchymal stem cells (MSCs), hepatic stellate cells (HSCs), and pancreatic stellate cells (PSCs) are potential precursors for CAFs, depending on the cancer type [88], [89].

The activation process of bone marrow-derived mesenchymal stem cells (BM-MSCs) into CAFs entails complex interactions, involving modulation by bone marrow-derived progenitors and intercellular communication. Additionally, the exposure of BM-MSCs to a diverse array of cytokines in the tumor microenvironment acts as a potent stimulus, driving their evolution into CAFs [90], [91].

In certain contexts, particularly in breast cancer, white adipocytes have emerged as potential contributors to the CAF population, facilitated by the adipose-rich environment of breast tissue. Studies have demonstrated that both human adipose-derived stem cells (HASCs) under TGF- β stimulation and mature adipocytes exposed to tumor-secreted Wnt-3a can transdifferentiate into fibroblast-like cells [92], [93]. While still under investigation, other cell types such as epithelial cells and endothelial cells have been proposed as origins of CAFs. It should be noted that while EMT-like alterations in gene expression and behavior have been demonstrated in several cell types, the evidence for complete cellular transformation to fibroblasts or CAFs in human cancers is limited and would likely make only a minor contribution to CAF populations if present [94], [95], [96]. In addition, pericytes and smooth muscle cells have been observed to give rise to CAFs [97], [98]. The possibility of recruiting of various cell types and their plasticity within the TME to eventually become CAFs demonstrates the important function of CAFs for the tumor evolution.

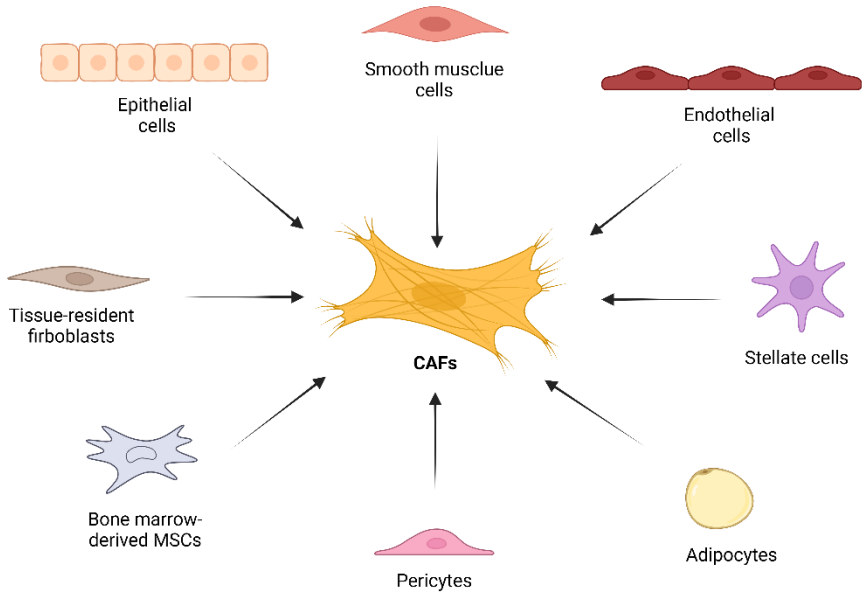

Figure 5: Origins of cancer-associated fibroblasts (CAFs) in the TME. CAFs arise from diverse cellular precursors including tissue-resident fibroblasts, bone marrow-derived mesenchymal stem cells, pericytes, endothelial cells, epithelial cells, smooth muscle cells, adipocytes, and stellate cells through various trans-differentiation processes (created with BioRender.com; inspired by [99]).

1.2.2 TGF-β signaling pathway in CAFs

TGF-β is a multifunctional cytokine that plays critical roles in diverse cellular processes, including cell growth, differentiation, apoptosis, and ECM production, making it a key regulator in both normal physiological functions and various pathological conditions, particularly in

cancer development and progression [100], [101]. In cancer biology, the TGF-β signaling pathway is particularly significant due to its role in activating CAFs. Therefore, a deeper understanding of TGF-β signaling in CAFs could uncover potential therapeutic targets. These targets could be used to disrupt tumor-stroma interactions, hindering cancer progression.

The mature TGF-β protein is initially secreted in a latent complex bound to latency-associated polypeptide, which binds TGF-β to the ECM and inhibits it from binding to its receptors [100]. Once activated by various factors including proteases, integrins, reactive oxygen species, or mechanical forces, TGF-β interacts with the transmembrane kinases transforming growth factor beta receptor type I (TGFβRI) and TGFβRII leading to the phosphorylation of downstream signaling molecules. This triggers a cascade of intracellular events, including canonical Smad)-dependent signaling and activation of non-Smad pathways [102]. The canonical TGF-β/Smad signaling involves a heterotetrameric receptor complex of two type I and two type II transmembrane receptor subunits with serine/threonine kinase domains. Ligand binding triggers type II receptor mediated phosphorylation of the type I receptor, activating Smad2 and Smad3 in most cells [103]. These activated Smad proteins associate with Smad4 and migrate to the nucleus. Upon nuclear translocation, these complexes interact with transcription factors (TFs) and co-regulators, thereby regulating the expression of target genes involved in various cellular processes. Cell type-specific responses to TGF-β vary due to differential expression of these regulators [104], [105], [106], [107]. The array of cellular pathways activated by TGF-β through diverse cellular interactions are collectively referred to as non-canonical signaling pathways. Key examples are illustrated schematically in Figure 4, including Erk1/2, p38/MAPK, c-Jun amino-terminal kinase (JNK), JAK/STAT, and PI3K/Akt pathway [108], [109], [106] (Fig. 6).

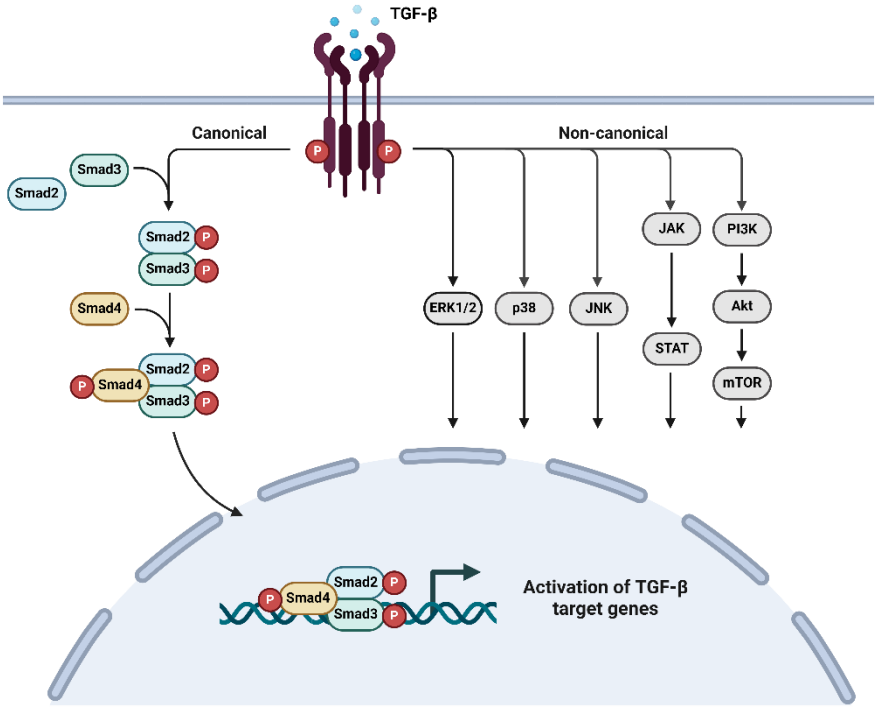

Figure 6: Schematic overview of TGF-β -induced canonical and non-canonical signaling. TGF-β signaling involves a heterotetrameric receptor complex of type I and type II transmembrane receptor subunits. Ligand binding leads to type II receptor mediated phosphorylation of the type I receptor, activating Smad2 and Smad3. These activated Smad proteins form complexes with Smad4 and translocate to the nucleus, recruiting transcriptional regulators to modulate target gene expression. TGF- β also activates or modulates non-canonical pathways including Erk1/2, p38/MAPK, JNK, JAK/STAT, and PI3K/Akt (created with BioRender.com).

1.2.3 Tumor associated macrophages (TAMs)

Apart from tissue resident macrophages like Kupffer cells in the liver, bone marrow-derived monocytes are the precursors of originally no-tissue resident macrophages, both being key players of the innate immune system that are widely distributed throughout all organs [110]. They play a vital role in maintaining tissue health by clearing away dead cells and cellular remnants [111], [112]. Macrophages act as a primary defense against pathogens but can also act as players of the adaptive immune system while presenting processed antigens. Equipped with a range of pattern recognition receptors (PRRs), such as Toll-like receptors (TLRs), they can detect and respond to pathogen-related as well as to internal (danger associated molecular patterns, DAMPs) signals [113], [114]. When these receptors recognize specific microbial or inflammation related patterns, they activate key signaling pathways involving nuclear factor-kappa B (NF-κB), mitogen-activated protein kinases (MAPKs) and interferon regulatory factors (IRFs). This activation cascade leads to the production of cytokines and chemokines that drive and regulate the inflammatory response [115], [116].

Macrophages display high plasticity in response to various stimuli and are typically categorized into two extreme immunological states. The pro-inflammatory type, often termed as M1 macrophages, is involved in driving inflammation, supporting immune responses and breaking down connective tissue. In contrast, the anti-inflammatory M2 macrophages are associated with dampening inflammation, fostering immune tolerance and supporting tissue repair by promoting the deposition of connective tissue, which can also contribute to cancer development. *In vitro*, the M1 macrophage phenotype is activated by exposure to lipopolysaccharide (LPS) and interferon-γ (IFN-γ), while the M2 macrophage phenotype is stimulated by IL-4 and IL-13 [117], [118], [119] (Fig. 7). However, the traditional classification of macrophage subsets into M1 and M2 categories significantly oversimplifies their complexity. Macrophages, in fact, display overlapping phenotypes that are influenced by their organ tissue location, the local microenvironment and the specific signaling cues they receive. For example, the M2 category can be further divided into several subtypes—M2a, M2b, M2c and M2d—each distinguished by unique receptor expressions, cytokine secretion profiles and immune effector functions [120], [121]. A variety of organ-specific, tissue resident macrophages have been described, e.g. for liver the prominent Kupffer cells, for lungs the alveolar macrophages, and for pancreas the pancreatic islet macrophages, interacinar macrophages, and perivascular macrophages. Given their significant roles in fibrosis and cancer development, strategies to convert TAMs, which often exhibit an M2-like phenotype, to a regenerative state are of considerable interest for potential therapeutic approaches.

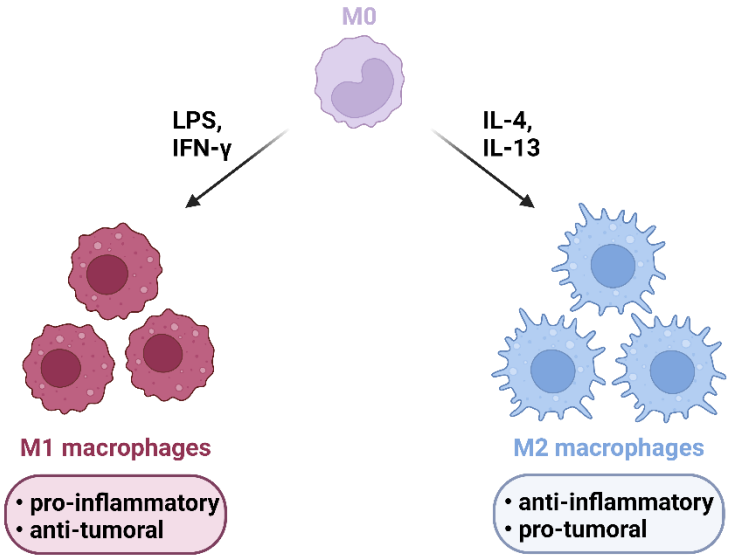

Figure 7: Inducers of (extreme) macrophage polarization *in vitro*. Monocytes (M0) can be polarized into M1 or M2 types depending on factors like IFN-γ, LPS (for M1) and IL-4, IL-13 (for M2). M1 macrophages enhance inflammation and anti-tumoral responses, while M2 macrophages can suppress inflammation and act pro-tumoral (created with BioRender.com; adapted from [122]).

1.2.4 Therapeutic modulation of M1 macrophages

1.2.4.1 Fra-2: key roles and functions in cellular regulation

As described in the previous chapter, the possibility of a modulation of TAMs is a highly promising goal for experimental approaches to treat cancer and the various functions and plasticity of macrophages offer many potential options for this. The activator protein-1 (AP-1) transcription factor family, a key regulator of diverse cellular processes, has been subject of extensive research since its discovery. This family comprises Jun (c-jun, junB, junD) and Fos (c-fos, Fra-1, Fra-2, fosB) proteins, each playing unique roles in transcriptional regulation [123]. Initially identified through its activation by the phorbol ester TPA (12-O-tetradecanoylphorbol-13-acetate), AP-1 binds to the TPA-responsive element (TRE), characterized by the consensus sequence TGAG/CTCA [33]. Structurally, AP-1 belongs to the basic-region leucine zipper (bZIP) class of transcription factors. This classification is based on its ability to form dimers through a leucine zipper domain (LZD) and bind to DNA via an adjacent basic amino acid-rich domain [124]. The dimerization capabilities of AP-1 proteins are diverse, with Jun proteins able to form both homo- and heterodimers, while Fos proteins, including Fos-related antigen-2 (Fra-2), are limited to heterodimer formation with Jun proteins [125]. Most AP-1 factors possess a transactivation domain (TAD) crucial for activating downstream target genes. However, Fra-2 and some other Fos family members lack a strong TAD, making them dependent on dimerization partners with TADs for effective transcriptional activation [126]. Fra-2's unique structure leads to varied transcriptional activity based on its dimerization partner. While c-Jun/Fra-2 dimers show lower activity than c-Jun/c-Fos pairs, Fra-2/JunD dimers exhibit enhanced activity compared to JunD homodimers, underscoring Fra-2's complex partner-dependent functionality. Fra-2 activation is governed by a complex interplay of multiple signaling pathways, responding to a range of stimuli such as growth factors and cytokines [127] (Fig. 8).

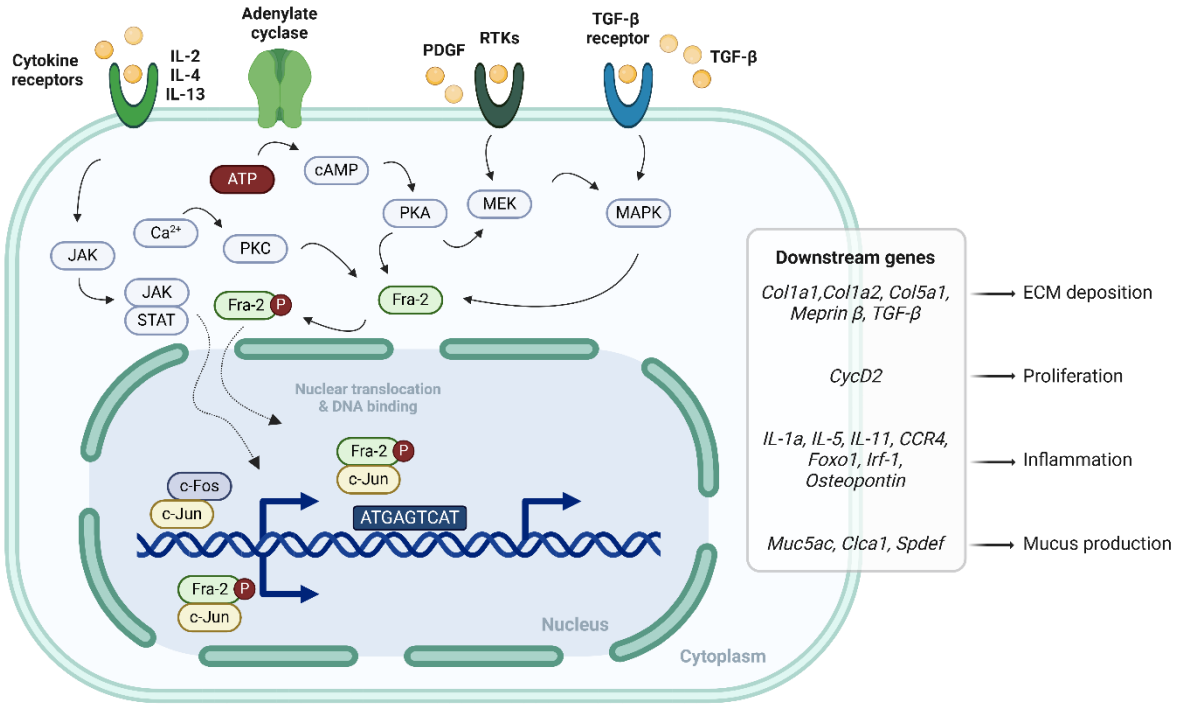

Figure 8: Regulation of Fra-2 and target gene expression. Fra-2 activity and expression are regulated by various upstream signals such as growth factors and inflammatory mediators, which activate MAP kinases and lead to Fra-2 phosphorylation. Newly formed Fra-2/c-Jun dimers have reduced transcriptional activity compared to c-Fos/c-Jun dimers, enabling Fra-2 to negatively regulate its own expression. Other Fra-2 dimers bind to AP-1 sites to activate genes involved in processes like proliferation, ECM deposition, inflammation and mucus production (created with BioRender.com; inspired by [127]).

Fra-2's influence extends across multiple cell types, each with unique outcomes that contribute to its roles in fibrosis and cancer. Fig. 9 illustrates the cellular mechanisms involved in lung fibrosis. In the lung, M1 macrophages are transformed into M2 macrophages through the action of macrophage-colony stimulating factor (M-CSF). This transformation is accompanied by an increase in Fra-2 expression in macrophages. The M2 macrophages then produce and release interleukins IL-4 and IL-13. These cytokines stimulate collagen production in fibroblasts. Besides, the image shows fibroblasts with increased Fra-2 levels. These activated fibroblasts produce high amounts of IL-1. The release of IL-1 promotes both pro-angiogenic (formation of new blood vessels) and pro-inflammatory responses in the surrounding tissue [128], [129].

Recent *in vitro* studies using primary cultures of bone marrow-derived macrophages have shown Fra-2's role in macrophage plasticity. These studies have revealed Fra-2's capacity to drive a phenotypic shift in macrophages, from the tumor-promoting M2 phenotype to the anti-tumoral M1 phenotype (Giardino MC *et al.*, unpublished).

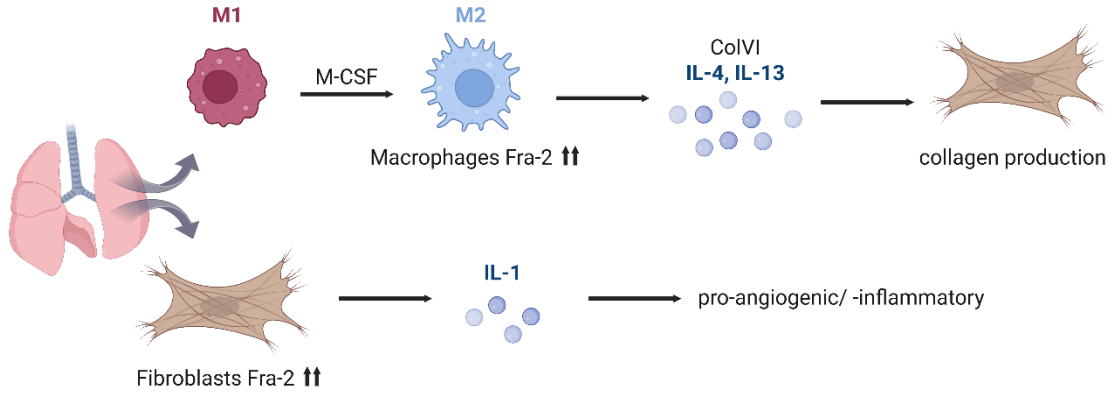

Figure 9: Fra-2 upregulation in macrophages and fibroblasts during lung fibrosis. Under the influence of M-CSF, M1 macrophages transition to the M2 phenotype, leading to increased Fra-2 expression. M2 macrophages release IL-4 and IL-13, which stimulate fibroblasts to produce collagen. Simultaneously, fibroblasts with upregulated Fra-2 expression produce higher levels of IL-1, which fosters pro-angiogenic and pro-inflammatory responses (created with BioRender.com; inspired by [127]).

1.2.4.1.1 Antisense oligonucleotides (ASOs) targeting Fra-2

Antisense oligonucleotides (ASOs) have emerged as powerful tools in molecular biology and therapeutics since their initial discovery in 1978 [130]. These short, synthetic single-stranded sequences, typically 12-24 nucleotides in length, are consisting of RNA and are designed to bind complementary RNA targets and regulate gene expression at the post-transcriptional level [131]. ASOs function through various mechanisms to modulate protein synthesis and gene expression (Fig. 10). The main mechanism of action involves binding to the target RNA (pre-mRNA, mRNA or microRNA) via Watson-Crick base pairing, forming a DNA-RNA hybrid. This structure, in turn, is recognized by the enzyme RNase H1, which cleaves the RNA strand of the duplex, leading to degradation of the target RNA and reduction of its levels in the cell [132].

Besides, ASOs bind closely to their target mRNA without inducing RNase H1-mediated degradation but leading to the inhibition of mRNA translation of the desired gene via ribosome blockade. This process "sequesters" the mRNA, reducing protein production without necessarily degrading the transcript [133], [134].

Another possible mode of action is the splice-switching of pre-mRNA [135]. By binding to specific splice sites or regulatory sequences, ASOs can modify pre-mRNA splicing, potentially leading to exon inclusion or exclusion [132], [136]. This process may result in the production of alternative protein isoforms or trigger nonsense-mediated mRNA decay [137], [138]. Due to their diverse mechanisms, ASOs can be adapted for a range of therapeutic applications, based on the desired effect and the specific attributes of the target RNA. Improvements in chemical

modifications have led to increased stability, enhanced target affinity and improved pharmacokinetic properties of ASOs, establishing them as a promising class of therapeutic agents [139], [140].

The research presented in this thesis investigates the therapeutic potential of an ASO designed to modulate the expression of Fra-2.

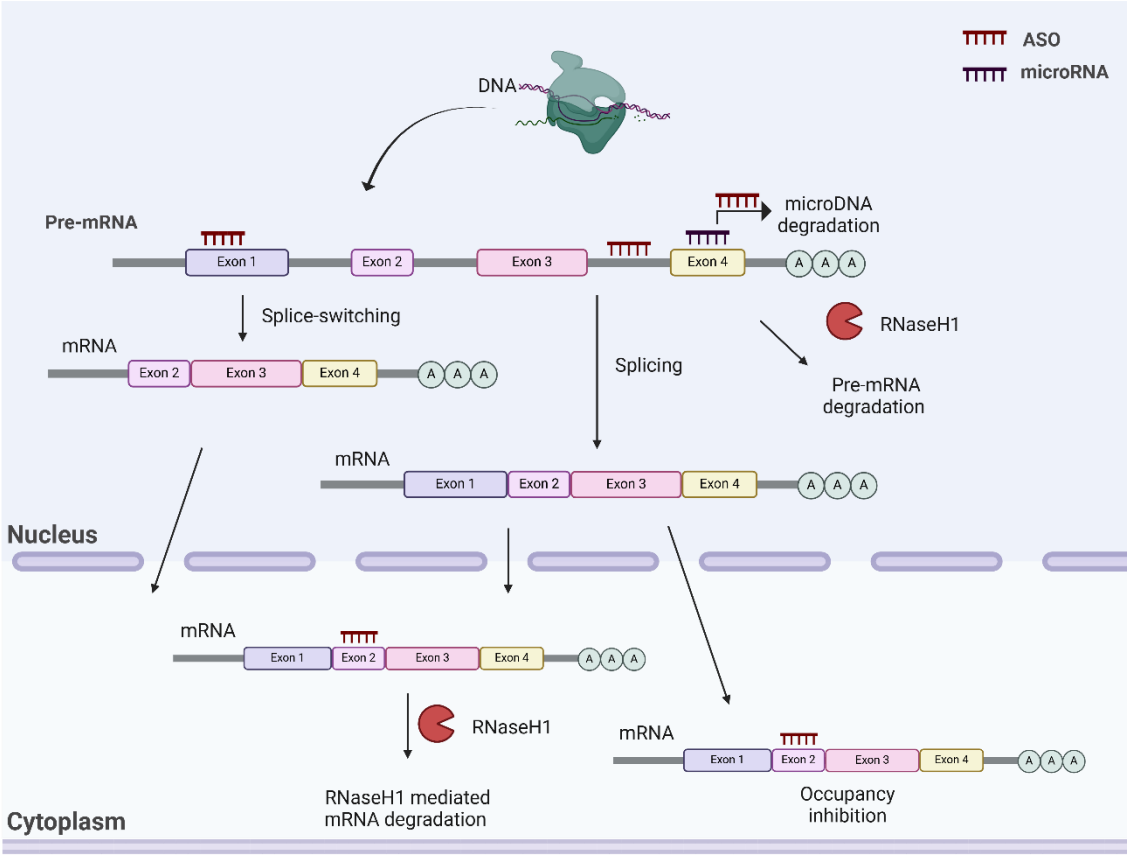

Figure 10: Mechanisms of antisense oligonucleotide (ASO) action. After cellular entry, ASOs modulate gene expression via: pre-mRNA splice-switching, RNase H1-mediated degradation of RNA targets and mRNA sequestration through complementary binding (created with BioRender.com; inspired by [141]).

1.2.4.2 Rapamycin: mTOR inhibitor

Rapamycin, also known as sirolimus, was initially discovered as an antifungal compound produced by the bacterium *Streptomyces hygroscopicus*. Further research uncovered rapamycin's potent immunosuppressive properties and over time it has emerged as a significant player in cancer therapeutics due to its ability to target the mammalian target of rapamycin (mTOR). mTOR is a critical intracellular regulator involved in energy metabolism and cell cycle control, making it an attractive target for anti-cancer therapies [142].

The mechanism of action of rapamycin involves the formation of a complex with FK506-binding protein 12 (FKBP12), which selectively inhibits mTOR complex 1 (mTORC1). This inhibition leads to decreased phosphorylation of mTORC1 substrates, affecting multiple downstream pathways, impacting lipid synthesis via sterol regulatory element-binding protein-1 (SREBP-1) and PPAR-γ, modulating transcription through S6K1 and S6, and affecting translation via 4E-BP1 and eIF4e. Besides, mTORC1 inhibition promotes autophagy, a cellular recycling process often dysregulated in cancer [143], [144] (Fig. 11). These multifaceted effects on cellular processes contribute to its potential in suppressing cell growth and proliferation, key hallmarks of cancer. Interestingly, while mTORC1 is readily inhibited by the rapamycin-FKBP12 complex, mTOR complex 2 (mTORC2) generally exhibits resistance. However, prolonged exposure to rapamycin may lead to reduced mTORC2 activity in certain cell types [145].

Originally approved as an immunosuppressant for organ transplant recipients nearly two decades ago, rapamycin's potential in cancer treatment has led to the development of derivatives with improved pharmacokinetic properties, collectively known as "rapalogs". These include everolimus (RAD001), temsirolimus (CCI-779), and deforolimus (AP23573) [146], [147].

Due to mTOR's involvement in cell proliferation, temsirolimus received approval in 2007 for the treatment of renal cell carcinoma and later for mantle cell lymphoma [148]. mTOR's relevance in cancer goes beyond its approved uses, with increased expression of pathway components like pRPS6, p-AKT, and RICTOR observed in cancers such as breast, colorectal and lung [149]. This upregulation often correlates with poor prognosis and early recurrence, again highlighting the pathway's significance in cancer progression. mTOR inhibitors are valued for their selectivity and minimal off-target effects and therefore predetermined for drug repurposing.

Recent investigations have expanded the therapeutic potential of rapamycin beyond its established role as an mTOR inhibitor. A promising hypothesis suggests that rapamycin may also have the ability to repolarize TAMs from a tumor-promoting M2 phenotype to a M1 phenotype. This repolarization could potentially reduce both tumor growth and progression. *In vitro* studies using primary cultures of bone marrow-derived macrophages (M0, M1 and M2 polarized) have provided strong evidence for this M2 to M1 macrophage repolarizing effect [150]. Given rapamycin's well-established safety profile and its known mechanism of action, these findings open new avenues for its application in cancer immunotherapy, potentially enhancing its efficacy in combination treatment strategies.

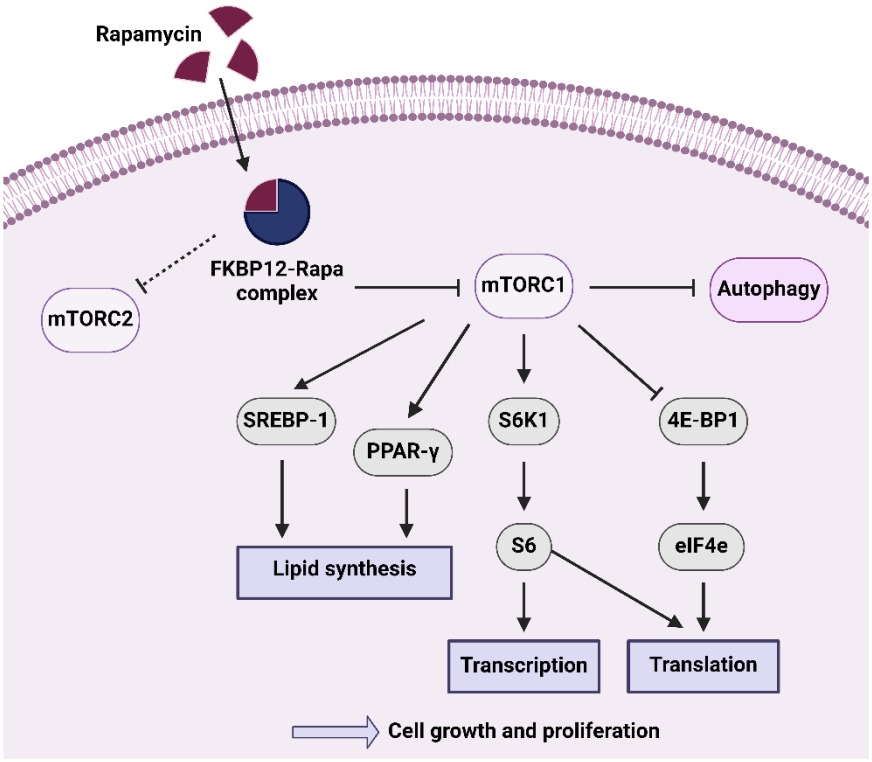

Figure 11: Mechanism of action of rapamycin. Rapamycin binds to FKBP12, forming a complex that directly inhibits mTORC1, while mTORC2 is sensitive to prolonged rapamycin treatment. mTORC1 inhibition influences several cellular pathways, including lipid synthesis (through SREBP-1 and PPAR- γ), transcription (via S6K1 and S6), and translation (via 4E-BP1 and eIF4e). Additionally, mTORC1 inhibition enhances autophagy (created with BioRender.com; inspired by [144]).

1.3 Mouse models

Mouse models have become essential tools in cancer research, offering valuable insights into the genetic underpinnings of tumor development and progression. The genetic similarities between mice and humans, particularly evident in the C57BL/6 strain where over 90% of genes have human equivalents, make these models highly relevant for studying human cancers [151], [152]. Subcutaneous and orthotopic injection models both offer distinct advantages and potential limitations. Subcutaneous models, where tumor cells are injected beneath the skin, are widely used due to their simplicity and ease of monitoring. They allow for straightforward tumor growth measurement using calipers, making it easy to assess treatment efficacy. These models are also less invasive and generally cause minimal distress to the animals. However, subcutaneous models have limitations in authentic replication of the TME, potentially leading to differences in tumor behavior compared to clinical scenarios [153].

By implanting tumor cells into their organ of origin, orthotopic models provide a more natural physiological setting. This approach better mimics the complex interactions between tumor cells and their native tissue, potentially offering more accurate insights into tumor growth,

metastasis and treatment response. However, these models are more challenging to establish and often require surgical procedures or genetical engineering. Besides, tracking tumor growth is more challenging compared to subcutaneous tumors, requiring *in vivo* imaging [153], [154]. Despite these challenges, the enhanced clinical relevance of orthotopic models makes them important in translational cancer research.

Genetically engineered mouse models (GEMMs) have been crucial for replicating and studying the wide range of genetic mutations identified across various human cancers. The Cre/*loxP* system has emerged as a powerful technique for creating conditional genetic models, allowing researchers to study gene function in specific tissues or cell types and mimicking common mutations and their role in cancer *in vivo* [155]. This system utilizes the Cre recombinase to delete DNA segments flanked by *loxP* sites, effectively inactivating or activating target genes. An advanced version of this system, CreERT2, offers even greater precision in genetic manipulation. By fusing Cre recombinase with a modified estrogen receptor, gene inactivation or activation can be controlled through the administration of tamoxifen (Tam) [156]. This advanced technique has become an essential tool for cancer studies.

1.4 Aim of the study

The complex interplay between tumor cells and the TME in desmoplastic cancers represents a significant challenge in cancer research and treatment. This study aimed to elucidate the intricate roles of key TME components, particularly CAFs and TAMs, in the progression of some of the most relevant types of desmoplastic cancers, including lung cancer, HCC and PDAC, while evaluating novel therapeutic approaches targeting the tumor stroma.

To achieve this goal, we established various subcutaneous and orthotopic injection models, enabling a comprehensive investigation of tumor development. These models were designed to provide valuable insights into the spatial and temporal dynamics of tumor-stroma interactions, which are crucial for understanding the complexities of cancer progression *in vivo*.

A central aspect of our study is to specifically inactivate TGF-β receptor II (TGFβRII) in CAFs by utilization of our bi-transgenic Cre/*loxP* mouse model (Col3a1-CreERT2/TGFβRII fl/fl). This targeted approach allowed us to assess the direct impact of CAF-specific TGF-β signaling on tumor progression. Furthermore, we generated a novel Cre/*loxP* mouse model designed for the complete depletion of CAFs (Col3a1-CreERT2/iDTR), which is intended to serve as a proof of principle of the tumor promoting role of CAFs in future experiments.

Our research explored the efficacy of various innovative therapeutic strategies targeting the tumor stroma. These included the application of a Fra-2 ASO to modulate CAF activity, the administration of the mTOR inhibitor rapamycin to target stromal components and to induce a phenotypic switch in TAMs from a pro-tumoral M2-like state to an anti-tumoral M1-like phenotype. Moreover, this study aimed to evaluate the potential synergistic effects of combining these therapeutic strategies.

2 Materials and methods

2.1 Materials and chemicals

Table 1: Equipment

Equipment	Supplier
Appl.Biosystems StepOne	Applied Biosystems
Autoclave	Sartorius AG
Balance	Kern PEJ
Balance	Precisa Gravimetrics AG
Cell counter	Bio-Rad Laboratories Inc.
Centrifuge	Thermo Fisher Scientific Inc.
ChemiDoc Imaging System	Bio-Rad Laboratories Inc.
CO_2 incubator	Heraeus
Electrophoresis Power Supply (Consort E844)	Merck KGaA
FACSSymphony™	BD Biosciences
Freezer (-20 °C)	Liebherr-International Deutschland GmbH
Freezer (-80 °C)	Thermo Fisher Scientific Inc.
Heatblock	Eppendorf AG
Ice machine	Ziegra Eismaschinen GmbH
Incubation shaker	Thermo Fisher Scientific Inc.
Isoflurane anesthesia machine (EZ-7000 Classic System)	E-Z Systems Inc.
Liquid nitrogen cell tank	Thermo Fisher Scientific Inc.
Magnetic stirrer	Merck KGaA
Microscope Leica DMi8	Leica Mikrosysteme Vertrieb GmbH
Microscope Zeiss AXIO	Carl Zeiss AG
Microwave	Alaska e.K.
Neubauer counting chamber	Braun
PCR cycler	Eppendorf AG
pH Meter	WTW
Pipettes	Eppendorf AG
Refrigerator (4 °C)	Liebherr-International Deutschland GmbH
Safety cabinet Microflow	Bioquell UK Ltd

Equipment	Supplier
Serological pipette controller	Hirschmann Laborgerate GmbH & Co. KG
scil Vet abc Plus+™	Scil Animal Care
Spectrophotometer NanoDrop	Thermo Fisher Scientific Inc.
Tabletop centrifuges	Eppendorf AG Thermo Fisher Scientific Inc.
Tecan Infinite 200 Pro plate reader	Tecan Life Sciences Home
UV table	LTF Labortechnik
Vortex mixer	IKA-Labortechnik
Water bath	Grant Instruments Limited
XGI-8 Gas Anesthesia System	Xenogen

2.1.1 Cell lines

Cell line	Definition	Usage
LuCa6	Murine cell line isolated in our research group from a tumor in the lung cancer model Scgb1a1/CreERT2/K-Ras^{G12VlacZ}/p53$^{fl/fl}$ (CKP) [157].	Subcutaneous injection
RIL-175	Murine hepatocellular carcinoma cell line isolated from liver tumors generated in C57BL/6 mice through the transfer of p53$^{-/-}$ fetal hepatoblasts transduced with HRasv12 (Dr. Lars Zender (University of Tübingen, Tübingen, Germany).	Subcutaneous and intrasplenic injection
Dt81Hepa1-6/βgeo	Hepa1-6 clone was isolated from the BW7756 tumor, spontaneously arising in the C57BL6/J mouse strain. Lacoste *et al*. performed *in vivo* passage (intrasplenic injection) of Hepa1-6 cells in C57BL/6 mice. From this cell line, the Dt81Hepa1-6/βgeo cell line expressing the β-geo gene was established in our research group.	Intrasplenic injection
Hy15549	Cell lines was established from primary pancreatic tumors of Ptf1-Cre; LSL-KRAS-G12D; p53 Lox/+ mice in the laboratory of Dr. Nabeel Bardeesy at Harvard Medical School (Boston, MA, USA) [158].	Subcutaneous injection
FC1242	All three cell clones were isolated from K-rasLSL.G12D/+; Trp53R172H/+; Pdx-1-Cre mice and were provided to us by the Cold Spring Harbor Laboratory (New York, USA).	Subcutaneous injection
FC1245		Subcutaneous injection
FC1199		Subcutaneous injection

2.1.2 Chemicals and consumables

Table 2: Consumables

Consumables	Supplier
Cell counter slides	Bio-Rad Laboratories Inc.
Cell culture flasks (25 /75 /175 cm^2)	Greiner Bio One International GmbH
Cell culture plates (6 /12 /24 well)	Greiner Bio One International GmbH
Cell sieve (70 µm)	Greiner Bio One International GmbH
Cryo tubes	Greiner Bio One International GmbH
FACS tubes	BD Biosciences
MultiScreen HTS Filter Plates	Millipore Ireland BV
Nitrile gloves	Starlab International GmbH
Parafilm® sealing film	A. Hartenstein GmbH
Pasteur pipettes	Carl Roth GmbH + Co. KG
Petri dishes	Greiner Bio One International GmbH
Pipette tips (0.1-20 µl /10-200 µl /100-1000 µl)	Greiner Bio One International GmbH
Reaction tubes (1.5 ml /2 ml /5 ml)	Eppendorf AG
Reaction tubes (15 ml /50 ml)	Greiner Bio One International GmbH
Reaction tubes (200 µl)	Starlab International GmbH
Serological pipettes (5 ml / 10 ml/ 25 ml)	Greiner Bio One International GmbH
Suture material Vicryl 4-0	ETHICON
Syringe (5 ml /10 ml)	BD Biosciences
Wound clips AutoClip® System	Fine Science Tools

Table 3: Reagents and chemicals

Reagents	Supplier
1 kb DNA marker	Bio&SELL GmbH
100 bp DNA marker	Bio&SELL GmbH
2-Propanol	Merck KGaA
5x PCR mix “ready to load”	Bio&SELL GmbH
6x Gel loading dye	Thermo Fisher Scientific Inc.
Agarose basic	AppliChem GmbH
Ammonium chloride (NH_4Cl)	Carl Roth GmbH + Co. KG
Bovine serum albumin (BSA)	Carl Roth GmbH + Co. KG
Bupresol® vet. 0.3 mg/ml	cp pharma

Reagents	**Supplier**
Dimethylsulfoxid (DMSO)	Merck KGaA
DNA oligonucleotides	Metabion GmbH
Dulbecco's Modified Eagle's Medium (DMEM) GlutaMAX	Gibco™
Dulbecco's phosphate buffered saline (DPBS)	Sigma-Aldrich
EDTA 0.5 M	Thermo Fisher Scientific Inc.
Ethanol absolute	VWR International
Ethidium bromide solution 0.025%	Carl Roth GmbH + Co. KG
Ethylenediaminetetraacetic acid disodium salt dihydrate (EDTA)	AppliChem GmbH
Fetal calf serum (FCS)	Greiner Bio One International GmbH
Hydrogen peroxide (H_2O_2) 30%	Carl Roth GmbH + Co. KG
Isoflurane	Piramal Critical Care GmbH
Ketamin Hameln 50 mg/ml	Hameln pharmaceuticals
Mayer's hemalum solution	Sigma-Aldrich
Paraformaldehyde	Carl Roth GmbH + Co. KG
Penicillin-Streptomycin (Pen-Strep)	Life Technologies
Phenobarbital	Sigma Aldrich
Picric acid	Sigma Aldrich
Potassium bicarbonate ($KHCO_3$)	Carl Roth GmbH + Co. KG
Rapamycin	Thermo Fisher Scientific Inc.
Rompun 2%	Bayer vital GmbH
Roswell Park Memorial Institute (RPMI) 1640 GlutaMAX	Gibco™
Roti-Histokitt II	Carl Roth GmbH
Roti-plast paraffin	Carl Roth GmbH
Sodium chloride	Carl Roth GmbH + Co. KG
Tamoxifen (Tam)	Merck KGaA
Tissue protein extraction reagent (T-PER) buffer	Thermo Fisher Scientific Inc.
Tris(hydroxymethyl)aminomethan (TRIS)	AppliChem GmbH
Triton X-100	AppliChem GmbH
Trypan blue	Sigma-Aldrich
Tween 20	AppliChem GmbH
Xylene	AppliChem GmbH

Table 4: Media and buffer

Acidified water

5 ml glacial acetic acid

fill up to 1 l with H_2Odd

10 x Citrate buffer

0.04 M sodium citrate dihydrate

0.06 M citric acid

adjust to pH 6.0

fill up to 1 l with H_2Odd, sterile filtration

DMEM GlutaMAX comp.

DMEM GlutaMAX (Gibco™)

10% FCS (heat inactivated)

1% Pen-Strep (10,000 U/ml penicillin, 10 mg/ml streptomycin)

Erythrocyte lysis buffer

155 mM NH_4Cl

10 mM $KHCO_3$

0.1 mM EDTA

adjust to pH 7.4, sterile filtration

Flow cytometry buffer

1x PBS

1 – 2% BSA

2 mM EDTA

Fixation buffer

1 x PBS

4% paraformaldehyde

50 x TAE buffer

242 g Tris Base

57.1 ml Acetic acid

100 ml EDTA (0.5 M, pH 8.3)

fill up to 1 l with H_2Odd, dilute 1:10 with H_2Odd before use

Tail buffer

1 M Tris pH 8.0

5 M NaCl

0.5 M EDTA pH 8.0

10% SDS

10 x TBS

0.5 M Tris base

1.37 M NaCl

adjust to pH 7.6

fill up to 1 l with H_2Odd

Lysis buffer

40 µl Tail buffer

10 µl Proteinase K (10 mg/ml)

100x Mg solution

0.1 M MgCl2

4.5 M β-mercaptoethanol

RPMI GlutaMAX comp.

RPMI 1640 GlutaMAX (Gibco™)

10% FCS (heat inactivated)

1% pen-strep (10,000 U/ml penicillin, 10 mg/ml streptomycin)

Sirius Red solution

0.5 g Sirius Red powder

500 ml saturated picric acid

Sodium phosphate buffer

1 M Na_2HPO_4

1 M NaH_2PO_4

adjust to pH 7.5

fill up to 1 l with H_2Odd

Table 5: Kits

Kits	Manufacturer
Pierce™ BCA Protein Assay Kit	Thermo Fisher Scientific Inc.
ImmPACT® DAB Substrate Kit, Peroxidase (HRP)	Vector Laboratories, Inc.
Luna Universal Probe One-Step RT-qPCR	New England Biolabs GmbH
Vectastain ABC-Kit	Thermo Fisher Scientific Inc.

Table 6: Primer

Target gene		Primer sequence 5'-3'
18S	Fwd	GTA ACC CGT TGA ACC CCA TT
	Rev	CCA TCC AAT CGG TAG TAG CG
α-SMA	Fwd	GAC TAC TGC CGA GCG TGA G
	Rev	GTC AGC AAT GCC TGG GTA CA
CD206	Fwd	TTG GAG GCT GAT TAC GAG CAG TG
	Rev	GGA CAT GCC AGG GTC ACC TTT
CD38	Fwd	AAG ATG CCT GTG GTG TGG TCC
	Rev	CTT GAA CAT GCG TTA CTG GAA GC
Col1a1	Fwd	GGA GAG AGC ATG ACC GAT GG
	Rev	AAG TTC CGG TGT GAC TCG TG
Col3a1	Fwd	GAA AGA GGA TCT GAG GGC TCG
	Rev	GGG TGA AAA GCC ACC AGA CT
Fra-2	Fwd	CAC TCC CGG CAC TTC AAA C
	Rev	GAG TCT GAT GAT GAC TGG TCC CC
GAPDH	Fwd	TCC ACT CAC GGC AAA TTC AAC
	Rev	CGC TCC TGG AAG ATG GTG ATG
IL-10	Fwd	AGC CTT ATC GGA AAT GAT CCA GT
	Rev	GGC CTT GTA GAC ACC TTG GT

Target gene		Primer sequence 5'-3'
iNOS	Fwd	TTG GTG AAG GGA CTG AGC TGT T
	Rev	AAG AGA AAC TTC CAG GGG CAA GC
PPIA	Fwd	GCC GAT GAC GAG CCC TTG G
	Rev	CCC TGG CAC ATG AAT CCT GGA A
Tbp	Fwd	TGG AAT TGT ACC GCA GCT TCA AAA T
	Rev	GCA GTT GTC CGT GGC TCT CT
TGFβRII	Fwd	GAG TCG TTC AAG CAG ACG GA
	Rev	GAA CCA AAT GGG GGC TCG TA
YM1	Fwd	AGA AGG GAG TTT CAA ACC TGG T
	Rev	GTC TTG CTC ATG TGT GTA AGT GA

Table 7: Primary antibodies

Antigen	Antibodies	Application	Source	Article no.	Dilution
α-SMA	anti-α-SMA	IHC	Abcam	ab124964	1:1000
CD3	anti-CD3	IHC	Abcam	ab5690	1:250
CD4	anti-CD4	IHC	Abcam	ab 183685	1:400
CD4	anti-CD4	FC	BD Horizon™	612952	1:100
CD8	anti-CD8α	IHC	Abcam	ab 237723	1:200
CD8	anti-CD8 α	FC	Biolegend®	100707	1:500
CD11c	anti-CD11c	FC	Biolegend®	337225	1:200
CD25	anti-CD25	FC	Biolegend®	302609	1:100
CD31	anti-CD31	FC	Biolegend®	102407	1:500
CD45	anti-CD45	FC	Biolegend®	110729	1:200
CD68	anti-CD68 y	IHC	Abcam	ab 125212	1:200
CD68	anti-CD68	FC	Biolegend®	137001	1:100
CD86	anti-CD86	FC	Biolegend®	105011	1:100
CD206	anti-CD206	FC	Biolegend®	141707	1:100
Col1a1	anti- Col1a1	IHC	Cell Signaling Technology	72026T	1:400
F4/80	anti- F4/80	FC	Biolegend®	123111	1:200
FoxP3	anti-FoxP3	IHC	Cell Signaling Technology	#12653S	1:600
Granzyme B	anti-Granzyme B	IHC	Abcam	ab255598	1:2000
Ly6G	anti-Ly6G	FC	BD Horizon™	552093	1:500

Antigen	Antibodies	Application	Source	Article no.	Dilution
MHCII	anti-MHCII	FC	BD Horizon™	563414	1:500
pSMAD2	anti-pSMAD2	IHC	Cell Signaling Technology	3108S	1:100
Vimentin	anti-Vimentin	IHC	Abcam	ab92547	1:400
YM1	anti-YM1	IHC	StemCell Technologies	#60130	1:300

Table 8: Secondary antibodies

Antigen	Antibodies	Application	Source	Article no.	Dilution
IgG rabbit	Goat anti-rabbit IgG heavy and light chain (HRP)	IHC	Abcam	ab205718	1:1000 - 1:10000
IgG rat	Goat anti-rat IgG heavy and light chain (HRP)	IHC	Abcam	ab6845	1:1000

Table 9: Software

Software	Source
BD FACSDivaTM	Becton, Dickinson and Company (Ashland, USA)
FlowJo Single Cell Analysis Software	Becton, Dickinson and Company (Ashland, USA)
GraphPad 9.5.1	Prism (La Jolla, USA)
ImageJ 1.8.0	National Institute of Health (Maryland, USA)
Image Lab 6.0.1	Bio-Rad Laboratories Inc. (Hercules, USA)
Microsoft Office	Microsoft (Redmond, USA)

2.2 Methods

2.2.1 Molecular biology

2.2.1.1 Polymerase chain reaction

The polymerase chain reaction (PCR) is used for the quantitative amplification of a DNA segment using oligonucleotide primers. In the initial denaturation step at 95 °C, the DNA double strand separates into single strands. The primers then anneal to the desired base sequence (primer annealing). The final reaction step involves elongation by a DNA polymerase. One PCR reaction tube (0.2 ml) contained the master mix, both primers (forward and reverse), the DNA and H_2Odd, in a total volume of 25 µl. The negative control consisted of all components except the DNA. All PCR reactions were performed using an automated thermocycler programmed as follows:

Table 10: Standard PCR protocol for amplifying the target DNA

Step	Time	Temperature	
Denaturation	1 min	95 °C	
Primer annealing	30 s	60 °C	⎫
Elongation	45 s	72 °C	⎬ 30 cycles
Finale elongation	10 min	72 °C	⎭
Cooling	∞	4 °C	

2.2.1.2 Agarose gel electrophoresis

Agarose gel electrophoresis was used for the separation of DNA. Agarose gels were prepared by blending agarose in Tris-Acetate-EDTA (TAE) buffer to achieve a final concentration of 2% (fragments of 0.1 – 1 kb). The mixture underwent microwave heating until the agarose was completely dissolved. To visualize the bands, a drop of 0.025% ethidium bromide was added and the solution was poured into a horizontal chamber. Once the gel had set, DNA samples were loaded onto it with the appropriate amount of 6-fold gel loading dye. The electrophoresis was performed in TAE buffer at 120 V for 30 to 60 min. Gene ladders were included as size reference. DNA fragments were visualized using UV light.

2.2.2 Cell culture

2.2.2.1 Passaging of cells

In this thesis, exclusively adherent cell lines were used, cultivated in Dulbecco's Modified Eagles Medium (DMEM) supplemented with 1% penicillin/streptomycin (pen/strep) and 10% fetal calf serum (FCS). Cells were cultured in either T75 or T175 flasks and underwent passaging before reaching confluence to prevent contact inhibition of growth. First, the old medium was removed, and cells were rinsed with 10 ml of Dulbecco's Phosphate Buffered Saline (DPBS). Subsequently, 2 to 4 ml of Trypsin-EDTA was added based on the volume of the cell culture flask, followed by a 1-minute incubation period. Trypsin-EDTA was removed, and cells were incubated until they were detached, but not longer than 10 min. Detached cells were then transferred into a reaction tube and centrifuged at 1.500 rpm for 5 min at room temperature (RT). The supernatant was decanted, and the pellet resuspended in 5 ml PBS followed by a second centrifugation. The resulting cell pellet was resuspended in 1 to 5 ml DMEM and the cell count was determined using a Neubauer counting chamber. The specified cell number was placed in a new cell culture flask preloaded with fresh medium. Cultivation took place in a CO_2 incubator at 37 °C and 5% CO_2.

2.2.2.2 Freezing and thawing of cell lines

For long-term storage, cells were frozen. Therefore, one sub-confluent T175 flask was used. The media was removed, and cells were washed with 10 ml DPBS. After detachment from the bottom with 1 to 2 ml Trypsin-EDTA, fresh medium was added to inactivate trypsin. After centrifugation for 5 min at 1.500 rpm, the cell pellet was resuspended and 1 x 10^6 cells were aliquoted in 1 ml freezing medium containing 90% FCS and 1 % DMSO. Each cell suspension was transferred to a cryo vial and slowly frozen to -80 °C in a specialized cryo-box. Cells can remain some days at -80 °C but should be frozen in liquid nitrogen for a long-term storage.
Upon thawing, it was crucial to rapidly combine the cells with the respective medium to prevent any toxic effects and osmotic shock arising from high intracellular concentrations of DMSO. Following centrifugation at 1.500 rpm for 5 min, the supernatant was removed, and the pellet was resuspended in PBS. After an additional centrifugation step, the supernatant was discarded, and the pellet was resuspended in culture medium for transfer into a cell culture flask. Cells were cultivated in an incubator at 37 °C and 5% CO_2.

2.2.2.3 Mycoplasma test

Our research group has established a universal protocol for routine mycoplasma testing using PCR. This method was published in iScience [159]. All steps were carried out according to the instructions outlined in the mentioned publication.

2.2.2.4 Counting of cell numbers

Ensuring the accurate and precise determination of cell concentration and viability is essential to uphold optimal culture conditions. Both was determined with a Neubauer cell counting chamber. For cell quantification, 10 µl of cell suspension were mixed with 10 µl of trypan blue solution. The resulting mixture was loaded into a Neubauer cell counting chamber using 10 µl. The trypan blue dye exclusion technique enabled the differentiation between viable and non-viable, blue-colored, cells. The counting and calculation were performed by the following formula:

$$\text{cell number/ml} = \text{Mean value of counted cell numbers} \times \text{dilution factor (2)} \times 10^4 \text{ cells/ml}$$

Formula 1: Calculation of the cell number per ml.

Cells were diluted as required for further usage.

2.2.2.5 Protein quantification via BCA assay

Protein concentration of supernatants was measured using the Pierce™ Bicinchoninic Acid (BCA) protein assay kit (Thermo Fisher Scientific) according to the manufacturer's instructions. This colorimetric assay provides a quick and efficient method for protein quantification. The samples were incubated with the BCA reagent for 30 min at 37 °C. Following incubation, the absorbance was measured at 562 nm using a Tecan plate reader.

2.2.3 Animals

All experiments involving animals were approved by the ethics committee on animal care of Rheinland-Pfalz (Landesuntersuchungsamt Koblenz, LUA) under the file reference G 23-1-007 and G20-1-045. The breeding of mouse strains was implemented in compliance with the regulations and under the supervision of the Translational Animal Research Center (TARC), Johannes Gutenberg University Mainz. Wild type C57BL/6N mice were purchased from Charles River. Mouse colonies were held and bred under specific pathogen-free (SPF) conditions following a 12 h light, 12 h dark cycle. The start of the experiments was scheduled one week after arrival of the mice providing a minimum adaptation period.

2.2.3.1 Mouse strains and transgenic mice

For mouse experiments, C57BL/6N wild-type mice, as well as transgenic mouse models were used (Table 11). In our research group, several mouse models were generated under the supervision of the TARC. A bi-transgenic mouse model was developed, incorporating a Col3a1 promoter-driven and estrogen-inducible Cre expression in combination with a floxed TGFβ type II receptor (Col3a1-CreERT2/TGFβRII fl/fl mouse; [160]). TGFβRII knock-out in MF/CAFs was induced by tamoxifen (Tam) administration (Fig. 12). During this thesis, a novel mouse strain was established by crossing the Col3a1-CreERT2 strain with the iDTR mouse strain. The expression of the diphtheria toxin receptor (DTR) is normally inhibited by a *loxP*-flanked STOP sequence. After activation of Cre recombinase, the STOP sequence will be deleted in cells with active Cre, permitting DTR expression. Subsequent administration of diphtheria toxin (DT) leads to the induction of apoptosis in MF/CAFs expressing DTR, without showing toxic effects on the mice themselves (Fig. 13).

Table 11: Mouse strains

Strain	Source
C57BL/6N	Charles River
Col3a1-CreERT2	In-house breeding
TGFβRII fl/fl	In-house breeding
Col3a1-CreERT2/TGFβRII fl/fl	In-house breeding
iDTR	Kindly provided by Prof. A. Waisman
Col3a1-CreERT2/iDTR	Established during this thesis

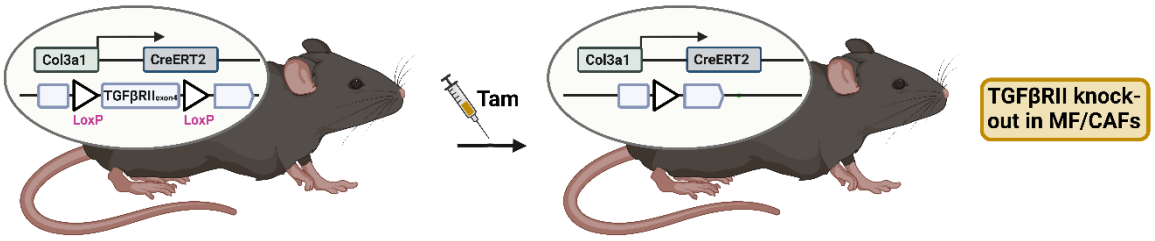

Figure 12: Schematic representation of the Col3a1-CreERT2/TGFβRII fl/fl mouse model. Upon injection of tamoxifen (Tam), Cre-dependent excision of exon 4 of the TGFβRII receptor leads to its inactivation in MF/CAFs (created with BioRender.com).

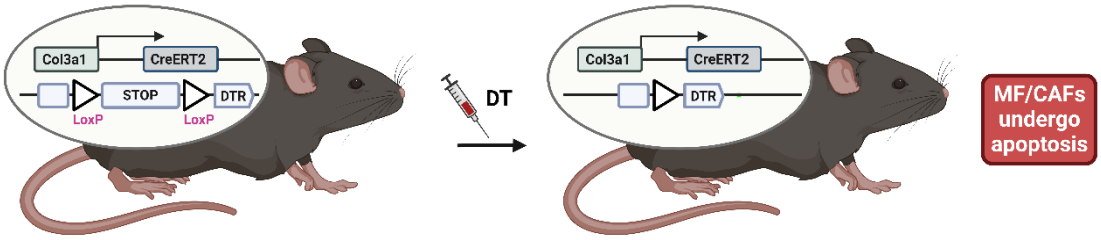

Figure 13: Schematic representation of the Col3a1-CreERT2/iDTR mouse model. The Cre-inducible expression of DTR in this mouse strain results in the depletion of MF/CAFs upon administration of diphtheria toxin (DT) (created with BioRender.com).

2.2.3.2 Genotyping

To determine the genotype of transgenic mouse models, one ear punch from each mouse was incubated with 50 µl lysis buffer at 56 °C for at least 4 h or overnight at 37 °C. The enzymatic reaction was terminated by adding 150 µl autoclaved H_2Odd and boiling at 99 °C for 5 min. Subsequently, samples were centrifuged at 14.000 rpm for 5 min and 1 µl of the DNA-containing supernatant was used for each genotyping PCR reaction. Agarose gel electrophoresis (see section 2.2.1.2) was performed to confirm the accurate genotype of a mouse.

Primers and expected PCR product sizes are listed in Table 12.

Table 12: Sequences of primers and band sizes of the expected PCR fragments

Target gene	Primers	Primer sequence 5'-3'	Expected band size
Col3a1-CreERT2	CreERT2_Col3a1_Fwd	TCG CTG CAT TAC CGG TCG ATG C	430 bp
	CreERT2_Col3a1_Rev	CCA TGA GTG AAC GAA CCT GGT CG	
TGFβRII fl/fl	TGFβR2flfl_Fwd	TGT AAT CGT TGC ACT CTT CCA TGT	mutant = 575 bp wild-type = 420 bp
	TGFβR2flfl_Rev	GCA CAG GTA CAC ATC TCT GCA C	
iDTR	R26mut	GCG AAG AGT TTG TCC TCA ACC	mutant = 300 bp wild-type = 603 bp
	R26WT	GGA GCG GGA GAA ATG GAT ATG	
	R26com	AAA GTC GCT CTG AGT TGT TAT	

2.2.3.3 Anesthesia of mice with isoflurane

Isoflurane functions as an inhalation anesthetic that acts as a muscle relaxant and provides analgesic effects as well. During injections, both subcutaneously and orthotopically, the mice were anaesthetized through a nose-cone using a specialized ventilation apparatus with a mixture of isoflurane and oxygen (2.5-4% isoflurane plus O_2, flow rate 2-3 l/min).

2.2.3.4 Subcutaneous (s.c.) mouse models

For subcutaneous tumor implantation, both C57BL/6N wild type mice and transgenic mouse models were employed (see section 2.2.3.1). The wild type mice were exclusively used for the initial establishment phase, specifically for testing different cell numbers. The desired cancer cell line of one of the various tumor entities (lung, liver or pancreas) was thawed at least 7 days before use and expanded prior tumor inoculation. Cells were cultured in cell culture flasks until reaching 80% confluence, and the preparation proceeded as follows:

The cells were harvested by trypsinization, and the resulting cell suspension was then centrifuged at 1.500 rpm for 5 min. After two washing steps of the pellet with an equivalent volume of PBS, cell counting was performed as previously described (see section 2.2.2.4). Then, the cell pellet was resuspended in an appropriate volume of ice-cold PBS and cells were kept on ice until usage. Subsequently, the cancer cells were subcutaneously implanted into the flank of the mice in a 100 µl volume using a 29 G sterile needle and syringe. Prior to implantation, the injection site was disinfected with 70% ethanol to prevent bacterial infections. Upon the formation of small solid tumors in the flank of the injected mice, tumor burden was examined by measuring tumor length and width using a digital caliper twice per week. Once the tumor reached a diameter of 10 mm, measurements were taken every other day. In the case of a rapidly growing cancer cell line, daily measurements were performed. Also, the weight of mice bearing tumors was regularly documented and the overall fitness was checked throughout the experiment.

The tumor volume was calculated using the following formula:

$$\text{Tumor volume} = \text{length (mm)} \times \text{width (mm)}^2 \times 0.52$$

Formula 2: Calculation of the tumor volume.

2.2.3.5 Orthotopic HCC tumor models

The RIL-175 or Dt81Hepa1-6/βgeo cell line was trypsinized and washed in PBS through two centrifugation steps at 1.500 rpm for 5 min each. After that, the cells were resuspended at the desired concentration in a saline solution containing 0.25% albumin. To induce orthotopic HCC, a surgery for intrasplenic injection was performed. For pain relief, all mice received one s.c. injection of buprenorphine (0.1 mg/kg in 0.9 % NaCl) into the skin over their neck approx.

30 min pre-surgery. During the surgical procedure, the animals were exposed to isoflurane anesthesia (see section 2.2.3.4). Once the mice were asleep, they were placed on a heating pad with their nose in a nose-cone. To prevent corneal drying, a small amount of eye ointment was applied. Subsequently, the mice were placed in a lateral position on their right side. The surgical area was shaved and sterilized with 70% ethanol. The abdominal cavity was accessed via a subcostal incision and the spleen with its associated ligaments was carefully pulled out using forceps. The previously prepared HCC cells were slowly injected in a volume of 100 µl into the spleen. Once the spleen regained its deep red color, the needle was gently retracted, and one single drop of surgical glue was applied to prevent blood loss and cell leakage. The spleen was carefully returned to its original position and the abdominal incision was closed using sutures and wound clips. For post-operative pain management, buprenorphine (0.009 mg/ml) was included in the drinking water for three days. Once again, the weight of the mice and their overall fitness were recorded throughout the duration of the experiment.

2.2.3.6 Preparation of tamoxifen (Tam) solution

For the induction of Cre-recombinase activity in mice, a tamoxifen (Tam) solution was prepared. Therefore, 1 g of Tam powder was dissolved in 10 ml of methanol at 37 °C. After that, the mixture was united with 90 ml of autoclaved sunflower oil and shaken overnight at RT. The resulting homogeneous solution was aliquoted into 2 ml reaction tubes and stored at -20 °C. 2 mg of Tam were injected intraperitoneally (i.p.) in Col3a1-CreERT2/TGFβRII fl/fl mice, resulting in Cre activation for the specific TGFβRII knock-out in CAFs. The total number and timing of the injections depended on the experimental design. For a short period of time, Tam was kept at 4 °C, always protected from light.

2.2.3.7 Blood extraction and serum preparation

For a complete blood count of the mouse, at least 10 µl blood from the facial vein were collected in an EDTA tube and then analyzed using the scil Vet abc Plus+™. For serum preparation 0.5 to 1 ml blood were obtained via cardiac puncture. The blood clotted within 15 to 30 min at RT. Centrifugation at 1.000 to 2.000 x g for 10 min was performed to separate the serum from the clot. The serum in the supernatant was immediately transferred into a new 1.5 ml tube and stored at -20 °C.

2.2.3.8 Isolation of single-cell suspension from primary tissue

Animals were sacrificed by cervical dislocation. Carefully dissected s.c. tumors were placed in a Petri dish on ice containing PBS. The tumor tissue was briefly rinsed and then minced into

small fragments within a 2 ml tube using scissors. The prepared fragments were transferred into a 50 ml Falcon tube each, with the volume adjusted to 5 ml using PBS. To initiate digestion, 1.2 ml of collagenase/dispase (derived from a 10 mg/ml stock solution in H_2O/PBS) was added to the Falcon tube, resulting in a final collagenase/dispase concentration of approx. 2 mg/ml and the mixture was shaken for 45 min at 37 °C. The digested tissue was then placed on ice. For further processing, 25 µl of DNAse I per 6 ml of the digest solution (from a 1% stock solution of 10 mg/ml) was added, achieving a final DNAse I concentration of around 0.025 mg/ml. After inverting the solution several times, it was left on ice to cool, not exceeding 5 min. Following this, the digested tissue was filtered through a 70 µm filter into a new 50 ml tube. After centrifugation at 1.500 rpm for 5 min, the supernatant was discarded, and the red blood cell (RBC) lysis protocol was performed for RBC elimination.

2.2.3.9 Red blood cell lysis

The single-cell pellet obtained in section 2.2.3.8 was resuspended in 2 ml erythrocyte lysis buffer and incubated for 3 min at 4 °C. To stop the reaction, 10 ml of DMEM were added, followed by centrifugation for 5 min at 1500 rpm. The supernatant was discarded, and the remaining pellet was resuspended in PBS for cell counting and FC staining.

2.2.3.10 Flow cytometry (FC)

Flow cytometry serves as a technique for detecting and quantifying the expression of intracellular or extracellular surface markers in individual cells. The staining process includes preparing a single-cell suspension from tissue samples (see section 2.2.3.8). Single cells, stained with fluorescence-labelled antibodies, can be allocated to a cell population by passing a laser system, generating characteristic sideward scatter (SSC) and forward scatter (FSC). Depending on the cell yield, 1 x 10^5 to 1 x 10^6 cells per tube were stained. Therefore, cells were incubated with the labeled antibody (directly labeled) in a volume of 200 µl FC buffer for 30 min on ice and protected from light. After incubation, stained cells were centrifuged for 5 min at 1.500 rpm at 4 °C and the supernatant was discarded. Then, 500 µl FC buffer were added and the tube was gently vortexed. The washing procedure was repeated three times and afterwards cells were resuspended in 300 µl FC buffer and were ready for measurement. 7-amino-actinomycin D (7-AAD) is a ready-to-use fluorescent dye that intercalates into double-stranded DNA and was used for live/dead cell discrimination, following the manufacturer's instructions (BD Pharmingen™ 7-AAD). Flow cytometric data were acquired using a BD FACSSymphony™ flow cytometer and analyzed using FlowJo V10 (BD Biosciences).

2.2.3.11 RNA extraction and RT-qPCR

For optimal RNA release, whole preserved organs were mechanically disrupted using a bead homogenizer (Tissue Lyser II, Qiagen). All further steps were performed according to the manufacturer's instructions of the Monarch Total RNA Miniprep Kit. The RNA concentration was determined by a Nanodrop spectrophotometer. Afterwards, the NEB Luna Universal Probe One-Step RT-qPCR Kit was used to quantify target RNA. This involved a one-step process converting RNA into cDNA in a single tube, followed by amplification for quantification via qPCR.

2.2.3.12 Quantitative assay for β-galactosidase

A 4-Methylumbelliferyl-β-D-galactopyranoside (MU-Gal) assay was performed to measure the activity of the enzyme β-galactosidase in liver tissue samples of mice. This assay utilizes the fluorogenic substrate MU-Gal, which, upon enzymatic hydrolysis by β-galactosidase, releases 4-methylumbelliferone (4-MU), a fluorescent compound. The fluorescence of 4-MU can then be measured to quantify the enzyme activity. Therefore, liver tissue samples were thawed and pulverized under liquid nitrogen. The pulverized tissue was then extracted with T-PER tissue extraction buffer (5 ml/g tissue) for 20 min on ice. Following extraction, the samples were centrifuged at 3.500 rpm for 10 min at 4 °C. The resulting supernatant was aliquoted and stored either at 4 °C for short-term use or at -20 °C for long-term storage. To perform the β-galactosidase assay, a reaction mixture was prepared containing 3 µl of 100x Mg solution, 15 µl of MU-Gal substrate (1.7 mM final conc.), 5 µl of protein extract and 277 µl of sodium phosphate buffer. Fluorescence measurements were carried out in triplicates using a Tecan plate reader, with readings taken at 5 min intervals. The obtained results were normalized to protein concentration determined by BCA assay.

2.2.4 Histology and microscopy

2.2.4.1 Tissue paraffin-embedding

To generate paraffin-embedded sections, s.c. tumors or the particular organ of interest was extracted from the mouse and rinsed twice in PBS. After that, the tissue was placed in a pre-labeled histology cassette, following fixation in a container/glass containing ice-cold paraformaldehyde (PFA; 4%) over night or until the dehydration and paraffinization steps were performed using a tissue infiltration machine. The tissue was immersed in H_2Odd and passed through a series of dehydration steps by exposure to increasing concentrations of isopropanol: 70%, 80% and 95%. The tissue was then treated three times with 100% isopropanol. After

dehydration, the samples were immersed with xylene. Finally, the tissue was left in liquid paraffin until embedding.

Tissue embedding was carried out using the Leica EG1150 modular tissue embedding center with an incorporated cooling plate and the EG1150H heated embedding module, following the manufacturer's instructions.

2.2.4.2 Microtome sectioning

A microtome was employed for sectioning FFPE (formalin-fixed paraffin-embedded) material. The blocks were cooled to facilitate cutting and were trimmed before obtaining the first section. Paraffin sections were sliced at a thickness of 4 - 6 µm, positioned in warm water (42 °C), and subsequently transferred to a glass slide once fully extended. Dried slides were stored at RT until they were used for several staining methods, including immunohistochemistry (IHC), hematoxylin and eosin (H&E) or Sirius Red (SR) staining.

2.2.4.3 Immunohistochemistry

To eliminate paraffin, tissue sections underwent two incubation steps in xylene (2× 10 min each). Deparaffinized sections were then rehydrated through a series of alcohol and water washes (2× 100% isopropanol for 10 min, 2× 95% isopropanol for 10 min, 2× 75% isopropanol for 10 min, and 2× H2Odd for 5 min). Antigen retrieval was carried out using a 10 mM sodium citrate buffer at pH 6.0 in a steam cooker for 45 min, followed by a cool down and a washing step in H2Odd for 5 min. To inhibit endogenous peroxidase activity, tissue sections were treated with 3% hydrogen peroxide (H_2O_2) in H_2Odd for 15 min and subsequently washed again for 2× 5 min in H2Odd. Blocking was accomplished by incubating the sections with 2.5% normal horse serum for 1 h. In every case, primary antibodies (see Table 7) were diluted in TBS-T (1% bovine serum albumin in TBS containing 0.1% Triton X-100), applied to the sections, and allowed to incubate in a dark humid chamber at 4 °C overnight. On the following day, the sections were washed twice in TBS-T for 10 min, and then secondary antibodies were applied. For primary rabbit antibodies, sections were treated with an HRP-labeled secondary goat anti-rabbit IgG antibody for 1 hour. If primary rabbit antibodies were used, sections were incubated with a biotinylated anti-rat IgG for 1 h, underwent a 10 min washing step in TBS-T, and then proceeded to an ABC-Kit for signal amplification. In each case, DAB staining was performed and finished with a final tap water rinse. This was followed by counterstaining with hematoxylin, dehydration through sequential incubations in 95% ethanol, 100% ethanol, and

2× xylene (each lasting 10 sec) and mounting with Roti Histokit II. Finally, the slides were sealed with coverslips.

2.2.4.4 Hematoxylin and eosin staining

Deparaffinization and rehydration of the sections were performed following the procedure outlined in section 2.2.4.3. For hematoxylin and eosin (H&E) staining, sections underwent a 5 min staining with hematoxylin, followed by a 10 min washing step under running tap water. Subsequently, the sections were stained with acidified eosin for additional 3 min before being rinsed in deionized water. To complete the process, sections were dehydrated in reverse order, followed by two 5 min incubations in xylene. Finally, the sections were mounted with Roti Histokit II, coverslips were applied, and the slides were allowed to dry.

2.2.4.5 Sirius red staining

Deparaffinization and rehydration of the sections performed based on the protocol in section 2.2.4.3. For Sirius Red (SR) staining, sections were immersed in the SR solution for 30 min. Subsequently, they were rinsed in H2Odd, followed by 2x 5 min washes in acidified water (0.005%). The sections were then dehydrated and mounted as described in the preceding sections.

2.2.5 Quantitative data analysis

For quantitative data analysis the GraphPad Prism 9.5.1 software was used. Results are presented as mean ± standard deviation (SD) unless noted otherwise. Significance levels are indicated as *$p < 0.05$, **$p < 0.01$, ***$p < 0.001$ and ****$p < 0.0001$, with unmarked comparisons indicating no significant difference. For comparisons between two groups, a two-tailed unpaired Student's t-test was performed. One-way analysis of variance (ANOVA) was applied to evaluate differences across three or more groups.

3 Results

3.1 Lung cancer

3.1.1 Influence of TGFβRII K.O. in CAFs on tumor growth and TME

Subcutaneous tumors were induced by injecting the LuCa6 mouse lung carcinoma cell line beneath the skin on both the right and left flank of homozygous Col3a1-CreERT2/TGFβRII fl/fl and heterozygous Col3a1-CreERT2/TGFβRII fl/- mice, serving as controls. A total of $7x10^5$ cells were injected in the right flank, while $3x10^5$ cells were injected in the left flank of the mice with 3-4 mice per experimental group. Two groups were examined: an early Tam (tamoxifen) group, receiving Tam (2 mg) via intraperitoneal administration three days post LuCa6-inoculation, and a late Tam group, with the first Tam administration initiated ten days after inoculation. Tam injections, occurring every 3 to 4 days, facilitated Cre activation, resulting in TGFβRII knockout in CAFs of Col3a1-CreERT2/TGFβRII fl/fl mice, while TGFβRII remained active in the control group. At day 21, all mice were sacrificed and further analyzed (Fig. 14A). The tumor progression in the early Tam group is illustrated in Fig. 14B. The left side of the illustration shows the tumor development corresponding to the higher cell count (right flank), with an average tumor volume of approx. 700 mm^3 in the control group in contrast to a smaller median tumor volume of 200 mm^3 observed in the floxed group. The right side of the figure outlines the progression of tumors with the lower cell count (left flank), revealing a tumor volume of about 150 mm^3 in the control group and approx. 50 mm^3 in the K.O. group. The tumor progression in the late Tam group is depicted in Fig. 14C. On the left, tumors in the control group measure approx. 500 mm^3, while knockout mice bear smaller tumors with a volume of around 300 mm^3. There is a noticeable trend toward reduced tumor volume when Tam is administered early, though this difference is not yet statistically significant. On the right, aligned with the lower number of injected cells, there is no difference in the tumor development between the groups, demonstrating tumor volumes around 100 mm^3.

The tumor volume at the endpoint of the experiment is shown in Fig. 14D. The early Tam administration time point revealed a significant reduction in tumor burden in the knockout group compared to the control group, whereas no significant difference in tumor development was observed in the late tamoxifen group. While not yet a significant effect on tumor size could be documented from caliper measurements of the flank, there was a strong trend in the two early knockout settings (early Tam) independent from the administered cell number, indicating that tumor growths was strongly inhibited by inactivation of TGFβRII signaling in CAFs compared to the control group with fully functional CAFs. After sacrifice and preparation of the s.c. tumors, the tumor volume was re-measured and a clearly significant difference in tumor growth of the

early Tam group could be observed. In Fig. 14E the *ex vivo* images of all subcutaneous LuCa6 tumors from both the early and late Tam groups are shown. It should be noted that while the observed trend in the *in vivo* measurements showed a clear tendency toward reduced tumor growth in the early Tam group, the limited number of mice per group (3-4) likely prevented these differences from reaching statistical significance. The more pronounced and statistically significant differences observed in the isolated tumors (Fig. 14D) compared to the *in vivo* measurements could be attributed to the absence of peritumoral edema, which might have masked the actual tumor size differences during caliper measurements in the living animals.

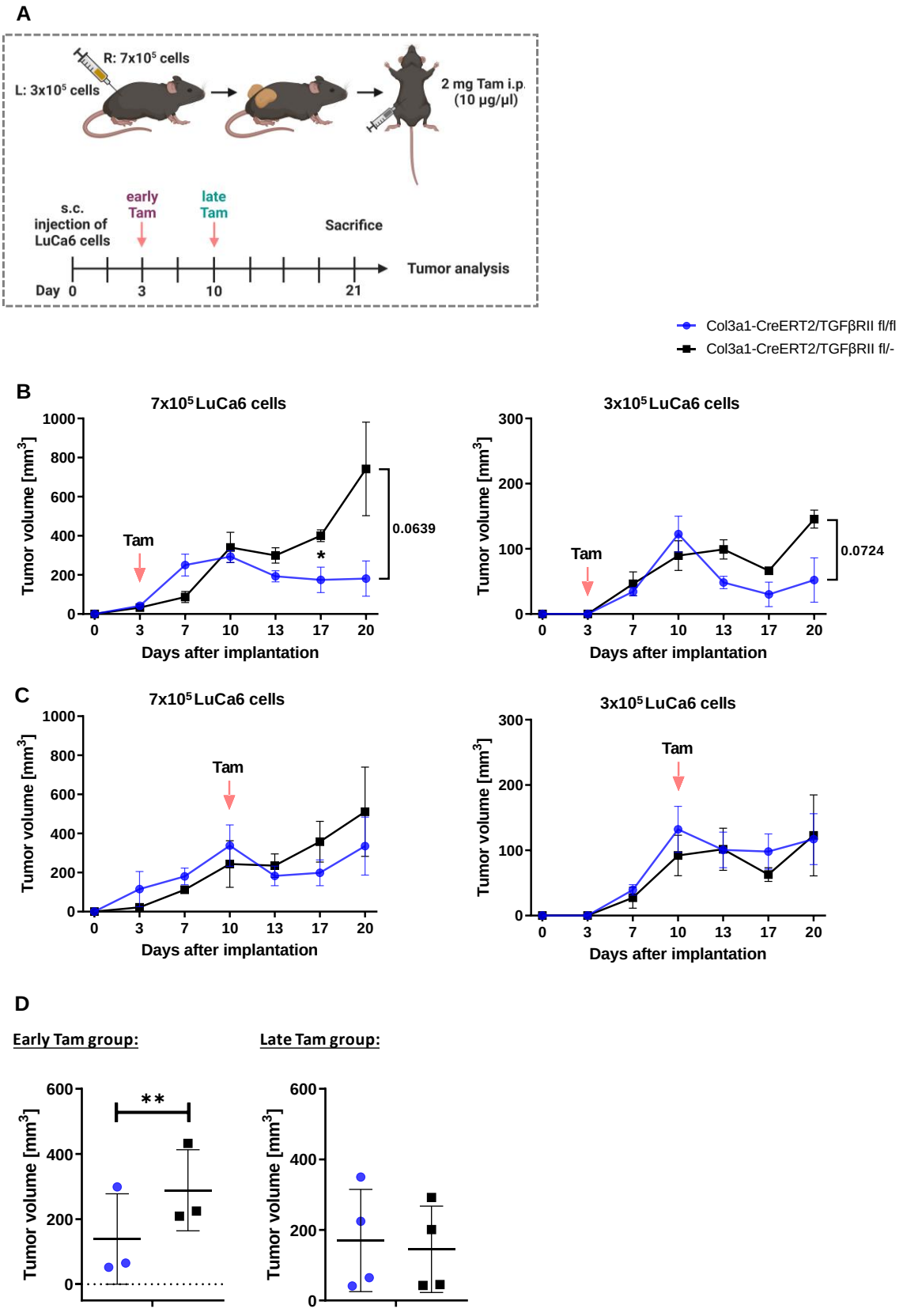
A
R: 7x10⁵ cells
L: 3x10⁵ cells
2 mg Tam i.p.
(10 µg/µl)
s.c.
injection of
LuCa6 cells
early
Tam
late
Tam
Sacrifice
Tumor analysis
Day 0
3
10
21
Col3a1-CreERT2/TGFβRII fl/fl
Col3a1-CreERT2/TGFβRII fl/-
B
7x10⁵ LuCa6 cells
3x10⁵ LuCa6 cells
Tumor volume [mm³]
Tam
0.0639
0.0724
*
Days after implantation
C
7x10⁵ LuCa6 cells
3x10⁵ LuCa6 cells
Tumor volume [mm³]
Tam
Days after implantation
D
Early Tam group:
Late Tam group:
Tumor volume [mm³]
**

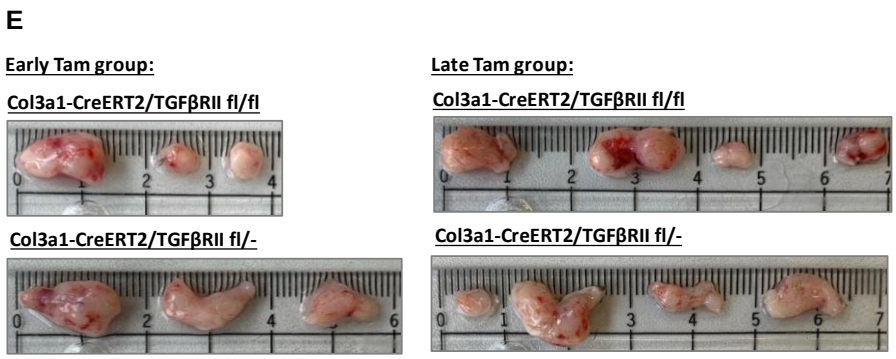

Figure 14: Impact of TGFβRII knockout in CAFs on desmoplastic LuCa6 lung tumors. **A.** Experimental design for subcutaneous tumor induction in Col3a1-CreERT2/TGFβRII fl/fl and Col3a1-CreERT2/TGFβRII fl/- mice. Tamoxifen administration (2 mg i.p.) schedules, early and late, were employed to explore TGFβRII K.O. effects in CAFs and on tumor growth (created with BioRender.com). **B.** Tumor progression in the early Tam group: volumes of tumors arising from $7x10^5$ cells (left side) and from $3x10^5$ cells (right side). **C.** Tumor progression in the late Tam group: volumes of tumors arising from $7x10^5$ cells (left side) and from $3x10^5$ cells (right side). **D.** Tumor volumes from 7x105 cells of the isolated, encapsulated tumors measured after sacrifice. **E.** *Ex vivo* images of s.c. LuCa6 tumors from both early and late Tam groups from tumors originated from an initial inoculum of $7×10^5$ cells. (*$p < 0.05$, **$p < 0.01$, n = 3-4/group).

To gain insight into collagen deposition in the subcutaneous LuCa6 tumors, Sirius Red staining was performed, comparing collagen deposition and distribution between the tumor margin and core. This analysis focuses on and presents data from tumors exhibiting a higher cellular density ($7x10^5$ cells), with 3-4 tumors per group selected for detailed examination. In the early Tam group, collagen deposition was notably higher in tumor margins (Fig. 15A) compared to tumor cores (Fig. 15B), showing a similar trend in both groups. The floxed group demonstrated approx. 40% positive Sirius Red stained area relative to the total tumor section area analyzed in the tumor margin (capsule), while the control animals showed around 35%. Within the tumor cores, collagen expression was around 10% in the floxed group and 15% in the control group.

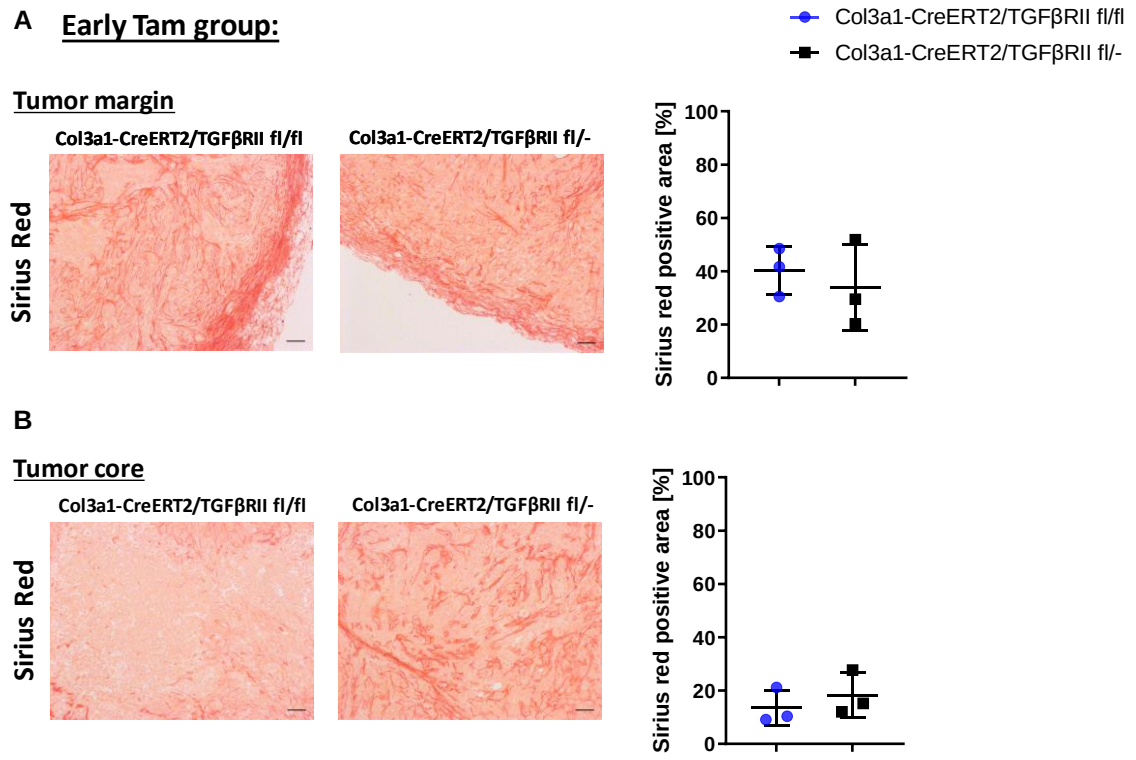

Figure 15: Histological- morphometric analysis of Sirius Red stained sections of the early Tam group. Distribution of collagen fibers stained with Sirius Red in the tumor margin (**A.**) and tumor core (**B.**) of subcutaneous (s.c.) LuCa6 tumors from Col3a1-CreERT2/TGFβRII fl/fl and Col3a1-CreERT2/TGFβRII fl/- mice is shown. Quantitative analysis of the positive stained area is presented. For each tumor, between 5-10 high power fields (20× magnification) were analyzed per region (margin and core). Results are expressed as mean values ± SD. Scale bar = 100µm. n = 3/group.

In the late Tam group, collagen deposition was prominent in the tumor margins (Fig. 16A) compared to the tumor cores (Fig. 16B), a consistent observation in both groups. While not reaching statistical significance, notable differences in collagen distribution were observed between floxed and non-floxed mice in the late Tam group. Across both the tumor margin and core, mice with a functional TGFβRII in CAFs demonstrated higher collagen expression than the floxed group. The Sirius Red positive area in the tumor margin reached approx. 60% in the control group and slightly below 50% in the floxed group. In the tumor core, the Sirius Red positive area measured around 30% in the control group, in contrast to approx. 20% in the K.O. mice. Although it cannot be definitively concluded to what degree the observed effects on tumor growth are attributable to altered collagen formation via the inactivated TGFβRII in CAFs, this mechanism likely plays a significant role, as evidenced by the observed trend of disrupted collagen formation. A larger cohort would likely have resulted in statistically significant differences in collagen deposition, which would have further strengthened the observed trend.

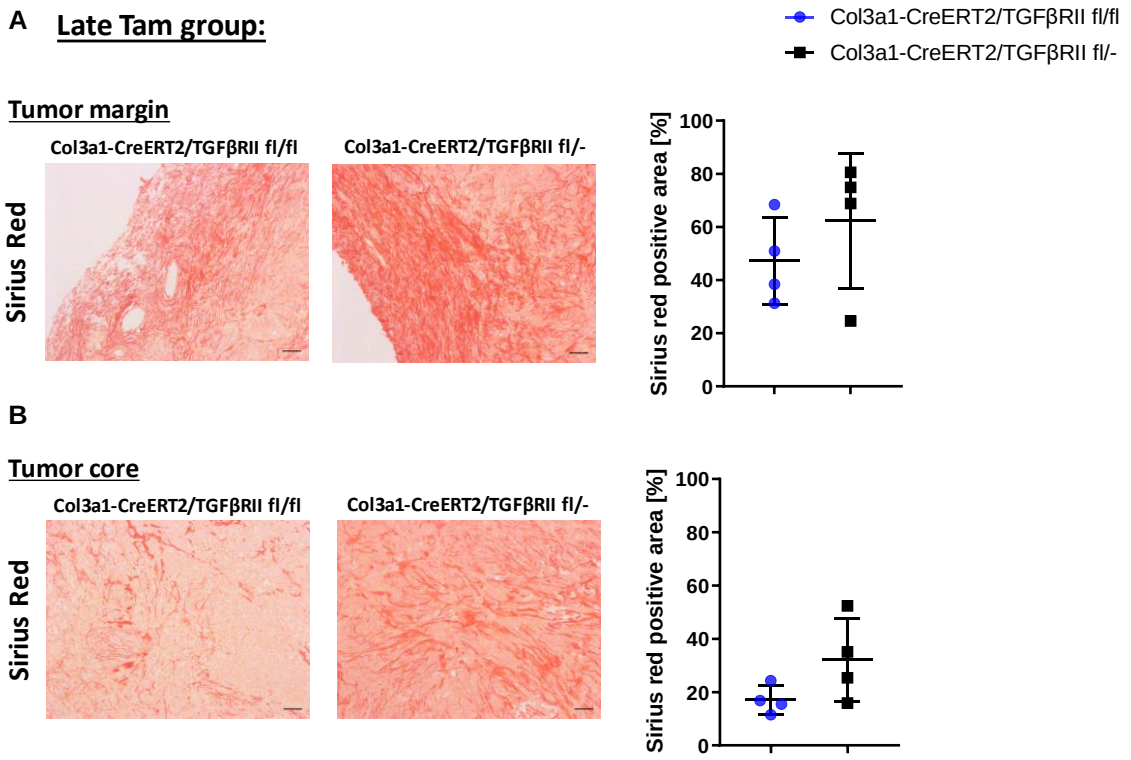

Figure 16: Histological- morphometric analysis of Sirius Red stained sections of the late Tam group. Distribution of collagen fibers stained with Sirius Red of subcutaneous (s.c.) LuCa6 tumors from Col3a1-CreERT2/TGFβRII fl/fl and Col3a1-CreERT2/TGFβRII fl/- mice is shown in (**A.**) the tumor margin and (**B.**) tumor core. Quantitative analysis of the positive stained area is presented. For each tumor, between 5-10 high power fields (20× magnification) were analyzed per region (margin and core). Results are expressed as mean values ± SD. Scale bar = 100µm. n = 4/group.

To further investigate the impact of the TGFβRII K.O. in CAFs on s.c. LuCa6 tumors, immunohistochemical staining using the α-SMA antibody (a marker for activated myofibroblasts) was carried out. In the early Tam group (Fig. 17A/B), α-SMA positive cells were evenly distributed in the tumor margin and tumor core. Surprisingly, α-SMA expression was higher in both the tumor margin and the tumor core in the floxed mice than in the control group. The tumor margin in the floxed group demonstrated a significantly higher positive area of about 7.5%, while the control animals revealed a positive α-SMA expression of about 3%. This pattern was consistently observed in the tumor core as well.

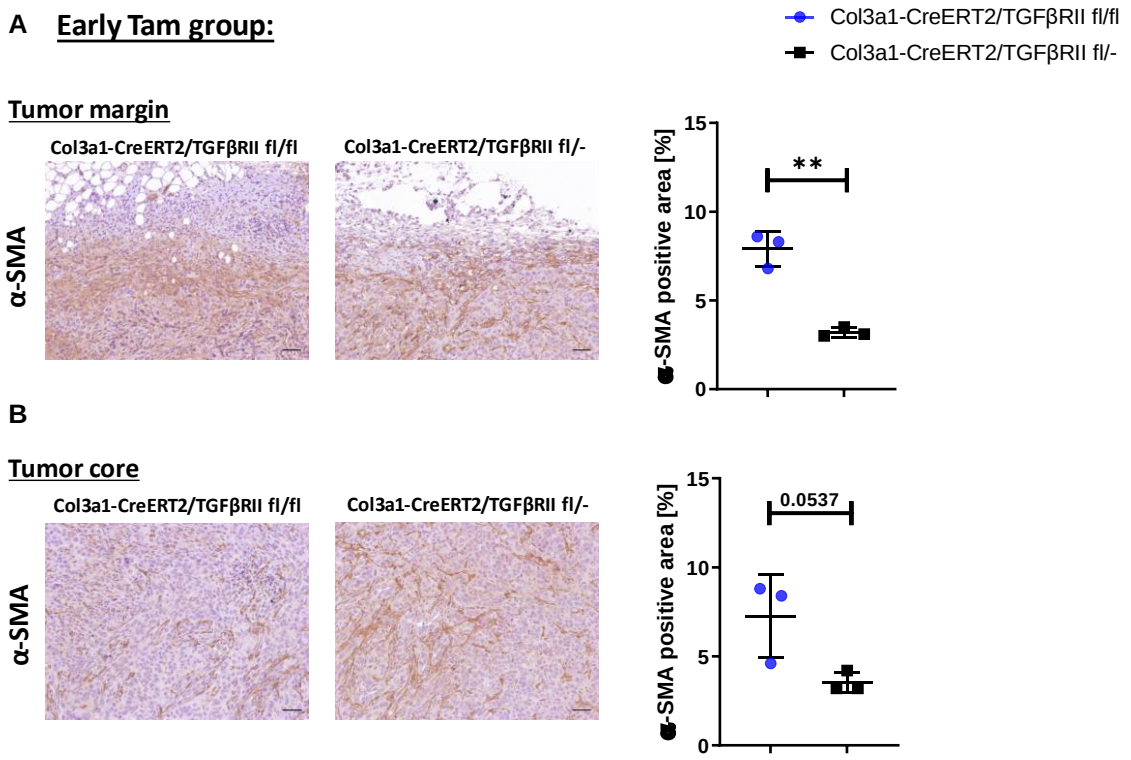

Figure 17: Immunohistochemical staining for α-SMA of the early Tam group. Representative photomicrographs and image quantification of α-SMA expression in the tumor margin (**A.**) and tumor core (**B.**) of subcutaneous (s.c.) LuCa6 tumors from Col3a1-CreERT2/TGFβRII fl/fl and Col3a1-CreERT2/TGFβRII fl/- mice are shown. For each tumor, between 5-10 high power fields (20× magnification) were analyzed per region (margin and core). Results are expressed as mean values ± SD (** p <0.01). Scale bar = 100µm. n = 3/group.

In the late Tam group (Fig. 18A/B), while not achieving statistical significance, a distinct trend contrary to the early Tam group was observed. Notably, α-SMA expression was higher in the control group compared to the tumors in the K.O. group. In contrast, the distribution of α-SMA positive cells did not differ between tumor margin and tumor core. The values of the α-SMA positive area measured around 5% in the floxed group and 8% in the control group.

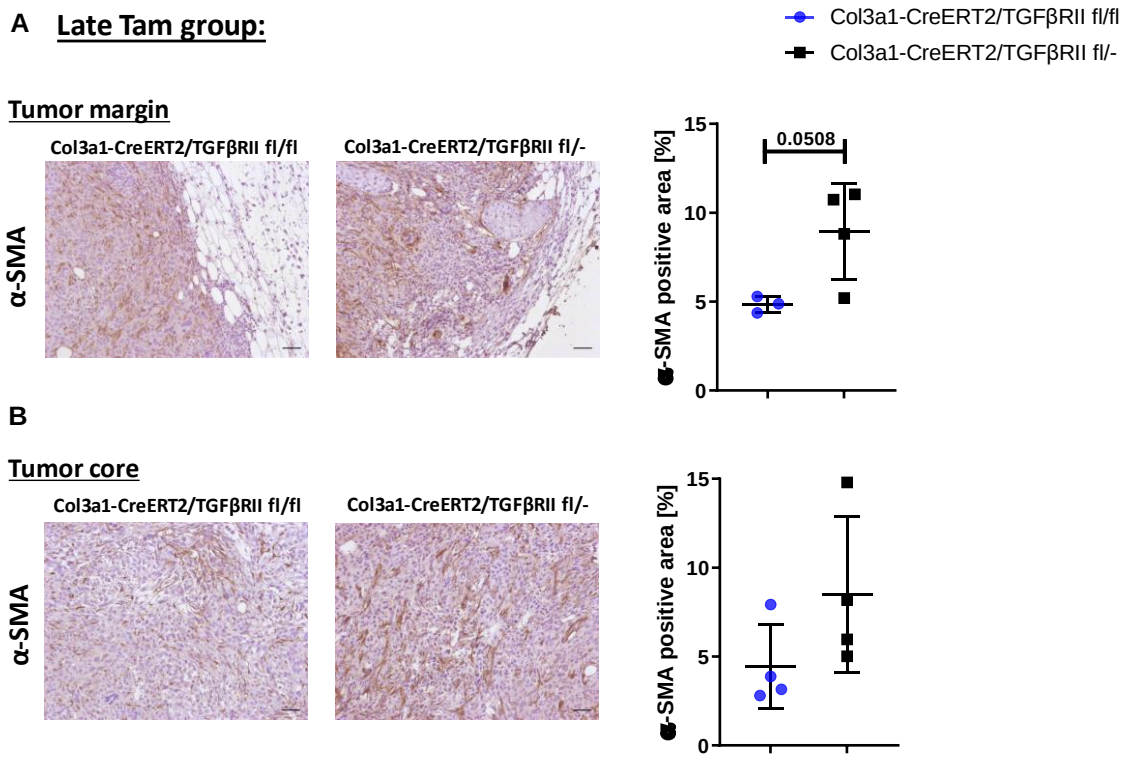

Figure 18: Immunohistochemical staining for α-SMA of the late Tam group. Representative photomicrographs and image quantification of α-SMA expression in the tumor margin (**A.**) and tumor core (**B.**) of subcutaneous (s.c.) LuCa6 tumors from Col3a1-CreERT2/TGFβRII fl/fl and Col3a1-CreERT2/TGFβRII fl/- mice are shown. For each tumor, between 5-10 high power fields (20× magnification) were analyzed per region (margin and core). Results are expressed as mean values ± SD. Scale bar = 100µm. n = 3-4/group.

3.1.2 TGFβRII K.O. in CAFs altering growth dynamics of lead and contralateral LuCa6 tumors

After obtaining preliminary insights into the TME of s.c. LuCa6 tumors encompassing aspects such as collagen distribution and α-SMA expression, the previously described experiment was repeated in a modified form with expanded cohorts (Fig. 8A). Unlike the prior analysis involving two distinct cell numbers, in this experiment, a cell number of $3x10^5$ of the LuCa6 cell line was bilaterally injected into the flanks of Col3a1-CreERT2/TGFβRII fl/fl mice. The initiation of the first Tam injection occurred on day 12 post-implantation, with subsequent administrations of 2 mg Tam via i.p. injection every 3-4 days with the intention to clear TGFβRII signaling in newly developing CAFs throughout the complete experimental time. Col3a1-CreERT2 mice with a completely intact wild type TGFβRII served as control animals. On day 29, all mice were euthanized, and the excised tumor tissue was further analyzed through histological staining, qPCR and flow cytometry.

Throughout tumor progression, minimal differences were observed between the groups and both tumor injection sides (Fig. 19B). However, at the endpoint of the experiment, more distinct differences in tumor development were present. Despite injecting the same concentration of LuCa6 cells, varying tumor sizes developed on each flank of the same mouse. Henceforth, no more distinctions between the right and left flanks were made from that point onward. Instead, tumors were classified into a lead tumor and its smaller contralateral counterpart. In Fig. 19C, the tumor volumes of the lead tumors (left), contralateral tumors (middle), and the combined tumor volumes (right) are shown. In the lower section of the figure, tumor weights at the endpoint are equally arranged. Representative samples from each group including a lead tumor (left) and its contralateral counterpart (right) are demonstrated in Fig. 19D. Thus, the inactivation of TGFβRII in CAFs resulted in a significant reduction of overall tumor volume and weight by almost 50%. With this experiment, the previous findings could be confirmed, and strong evidence was generated that deleting the TGFβRII signaling in CAFs highly significantly hinders their supportive function for tumor growth.

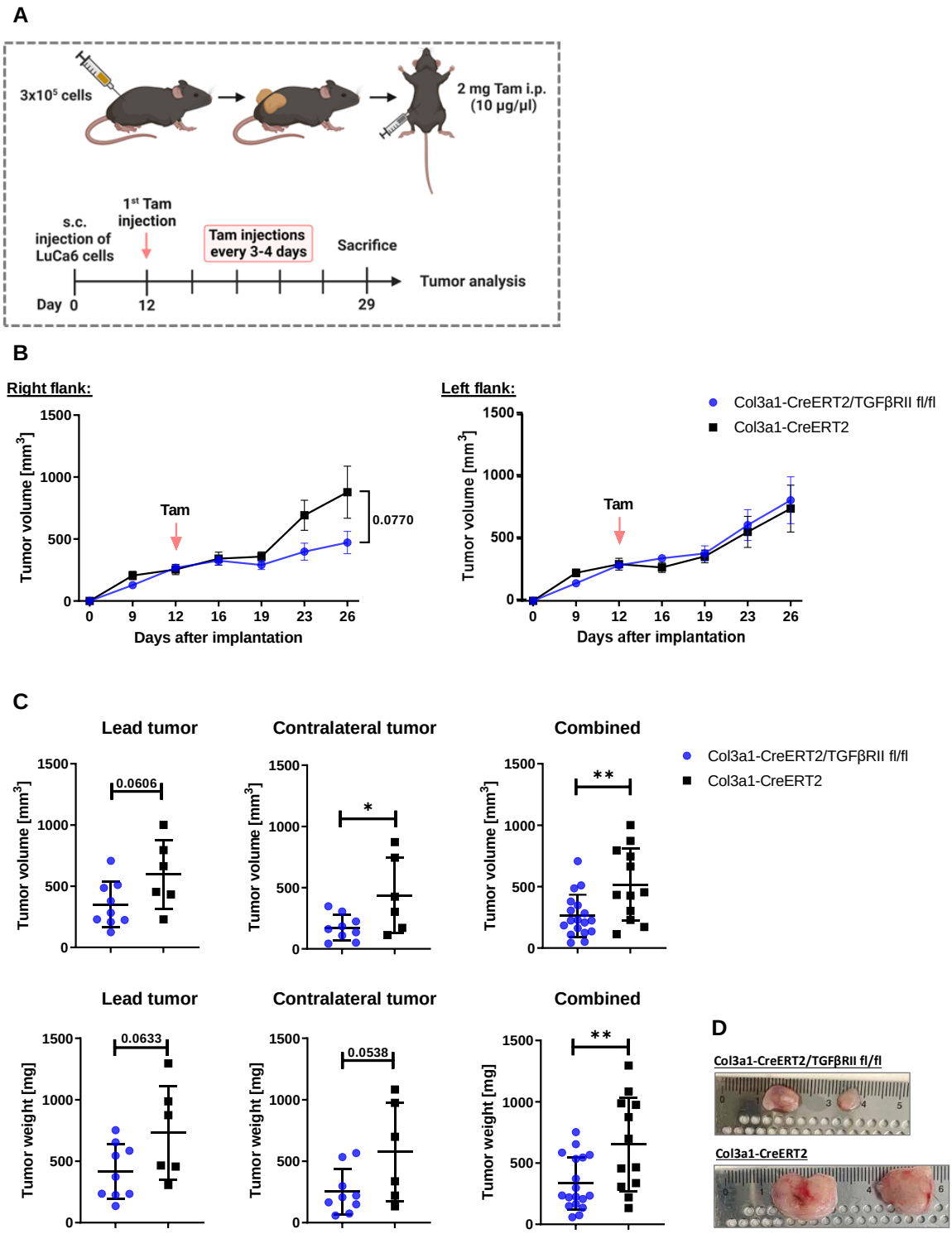

Figure 19: Impact of TGFβRII inactivation in CAFs on development of s.c. LuCa6 lung tumors. **A.** Experimental design: LuCa6 cells ($3x10^5$) were bilaterally injected into Col3a1-CreERT2/TGFβRII fl/fl and Col3a1-CreERT2 mice, with Tamoxifen (Tam) treatment (2 mg i.p.) initiated on day 12. (created with BioRender.com). **B.** Tumor progression over the study period (right flank vs. left flank) **C.** Tumor volumes and weights at the endpoint of the experiment categorized into lead and contralateral tumors based on size. **D.** Representative *ex vivo* images of s.c. LuCa6 tumors from K.O. and control group. (*p < 0.05, **p < 0.01, n = 6-9/group)

Next, Sirius Red staining was performed to investigate the potential impact of TGFβRII K.O. in CAFs on collagen deposition within the tumor margin and core of s.c. LuCa6 tumors. Both, lead tumors and the contralateral tumors were analyzed. Collagen deposition was prominent in the tumor margins compared to the tumor cores and comparable in both groups (Fig. 20A/B). The amount of collagen deposited was not reduced in the floxed group in contrast to the control mice. Thus, the knockout of TGFβRII in CAFs did not result in an attenuation of collagen synthesis.

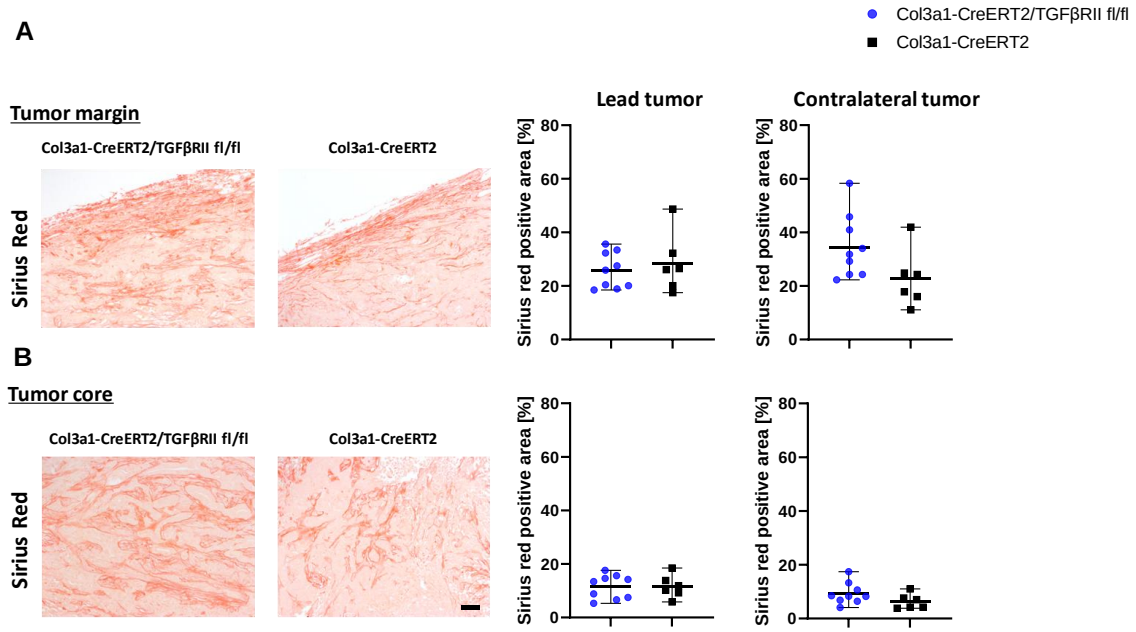

Figure 20: Histological analysis of Sirius Red stained sections of the late Tam group. Distribution of collagen fibers stained with Sirius Red in the tumor margin (**A.**) and tumor core (**B.**) of subcutaneous (s.c.) LuCa6 tumors from Col3a1-CreERT2/TGFβRII fl/fl and Col3a1-CreERT2 is shown. Quantitative analysis of the positive stained area of lead and contralateral tumors is presented. For each tumor, between 5-10 high power fields (20× magnification) were analyzed per region (margin and core). Results are expressed as mean values ± SD. Scale bar = 100µm. n = 6-9/group.

Following this, an analysis utilizing the α-SMA antibody was carried out (Fig. 21A/B). No discernible differences in α-SMA expression were observed in both groups, be it in the tumor margin or the tumor core. Therefore, the knockout of TGFβRII in CAFs had no detectable effect on the expression of α-SMA.

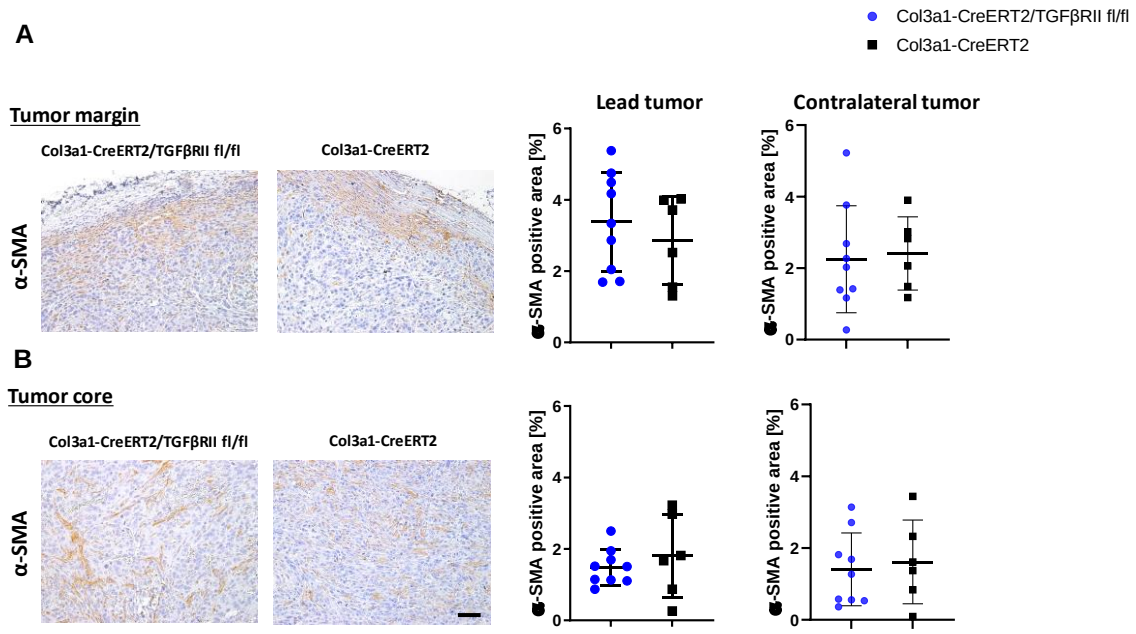

Figure 21: Immunohistochemical staining for α-SMA. Representative photomicrographs and image quantification of α-SMA expression in the tumor margin (**A.**) and tumor core (**B.**) of subcutaneous (s.c.) LuCa6 tumors from Col3a1-CreERT2/TGFβRII fl/fl and Col3a1-CreERT2 mice are shown. For each tumor, between 5-10 high power fields (20× magnification) were analyzed per region (margin and core). Results are expressed as mean values ± SD. Scale bar = 100 µm. n = 6-9/group.

Throughout the performed immunohistochemical analyses, immune cell infiltration and other specific cellular characteristics and signaling pathways in CAFs were investigated to obtain more insight into the full impact of TGFβRII K.O within the TME of desmoplastic tumors. These markers included CD68 and YM1, CD4, FoxP3 and CD8, collagen type I, vimentin and pSMAD2 for histological evaluation. CD68 staining was utilized to identify total macrophages and monocytes within the tumor tissue samples, while YM1 served as a marker for alternatively activated macrophages (M2 phenotype). CD3 staining allowed for the evaluation of overall T cell infiltration and distribution in the tumor tissue, while CD8 staining provided insights into the presence and distribution of cytotoxic T cells (CD8+ T cells). CD4 staining was used to detect helper T cells (CD4+ T cells), and FoxP3 expression was assessed to identify regulatory T cells (Tregs), which play a critical role in immune regulation. Collagen type I staining focused on interstitial collagen deposition, an essential component of connective tissues. Vimentin staining highlighted mesenchymal cells (including vascular endothelia), reflecting alterations in mainly fibroblast phenotype in comparison to α-SMA-positive contractile myofibroblasts. Lastly, pSMAD2 staining indicated activation of the TGF-β signaling pathway.

Immunohistochemical analysis of tumor tissues revealed distinct patterns between the tumor margin and core regions. CD68+ macrophages were quantified as a percentage of positive area in the tumor margin and as positive cells per field in the tumor core. In the tumor margin, the K.O. group showed a trend towards a higher CD68+ percentage compared to the control group, although this difference did not reach statistical significance. In the tumor core a similar trend was observed. YM1 staining, indicative of alternatively activated (M2) macrophages, was also assessed in both regions. In the tumor margin, the YM1+ area was slightly elevated in the floxed group compared to the control, while in the tumor core, YM1+ levels were comparable between groups (Fig. 22A).

T cell infiltration was assessed by quantifying CD4+, FoxP3+ and CD8+ cells in both the tumor margin and core regions (Fig. 22B). In the tumor margin, CD4+ T cells showed a slightly higher presence in the floxed group compared to the control group, although this difference was not statistically significant. The tumor core exhibited minimal CD4+ T cell infiltration in both groups, with values close to 0%. FoxP3+ cells were more abundant in the tumor margin, compared to tumor core in both groups, with overall low FoxP3+ cell numbers and some individual tumors with very high levels of FoxP3+ cells. Notably, FoxP3 defines both CD4+ regulatory T cells (Treg) and regulatory dendritic cells. Analysis of (cytotoxic) CD8+ T cell infiltration revealed differences between the floxed group and controls. In the tumor margin, the floxed group showed a trend towards higher CD8+ cell counts, though this was not statistically significant. The tumor core exhibited significantly higher CD8+ infiltration in the floxed group compared to controls.

The immunohistochemical panel also included collagen type I staining to assess collagen type I deposition, an important component of the TME. Collagen type I expression was comparable in the tumor margin between the floxed and control group. In the tumor core, collagen type I expression was generally lower, with the floxed group exhibiting approx. 5% positive area compared to around 8% in the control group, although this difference was not statistically significant.

A significant finding emerged from the analysis of vimentin expression, a marker for mesenchymal cells, mainly fibroblasts. In the tumor core, a statistically significant increase in vimentin positive cells was observed in the K.O. group compared to the controls (Fig. 22C). This unexpected observation suggests an enhanced presence of mesenchymal or fibroblast-like cells in the tumor core when TGF-β signaling is disrupted in Col3a1-expressing cells.

To evaluate the activity of the TGF-β signaling pathway, pSMAD2 levels were quantified (Fig. 22D). The analysis of pSMAD2 expression in the tumor margin and core revealed distinct patterns of cellular localization. In the tumor margin, the number of pSMAD2-positive cells was slightly lower in the floxed group, although not significantly. Interestingly, despite the genetic deletion of TGFβRII in Col3a1-expressing cells, pSMAD2 levels in the tumor core did not differ between both cohorts, suggesting that the loss of TGFβRII in Col3a1+ cells may not dramatically alter overall SMAD2 phosphorylation within the TME.

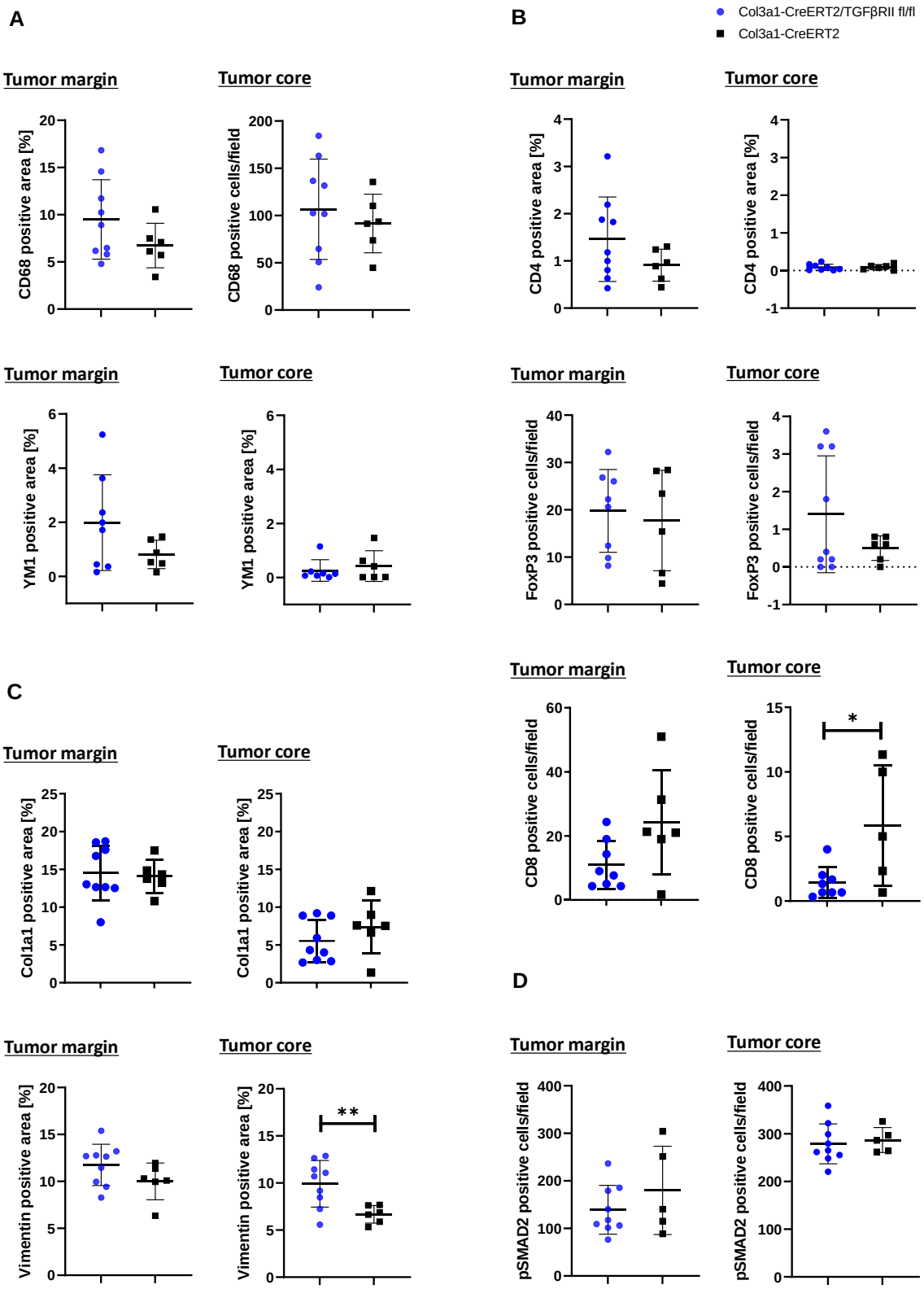

Figure 22: Quantitative analysis of immunohistochemistry markers. Plots showing the distribution of various cellular markers in tumor margin and core of Col3a1-CreERT2/TGFβRII fl/fl (blue) and Col3a1-CreERT2 (black) groups. Expression of CD68+ and YM1 (**A.**), CD4, FoxP3+ and CD8 (**B.**),

Col1a1 (collagen type I) and vimentin (**C.**), pSMAD2+ (**D.**) Each dot represents an individual sample, with mean ± SD indicated (*p < 0.05, **p < 0.01, n = 6-9/group).

In the following part, qPCR analysis was used to assess the expression of *acta2* (α-SMA) and *tgfbr2* (TGFβRII) in both the lead tumor and its contralateral counterpart (Fig. 23A/B). The transcript data revealed a significant upregulation of α-SMA and TGFβRII transcripts in Col3a1-CreERT2/TGFβRII fl/fl mice compared to the control group.

In the subsequent analysis, the examination of *col1a1* and *col3a1* expression revealed comparable transcript levels for both collagen chains in the lead tumors of both experimental groups. However, higher transcript levels were observed in the contralateral tumors of the floxed group, even significant regarding *col3a1* transcripts, indicating that the expression of these major collagen chains is independent of TGFβRII signaling in CAFs.

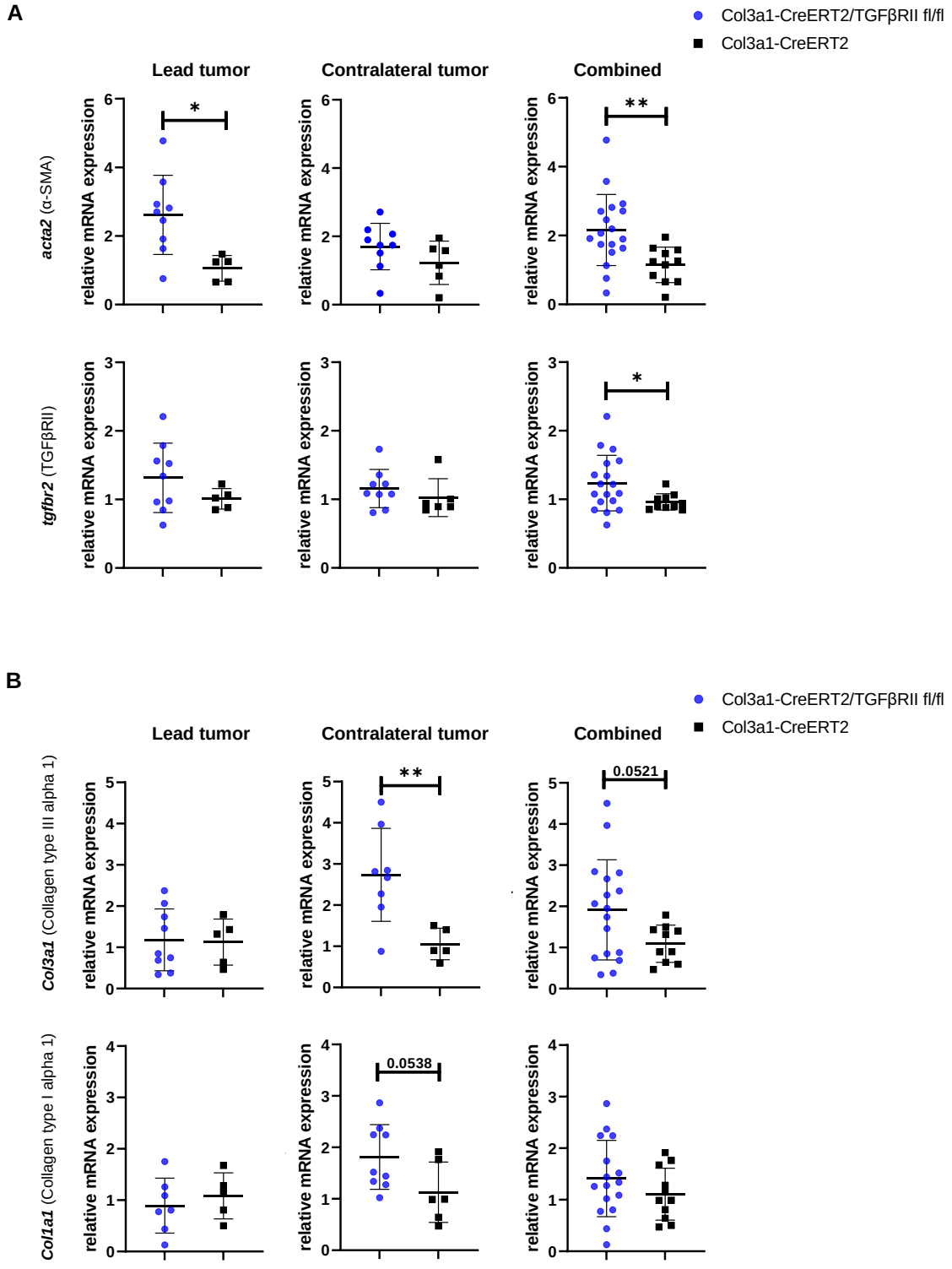

Figure 23: mRNA expression analysis of subcutaneous (s.c.) LuCa6 tumors from Col3a1-CreERT2/TGFβRII fl/fl and Col3a1-CreERT2 mice. Quantitative analysis of α-SMA and TGFβRII mRNA levels (**A.**) and of Col3a1 and Col1a1 mRNA levels (**B.**) in lead tumors, contralateral tumors, and pooled tumor samples. Results are expressed as mean values ± SD. (*p < 0.05, **p < 0.01, n = 6- 9/group)

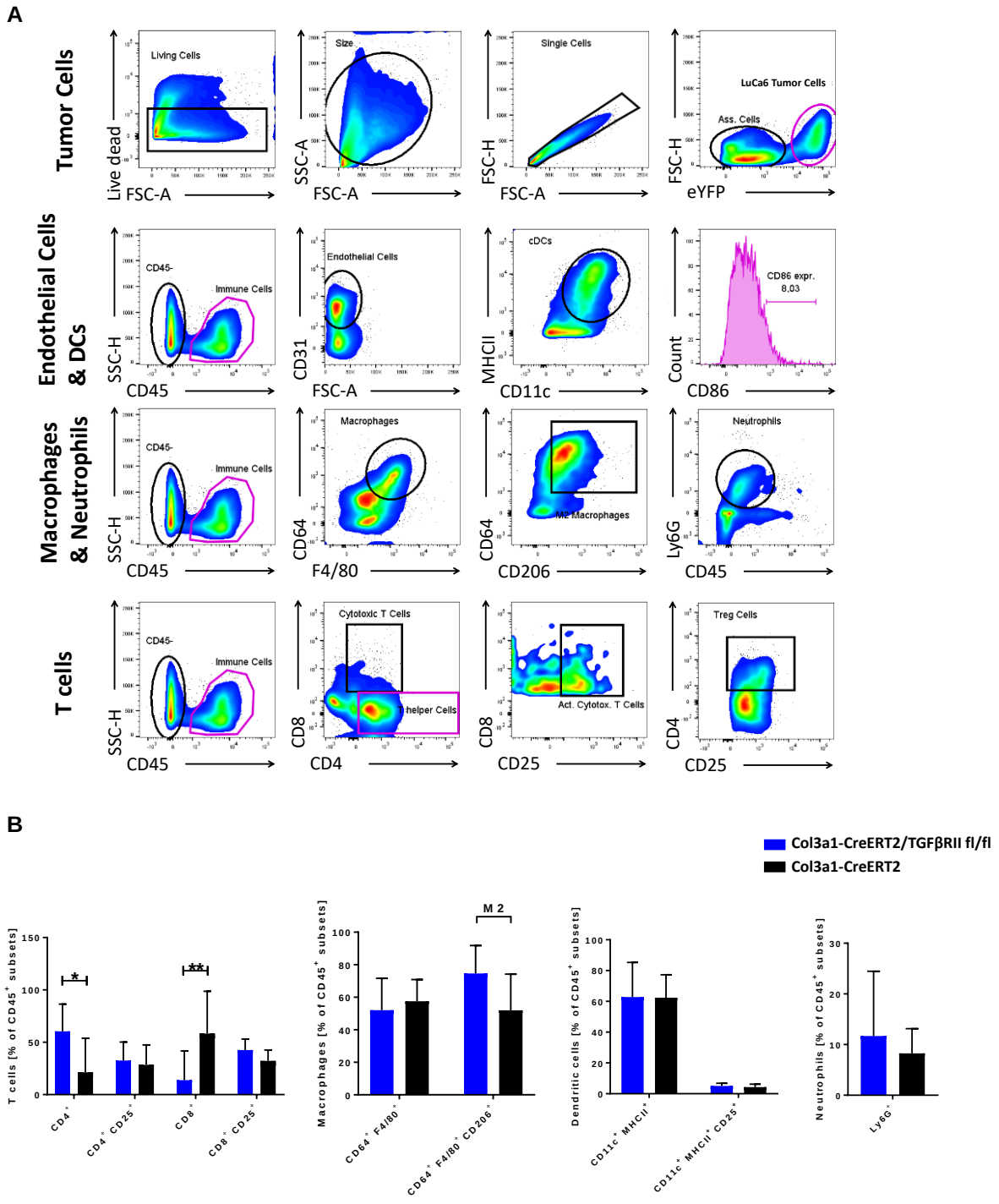

Figure 24: Flow cytometric analysis of subcutaneous (s.c.) LuCa6 tumors from Col3a1-CreERT2/TGFβRII fl/fl and Col3a1-CreERT2 mice. A. Various cell populations, including tumor cells, endothelial cells, dendritic cells (DCs), macrophages, neutrophils, and T cells, were analyzed from s.c. LuCa6 tumors. Gating strategy: living cells with SSC-H and FSC-A, single cells in FSC-H and FSC-A. **B.** Quantification of T cell subsets, macrophages, dendritic cells, and neutrophils in the tumor microenvironment, comparing Col3a1-CreERT2/TGFβRII fl/fl (blue bars) and Col3a1-CreERT2 (black bars) mice. Data are presented as mean ± SD. (*p < 0.05, **p < 0.01, n = 6-9/group)

Flow cytometric analysis of one half of the lead tumor was performed to better assess the numbers and characteristics of immune cells of interest in the TME. Relevant data are presented in Fig. 24B. The left side of the figure shows T-cell populations identified as CD45+ and either CD4 or CD8 positive. Unexpectedly, Col3a1-CreERT2/TGFβRII fl/fl mice revealed significantly lower levels of CD8+ T cells compared to controls, recognized as pivotal contributors to anti-tumor immunity. Conversely, there was an increased CD4 expression in the fibroblast TGFβRII K.O. mice, as already demonstrated by quantitative IHC. CD25, employed as a T cell activation marker) both for Treg and cytotoxic T cells, exhibited no discernible difference between the groups. Further investigation extended to other immune cell types, including M1 macrophages (CD45+CD64+F4/80+ positive) and M2-type macrophages (F4/80+CD206+). Here, no statistically significant differences in expression were detected. The total numbers of dendritic cells and neutrophils showed no differences between the two experimental groups. Overall, the flow cytometric results were in line with the immunohistochemistry and resulted in no clear observation that immune cell infiltration could play a crucial role in the tumor progression of this desmoplastic lung cancer model with TGFβRII K.O. in CAFs.

3.2 Primary hepatocellular carcinoma (HCC)

3.2.1 Treatment of immune competent mice with an orthotopic and syngeneic HCC with rapamycin, Fra-2 ASO and their combination

To assess the impact of the mTOR inhibitor rapamycin and Fra-2 targeting on the tumor growth and associated TME, an orthotopic and syngeneic liver cancer model, established by us, was used. Therefore, Dt81Hepa1-6/βgeo cells ($1x10^5$) were injected into the spleens of male C57BL/6 mice leading to a homogeneous colonization of the livers with HCC foci. At day 17 after inoculation, 5-8 mice per group received either 0.075 mg/kg of the mTOR inhibitor rapamycin as monotherapy via daily i.p. injection or Fra-2 ASO as a macrophage polarization modulator at 2 mg/kg i.p. twice a week. The third group received the combination of both rapamycin and Fra-2 ASO. Untreated HCC-bearing C57BL/6 mice served as controls (Ctrl). Five weeks post-surgery all mice were sacrificed, and the livers were further analyzed (Fig. 25A). Livers of tumor-free wild type mice were harvested and weighed to provide a valid basis for comparison with the treated mice. Fig. 25B illustrates that both the combination treatment and the individual drug administrations led to significantly decreased liver weight and a lower liver to body weight ratio which reflect tumor burden. Mice treated with the combination therapy showed approx. a 50% reduction compared to the untreated group, nearly aligning with the liver weights (1.5- 2 g) and the liver to body weight ratio of wild type mice.

Fig. 25C shows representative images of the livers from each group, highlighting the efficacy of the therapies, with frontal (left) and dorsal (right) perspectives, providing a comprehensive visualization. While livers of untreated control animals appear heavily burdened, livers of treated mice show minimal to no tumor nodules.

All applied treatments against HCC showed comparable and highly efficacious therapeutic outcomes with the combination of rapamycin and Fra-2 ASO not yielding a better result. However, this lack of synergistic effect may be challenging to detect in this experimental setting, as monotherapies already reduced tumor burden to levels approximating nil tumor burden in healthy hepatic tissue.

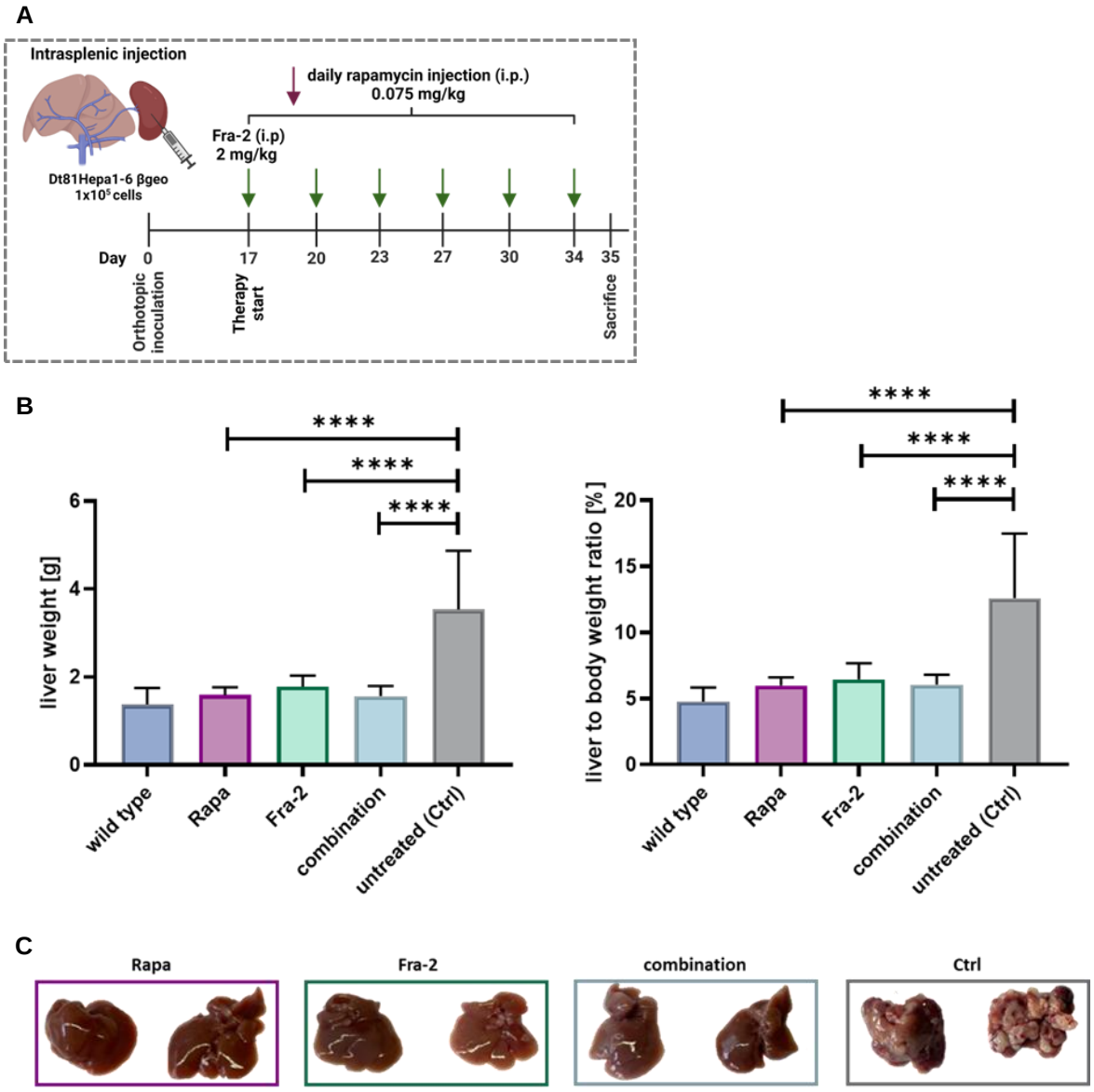

Figure 25: Therapeutic intervention of orthotopic murine HCC A. Experimental design showing intrasplenic injection of 1x10^5 Dt81Hepa1-6/βgeo cells in C57BL/6 mice, followed by daily rapamycin injections, Fra-2 ASO treatments twice a week, their combination, or no treatment from day 18-35 days (created with BioRender.com). **B.** Quantification of liver weight (left) and liver to body weight ratio (right) of all cohorts compared to tumor-free wild type mice. Data are presented as means ± SD. **** indicates $p < 0.0001$. n = 5-8/group. **C.** Representative images of livers of each treated group and Ctrl showing ventral (left) and dorsal (right) surfaces.

To confirm the previous results with a more sensitive method, the MU-Gal (4-Methylumbelliferyl-β-D-galactopyranoside) assay was employed as an alternative method to determine tumor burden in this study. This technique utilizes the specific characteristics of the Dt81Hepa1-6/βgeo HCC cell line (generated by Dominik Siegl, TIM) that expresses β-galactosidase. The activity of this enzyme directly correlates with cancer cell numbers and

therefore, with the tumor burden in liver tissue samples. This approach provided a precise and objective measurement of cancer progression in the experimental model, offering insights into HCC development and treatment efficacy.

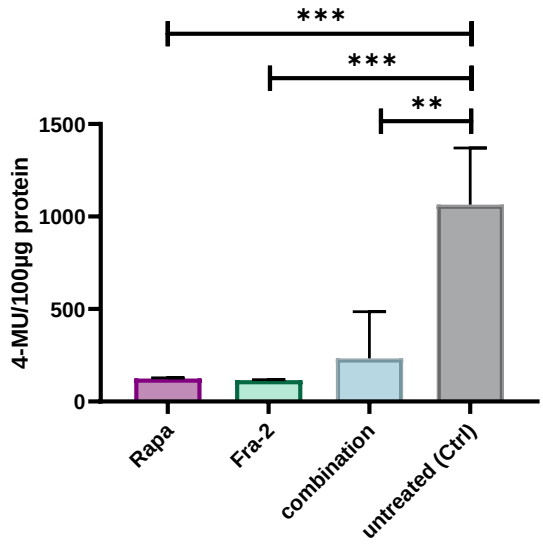

Figure 26: Evaluation of tumor burden via MU-Gal assay. β-galactosidase activity was assessed as an indicator of tumor load in liver tissue samples from HCC-bearing mice treated with Rapa, Fra-2 ASO or combination therapy compared to the untreated Ctrl group. Results are expressed as mean ± SD (**p < 0.01, ***p < 0.001, n = 4/group).

As shown in Fig. 26, the MU-Gal assay revealed comparable results to the previous assessment of the tumor burden with highly significant differences in β-galactosidase activity of treated mice compared to the untreated group. The untreated control group showed dramatically elevated levels, with activity exceeding 1000 4-MU/100µg protein, suggesting vast tumor progression. In contrast, all treatment modalities – Rapa, Fra-2 ASO and their combination – demonstrated a highly significantly reduced β-galactosidase activity. The Fra-2 ASO group showed the lowest levels, closely followed by rapamycin, both hovering around 100 4-MU/100µg protein. The combination therapy, while still highly effective, displays a slightly higher activity than the monotherapies and a higher deviation. The marked variability in the untreated group, indicated by the large error bars, highlights the diverse and heterogeneous nature of untreated HCC, and perhaps some antagonistic effect among the two therapies. While all treatments appear promising, their comparable efficacy across different groups invites intriguing questions about their mechanisms of action and potential clinical applications. These questions will be explored in forthcoming analysis.

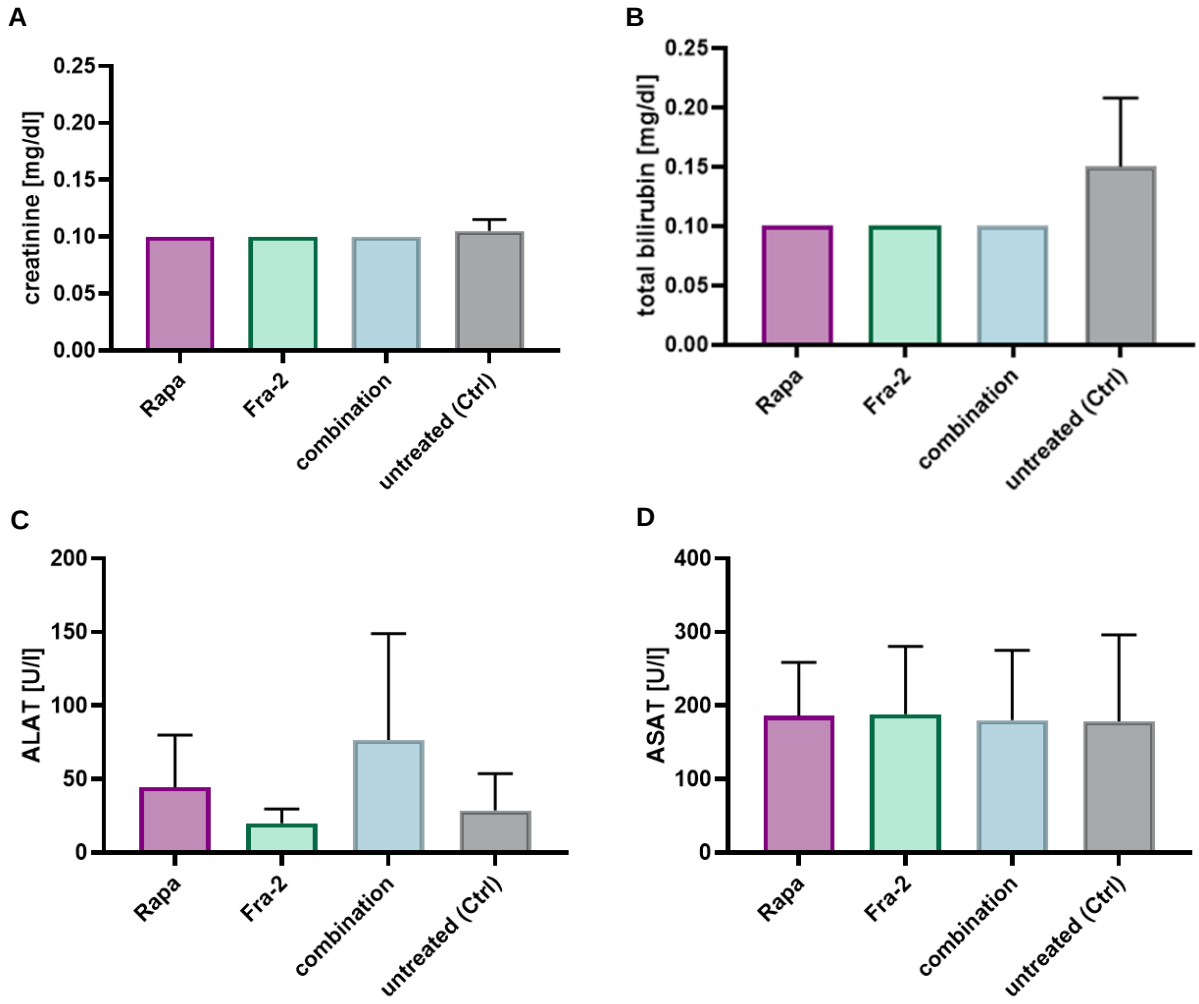

Figure 27: Serum toxicity marker analysis to evaluate drug safety in HCC-bearing mice under treatment. Levels of (**A.**) creatinine, (**B.**) total bilirubin, (**C.**) ALAT and (**D.**) ASAT were measured in serum samples from mice treated with Rapa, Fra-2, combination therapy, or untreated (Ctrl). Data are presented as mean ± SD (n = 4-6/group).

First, the safety profile of the experimental treatments for HCC was assessed through the analysis of key serum toxicity markers in the mice at sacrifice. Figure 27 presents the quantification of four critical serological indicators: creatinine, total bilirubin, alanine aminotransferase (ALAT) and aspartate aminotransferase (ASAT) analyzed by the central laboratory of the University Medical Center Mainz. These markers provide insights into potential hepato- and nephrotoxicity and overall physiological stress induced by the treatments.

Creatinine, an indicator of renal function, showed minimal variation across all treatment groups (Fig. 27A), with levels slightly below the standard reference range of 0.1–0.36 mg/dl for mice. The mean creatinine levels were consistent around 0.10 mg/dl, with the untreated Ctrl group exhibiting a mean of approximately 0.11 mg/dl. The narrow range of creatinine values suggests that none of the treatments induced significant kidney damage.

Total bilirubin, a marker of liver function and potential hepatocellular damage, displayed also levels slightly below the standard mice reference range (0.2–1.2 mg/dl). The untreated Ctrl group showed a slightly higher mean value of around 0.15 mg/dl, but with a significantly larger standard deviation (Fig. 27B). Normal bilirubin levels in the bloodstream are a key indicator of liver health and proper red blood cell metabolism. This balance reflects a harmonious interplay between the body's own production of bilirubin from the breakdown of ageing red blood cells and the liver's ability to remove it from the system.
Next, ALAT, an enzyme specific to liver cells, which serves as a sensitive indicator of hepatocellular damage was analyzed (Fig. 27C). The combination therapy cohort stands out with the highest mean ALAT level of approximately 80 U/l, which is accompanied by a substantial standard deviation that underscores some variability within this group. The remaining experimental groups exhibit ALAT levels clustering around or below 50 U/l, a range that largely aligns with the reference threshold of <35 U/l. ASAT, another enzyme indicative of liver health but also found in other tissues, showed uniform levels across all groups (Fig. 27D). Mean ASAT values cluster around 180-200 U/l for all treatments and the untreated Ctrl group, still within the reference range of 50-200 U/l, suggesting no significant treatment-specific effect. In conclusion, the serum toxicity marker analysis indicates that the experimental treatments demonstrate a favorable safety profile in HCC-bearing mice. The treatments do not appear to induce significant hepatotoxicity or renal stress. However, the variability observed, particularly in ALAT and ASAT levels, underscores the importance of continued monitoring and further studies to fully elucidate the long-term safety and specific mechanisms of these treatments.

In the following sections, various analyses, including quantitative Sirius Red staining and IHC and multiple qPCRs were performed to further explore the TME of HCC diseased liver tissues.

To visualize the effects of different HCC-treatments on collagen deposition, Sirius Red staining was utilized (Fig. 28A/B). The untreated control group exhibited the highest level of collagen deposition, with a Sirius Red-positive area of approx. 5%. In contrast, all treatment groups showed markedly reduced collagen deposition. Notably, the combination treatment of Rapa and Fra-2 ASO resulted in the lowest collagen deposition within the livers. Statistical analysis revealed significant differences between the untreated control group and both the Rapa monotherapy group and the combination group, offering the most pronounced anti-fibrotic effect.

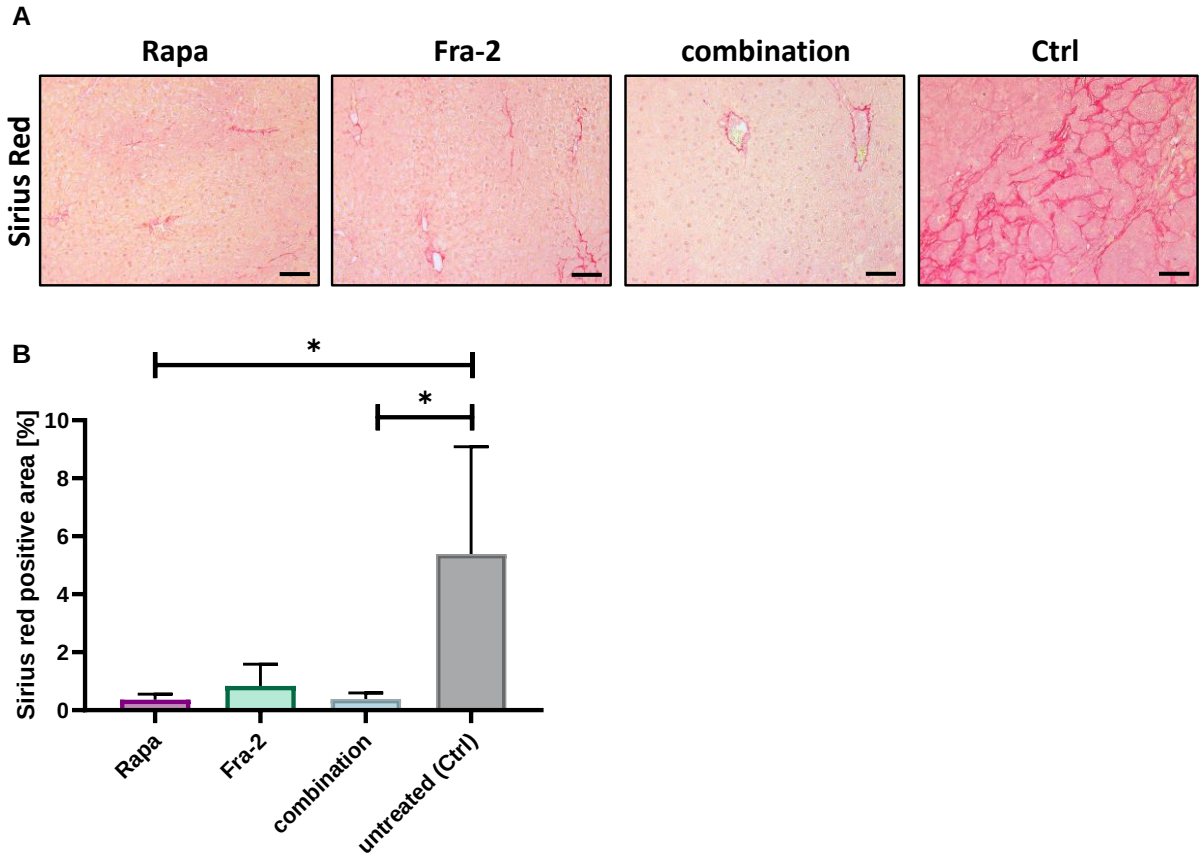

Figure 28: Histological analysis of Sirius Red stained liver sections of HCC-bearing mice. A. Representative images of Sirius Red staining in liver sections from mice treated with Rapa, Fra-2 ASO, combination therapy and untreated (Ctrl). **B.** Quantification of collagen deposition by determination of Sirius Red positive area. Values are presented as mean ± SD. (*$p < 0.05$, n = 4/group). Scale bar = 100 µm.

Next, hematoxylin and eosin (H&E) staining was performed to provide detailed visualization of the morphological features of this HCC in mouse livers. In Fig. 29 the liver of an untreated HCC-bearing mouse is shown with both cancerous and normal tissue. Panel A shows a 5x merged view of the liver, clearly delineating the tumor mass (outlined by a dashed line) within the surrounding normal hepatic parenchyma. The tumor appears as a distinct, more densely stained region. Panel B provides a 20x magnification of one tumor area, allowing for a closer examination of the tumor-normal tissue interface and the altered cellular architecture within the neoplastic region. Panel C further zooms in to a 40x magnification of an intratumoral section, revealing the cellular details of HCC.

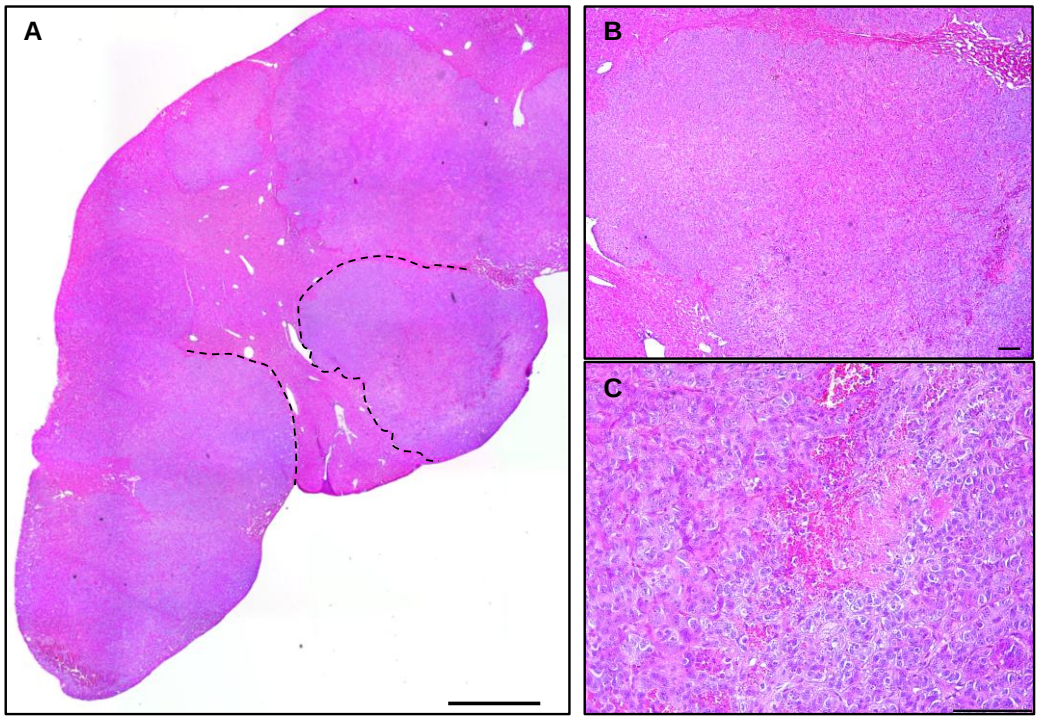

Figure 29: Histopathology of HCC in untreated mouse liver. Representative H&E-stained sections demonstrate HCC pathology. **A.** 5x merged view: Tumor mass (dashed outline) amid normal liver tissue. **B.** 20x magnification of tumor region. **C.** 40x intratumoral view showing characteristic HCC features. Scale bars: 1 mm (A), 200 µm (B), 100 µm (C).

A closer examination of the zoomed-in image reveals the typical features of HCC. The normal liver architecture is disrupted and replaced by a disorganized growth pattern, manifested in irregular trabecular or sheet-like arrangements of tumor cells. The nuclei show marked cellular atypia, evident in an increased nucleus to cytoplasm ratio, increased staining (hyperchromasia), and variability in shape (pleomorphism). The increased cellular density compared to normal liver tissue indicates the enhanced proliferation rate which is typical for cancerous tissue. The cytoplasm of the tumor cells appears eosinophilic (pink), which is characteristic of hepatocytes but often more pronounced in HCC. Notably, bright pink areas in the center of the image likely represent inflammatory cell infiltrates or possibly necrotic areas with red blood cell extravasation. The absence of normal portal tracts and the heterogeneity in staining intensity and cellular morphology across the field further underscore the cancerous nature of the tissue.

Immunohistochemical analysis of macrophage markers in liver tissues from HCC-bearing mice revealed different effects of the treatments on CD68+ and YM1+ cell populations (Fig. 30A/B).

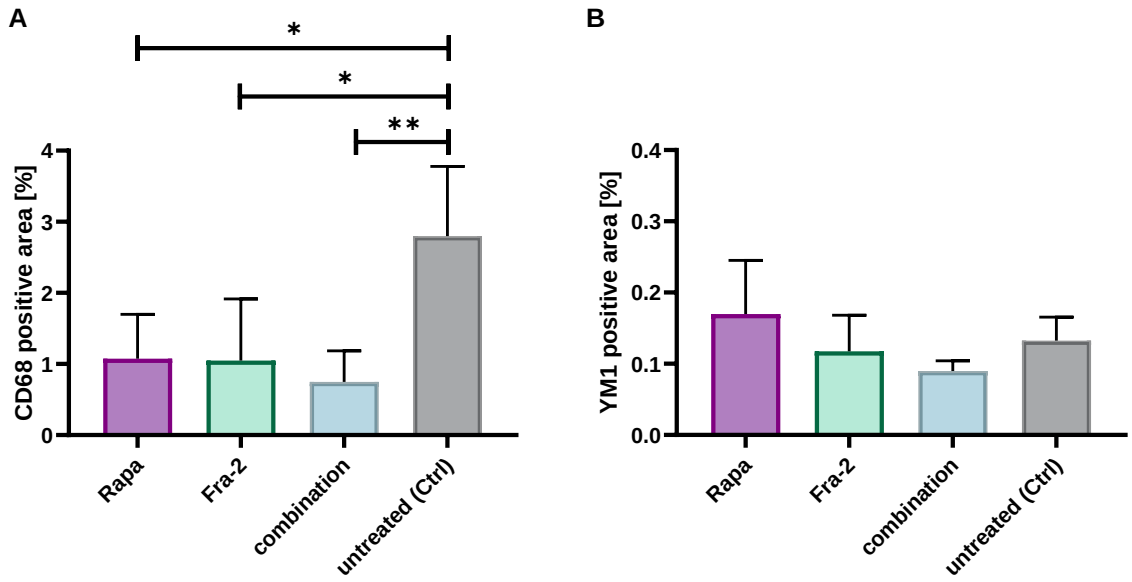

Figure 30: Quantitative analysis of macrophage marker CD68 and M2 polarization marker YM1. Expression of CD68+(**A.**) and YM1+ area (**B.**) per field in liver tissues of HCC-bearing mice treated with Rapa, Fra-2 ASO, combination therapy and untreated (Ctrl). Data are presented as mean ± SD (*p < 0.05, **p < 0.01, n = 4/group).

CD68+ cell quantification showed a significant reduction in the positive area in all treatment groups compared to the untreated control. The combination therapy demonstrated the strongest impact, followed by Fra-2 ASO and rapamycin monotherapies, all significantly lower than the untreated control (approx. 3.5%). There were no statistically significant differences among the treatment groups (below 1.5%). Interestingly, the rapamycin-treated group showed an unexpected increase in YM1 levels (considered a marker M2-type macrophages) relative to the untreated control, contrary to the initial hypothesis. Conversely, both the Fra-2 ASO monotherapy and the combination treatment resulted in a reduction of YM1 expression, although these decreases did not reach statistical significance. These results suggest that while the treatments, particularly the combination therapy, effectively reduced the presence of CD68+ macrophages in the TME, they did not significantly alter the population of YM1+ cells, which are typically associated with an M2-like phenotype.

Having examined the effects of treatments on macrophage populations, the impact on adaptive immune responses was subsequently investigated by analyzing various T cell subsets and cytotoxic activity markers. Specifically, CD4+ helper T cells, FoxP3+ regulatory cells, CD8+ cytotoxic T cells, and Granzyme B-expressing (mainly CD8+) cells were assessed, with the

latter serving as a key indicator of cytolytic potential in both innate and adaptive immune cells (Fig. 31).

First, CD4+ T cell infiltration showed a trend toward reduction across all treatment groups relative to the untreated controls. Notably, the rapamycin and Fra-2 ASO groups exhibited the lowest CD4+ T cell counts, while the combination therapy group demonstrated an intermediate effect. However, it is important to note that these differences were not statistically significant.

Next, FoxP3+ regulatory cells (mainly Tregs, but likely also suppressive DCs) were markedly reduced in all treatment groups compared to the untreated controls. Interestingly, FoxP3+ cells were almost absent in the rapamycin, Fra-2 ASO, and combination therapy groups. Nevertheless, the lack of statistical significance was attributed to high variability in the control group. Furthermore, the histological analysis of CD8+ cells (cytotoxic T lymphocytes) showed significant differences across treatments. The Ctrl group had the highest percentage of CD8 positive cells, significantly exceeding both Rapa and combination treatments. Additionally, Fra- 2 ASO treatment showed intermediate levels, higher than Rapa and the combination, but lower numbers than the untreated control, without reaching statistical significance. Lastly, Granzyme B+ cell counts, which indicate cytotoxic activity, tended to decrease in the combination therapy group compared to the untreated controls. Moreover, the rapamycin and Fra-2 ASO groups displayed levels similar to those of the control group, without reaching statistical significance. Taken together, these findings suggest a complex immunomodulatory effect of the treatments on various T cell populations. The observed trends in CD4+ T cells, Tregs, CD8+ T cells, and Granzyme B+ cells indicate potential shifts in the immune environment, with each treatment showing distinct patterns of influence.

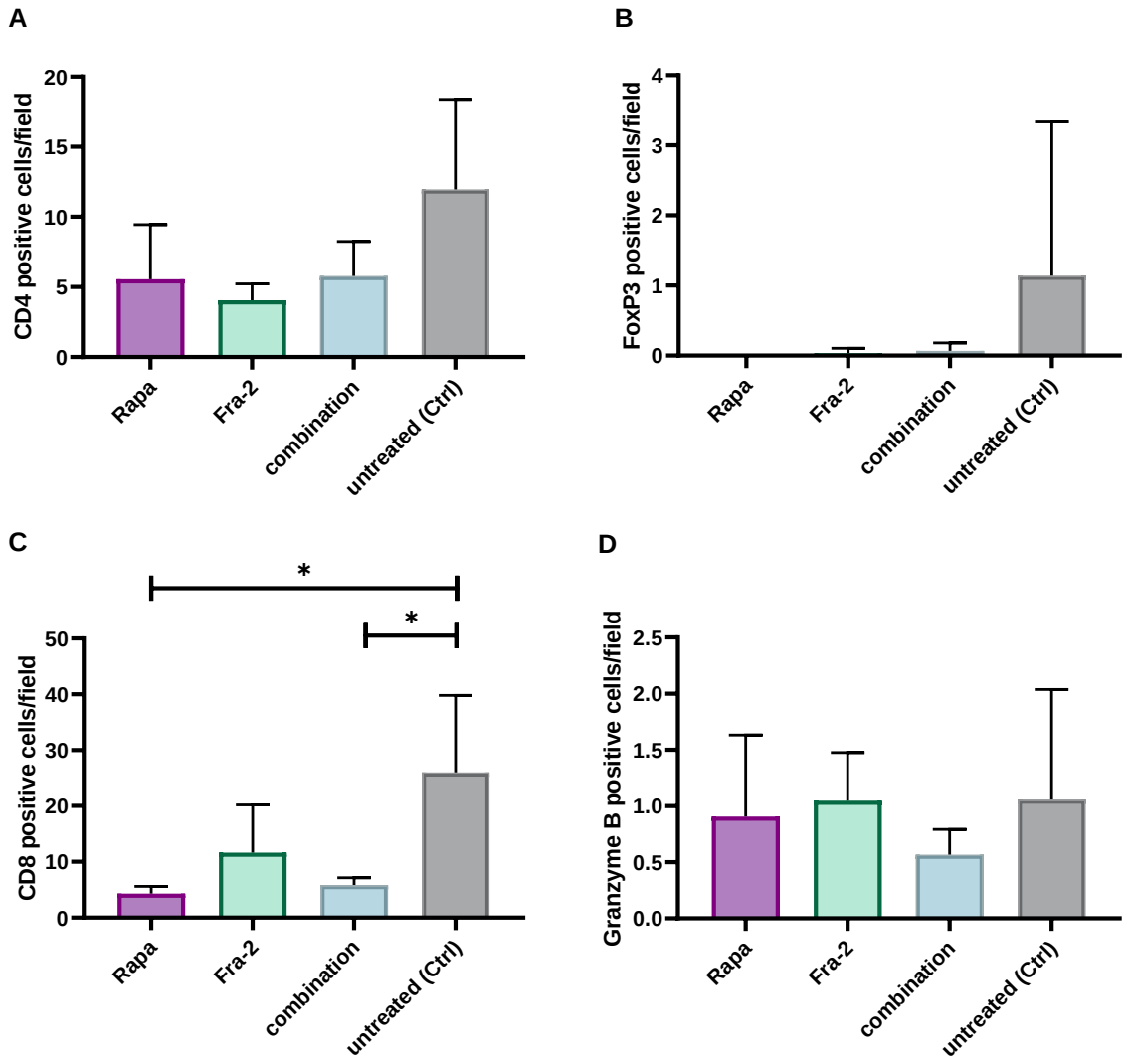

Figure 31: Quantitative analysis of T cell subsets and cytotoxic markers. Expression of CD4+(**A.**), FoxP3+ (**B.**), CD8+ (**C.**) and Granzyme B+ cells (**D.**) per field in liver tissues of HCC-bearing mice treated with Rapa, Fra-2 ASO, combination therapy and untreated (Ctrl). Data are presented as mean ± SD (*$p < 0.05$, n = 4/group).

The qPCR analysis revealed a complex modulation of macrophage phenotypes in the TME of HCC-bearing mice treated with rapamycin, Fra-2 ASO and their combination (Fig. 32). Contrary to expectations of a shift towards an anti-tumoral M1-like phenotype, a mixed response across various macrophage markers was observed, suggesting a more multifaceted impact of these treatments on the immune landscape within the tumor.

Analysis of iNOS expression, typically associated with classically activated (M1) macrophages and pro-inflammatory responses, revealed an unexpected pattern. The untreated control group exhibited the highest iNOS mRNA levels, while the combination therapy group displayed a significant reduction compared to the Ctrl. The Rapa and combination treatment groups showed intermediate levels of iNOS expression, not significantly different compared to

untreated group. CD38 is a prominent marker of plasma cells, but also a marker for classically activated M1 macrophages. Its expression followed a different pattern than previously observed for iNOS. While a shift towards the M1 phenotype was evident in the treated groups—reaching statistical significance in the rapamycin-treated group compared to the untreated animals—no synergistic effect was observed in the combination therapy (Fig. 32A). Analysis of Fra-2 expression revealed an unexpected outcome across treatment groups (Fig. 32B). Rapamycin monotherapy led to a significant increase in Fra-2 levels compared to the untreated control. Surprisingly, the Fra-2 ASO treatment did not yield the anticipated downregulation, showing Fra-2 expression levels between those of the rapamycin and the control group. The combination therapy resulted in Fra-2 levels lower than with the Fra-2 ASO alone, but still higher than the untreated control. These results suggest a complex regulation of Fra- 2 expression, possibly different in the cancer cells from the cells of the TMA (which are prominently addressed by the ASO), in response to these treatments, with rapamycin unexpectedly upregulating Fra-2, while the targeted Fra-2 ASO did not lead to the most substantial reduction in Fra-2 levels as initially hypothesized.

As previously observed in the IHC staining, YM1 showed a similar pattern at the mRNA level. In Fig. 32C elevated YM1 expression in the Rapa group compared to the untreated control is shown, while the Fra-2 ASO and the combination group show lower expression levels, although these differences did not reach statistical significance. Besides, CD206, which is also an M2 macrophage marker, showed varying expression levels across treatments. While the treated groups showed expression patterns similar to YM1, an unexpected statistically significant downregulation was observed in the untreated Ctrl compared to the rapamycin-treated mice. Lastly, IL-10, an anti-inflammatory cytokine that primarily polarizes macrophages towards an M2 phenotype was analyzed via qPCR (Fig. 32C). The results were consistent with those of CD206, with significantly higher expression of IL-10 in the Rapa group, as well as in the Fra-2 ASO group. These findings reinforce the importance of considering multiple markers when assessing macrophage polarization *in vivo*, as the treatments appear to induce a mixed phenotype rather than a clear shift towards either M1 or M2 states. This mixed responses in view of high anti-tumor efficacy have implications for the overall anti-tumor efficacy of these and other tumor as well as TME-targeted treatments.

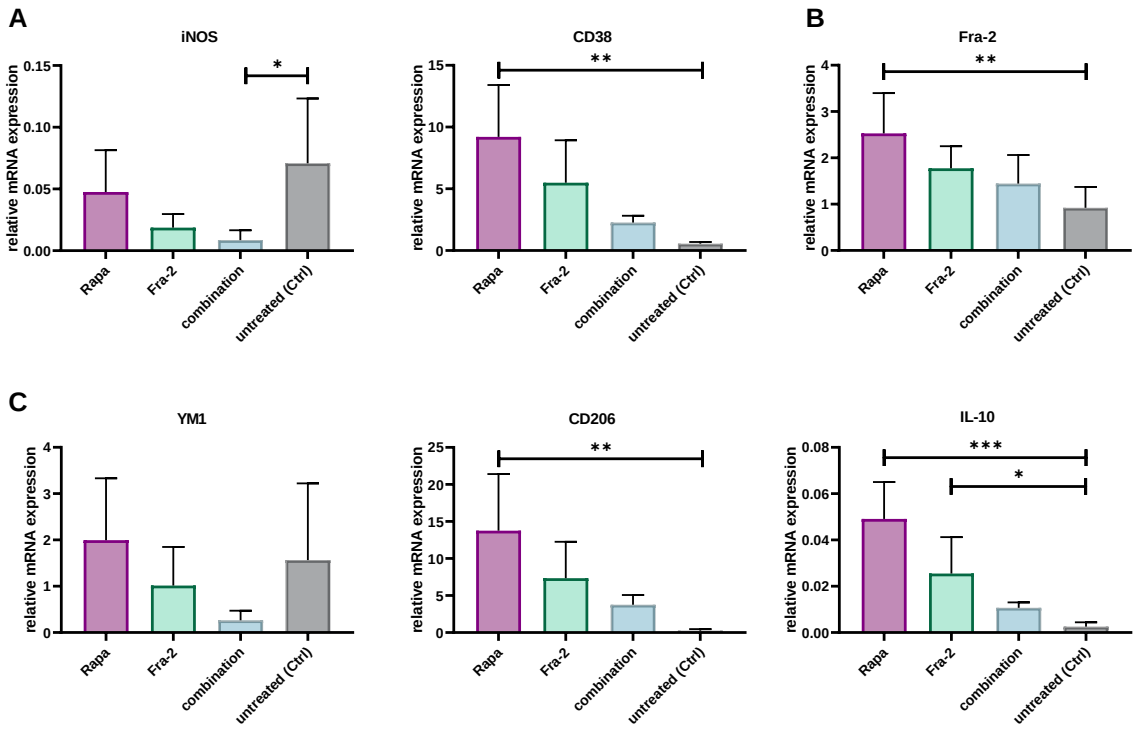

Figure 32: Relative mRNA expression in liver tissues of HCC-bearing mice. Quantitative analysis of M1-associated macrophage markers iNOS and CD38(**A.**), transcription factor Fra-2 (**B.**) and M2-associated macrophage markers YM1, CD206, and IL-10 (**C.**) of mice treated with Rapa, Fra-2, combination therapy and untreated (Ctrl). Data are presented as mean ± SD (*p < 0.05, **p < 0.01, ***p < 0.001, n = 4/group)

After Sirius Red staining had already shown a significant anti-fibrotic effect of the therapies, mRNA expression levels of the major interstitial *col1a1* and *col3a1* were additionally determined by qPCR (Fig. 33A/B). For *col1a1*, a significant difference was observed between the untreated control group vs the treated groups. The untreated control exhibited highly significantly higher transcript levels, approximately nine-fold greater than the other groups. Regarding *col3a1*, a comparable pattern emerged, though less pronounced. The untreated control group again displayed the highest expression, although not yet statistically significant. The treatment groups all showed reduced expression compared to the controls, with Fra-2 ASO and the combination treatment resulting in particularly low levels, providing further support for the anti-fibrotic effects.

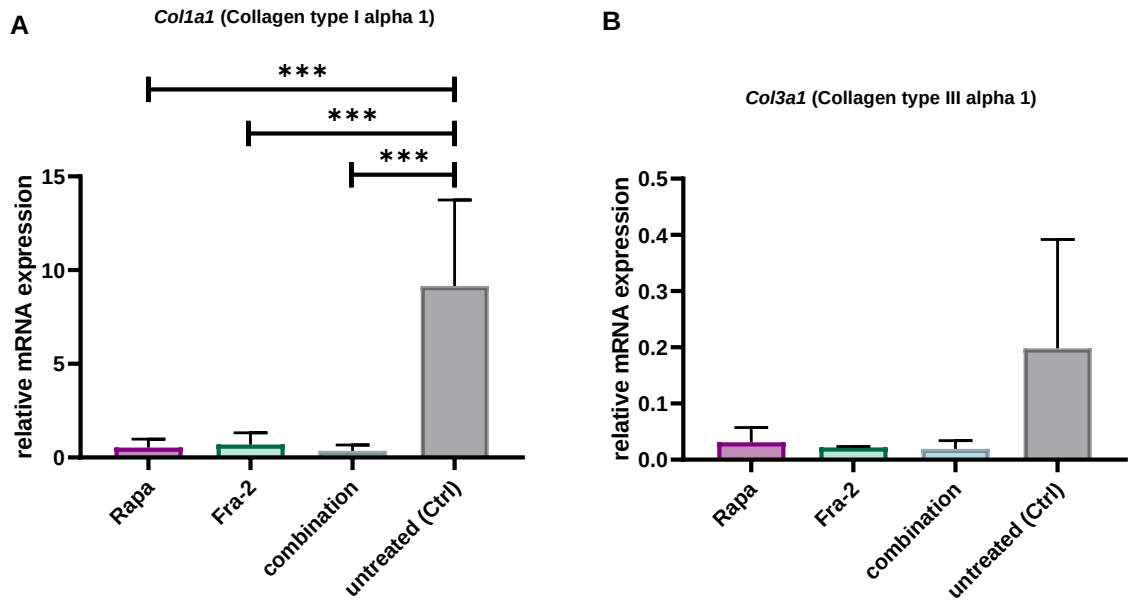

Figure 33: Relative mRNA expression of Col1a1 and Col3a1. Quantitative analysis of Col1a1 (**A.**) and Col3a1 (**B.**) mRNA levels of livers from HCC-bearing mice treated with Rapa, Fra-2 ASO, combination therapy and untreated (Ctrl). Results are expressed as mean values ± SD. (***p < 0.001, n = 4/group)

3.2.2 Establishing an additional subcutaneous and orthotopic HCC model

Establishing reliable cancer models is crucial for preclinical research focused on evaluating potential therapeutic interventions. In addition to the orthotopic HCC model described before, the RIL-175 cell line was used to establish both s.c. and orthotopic model, highlighting the significance of testing therapies across diverse model systems.

Due to the inability of Dt81Hepa1-6/βgeo cells to grow subcutaneously (data not shown), an alternative model for rapid therapy screening was required. Experiments with the RIL-175 cell line were carried out at four different concentrations: $0.25x10^6$, $0.5x10^6$, $0.75x10^6$ and $1x10^6$ cells, with 5 mice per group (Fig. 34A). Tumor progression was assessed following s.c. injection of these cells into the right flank of female C57BL/6 mice, revealing concentration-dependent growth characteristics.

To investigate tumorigenesis in an orthotopic model, $0.5x10^6$ RIL-175 cells were injected intrasplenically injected into male C57BL/6 mice (Fig. 34B). According to the original experimental design, sequential euthanasia of cohorts (n = 5 per timepoint) was planned at 2-, 3-, and 4-weeks post-injection to evaluate tumor progression over time. However, as a result of the rapid tumor growth and the consequential adverse health effects observed in the mice within two weeks post-injection, all animals had to be euthanized.

Liver weight and liver to body weight ratio were significantly higher in HCC-bearing mice compared to wild type mice, demonstrating the suitability of the RIL-175 cell line as an orthotopic HCC model. However, to optimize experimental conditions, a lower cell count should be considered.

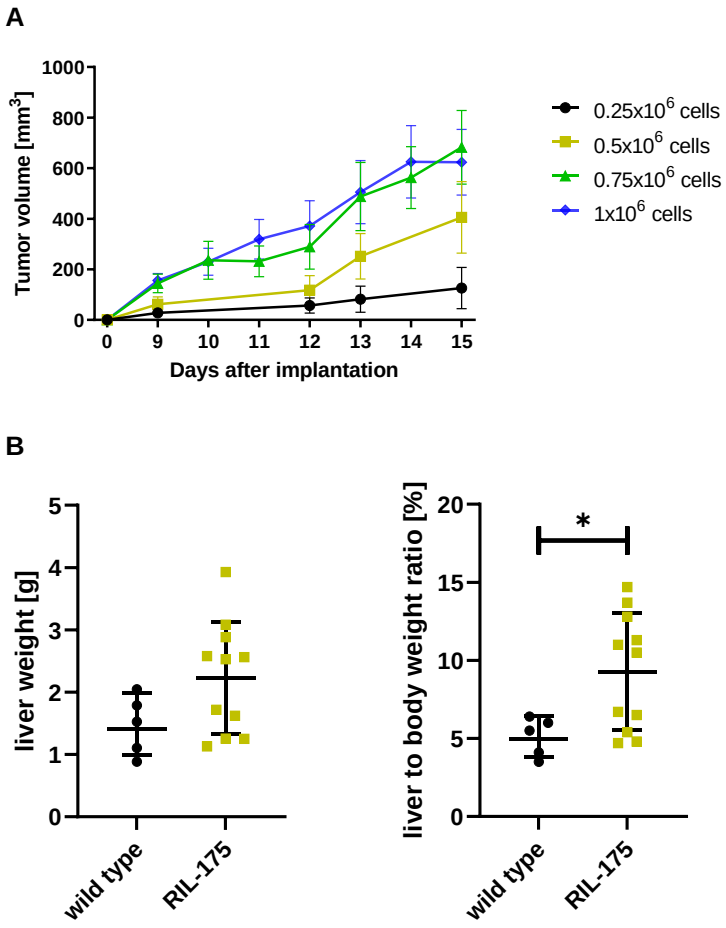

Figure 34: Tumor progression dynamics of the RIL-175 cell line. A. Tumor growth kinetics following implantation of varying cell numbers of RIL-175 cell line. Growth curves show mean tumor volume ± SEM for 0.25×10⁶ (black), 0.5×10⁶ (yellow), 0.75×10⁶ (green) and 1×10⁶ (blue) cells over 15 days post-implantation. **B.** Liver weights and liver to body weight ratios of RIL-175 group compared to wild type livers at two weeks post-injection. Individual data points shown with mean ± SD. (*p < 0.05, n = 5-11)

3.3 Pancreatic cancer

3.3.1 Establishing subcutaneous PDAC injection models

In the introductory section of this thesis the challenges posed by PDAC and the need for a comprehensive investigation of its complex biological processes to develop more effective therapies were highlighted. The desmoplastic stromal reaction presents a significant hurdle for treatment as it facilitates tumor progression, invasion and also metastasis. The development

of subcutaneous injection models offers a valuable opportunity to investigate the desmoplastic stromal response in PDAC. Therefore, four different cell lines (FC1242, FC1245, FC1199, and Hy15549) were introduced into the right flank of female C57BL/6 mice at two different concentrations, either $1x10^5$ or $1x10^6$ cells. Tumor progression was analyzed throughout the experiment and is shown in Fig. 35A&B.

In addition to the growth of the tumors, the external examination of the tumors revealed cases of ulceration with visible ulcers or crater-like depressions on the surface of the tumor mass in approx. 60% of mice in the FC1245 and FC1199 groups, with no apparent dose-dependency between the $1x10^5$ and $1x10^6$ cell concentrations. Considering the desired experiment duration of approx. 3-4 weeks, the FC1245 cell line was considered unsuitable for further investigation. Even with the lower cell concentration of $1x10^5$, mice injected with this cell line were sacrificed by day 18 due to ulceration. Similarly, the FC1199 cell line was excluded from subsequent experiments due to a significant number of ulcerated tumors. In contrast, the two candidate cell lines, Hy15549 and FC1242, showed homogeneous growth, although experiments with Hy15549 at the higher $1x10^6$ concentration had to be terminated at day 23 when tumors reached the ethical endpoint size of 1.5 cm in diameter. Based on these observations, FC1242 at both concentrations and Hy15549 emerged as viable models for extended PDAC studies, with Hy15549 demonstrating optimal growth kinetics and experimental utility when implanted at the lower concentration of $1x10^5$ cells, allowing for the full duration of the intended experimental timeline.

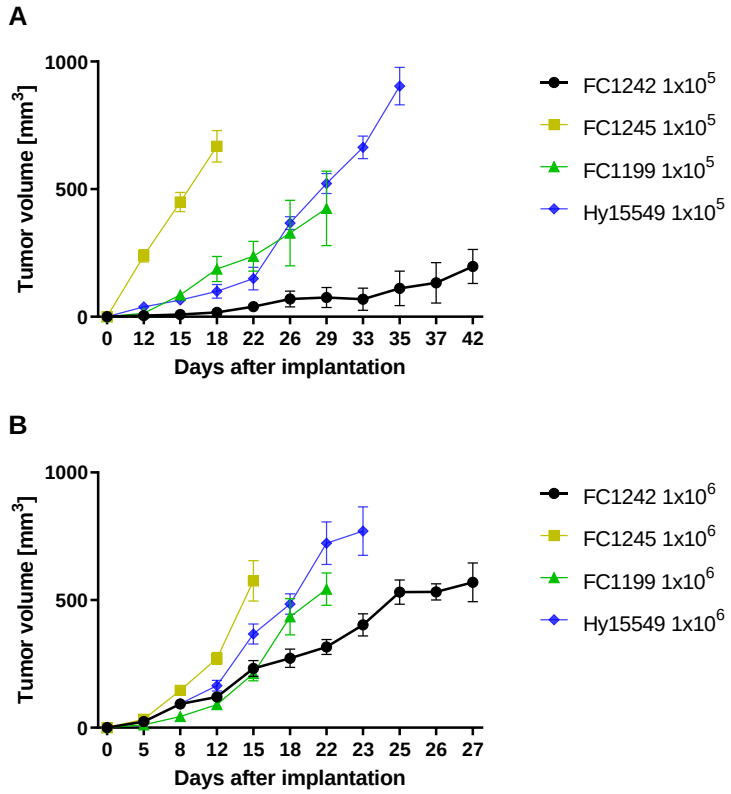

Figure 35: Tumor growth kinetics of different PDAC cell lines. A. Growth curves of s.c. tumors derived from FC1242, FC1245, FC1199 and Hy15549 cell lines implanted at $1x10^5$ cells. Tumor volume was measured up to 42 days post-implantation. **B.** Growth curves of tumors derived from the same cell lines implanted at $1x10^6$ cells. Tumor volume was measured over 27 days post-implantation. Data points represent mean tumor volume ± SD with n = 5/group.

3.4 Establishment of the Col3a1-CreERT2/iDTR mouse strain

A profound understanding of the interactions between CAFs within the TME is crucial to fully comprehend the immunosuppressive mechanisms induced by CAFs. The establishment of a novel mouse model is anticipated to provide deeper insights into these interactions and to unveil novel molecular targets for therapies targeting cancer-associated fibroblasts (CAFs). To establish a novel mouse strain, the Col3a1-CreERT2 strain was crossbred with the iDTR (inducible diphtheria toxin) mouse strain. The breeding strategy is demonstrated in Fig. 36A. Crossing of the iDTR strain to the Col3a1Cre strain renders CAFs sensitive to DT. The *lox*P-flanked STOP cassette, which inhibits DTR expression, is removed upon crossing with the tissue-specific Cre-expressing mouse strain, in this particular case, the Col3a1-CreERT2 mice. This process facilitates the expression of DTR in the targeted cell types, rendering them vulnerable to cell death upon diphtheria toxin (DT) injection. Before administering DT, activation of Cre recombinase should occur through Tam injections.

Following the breeding strategy, breeding pairs were arranged and the offspring analyzed using PCR to validate the genotype. In Fig. 36B, a representative agarose gel of the offspring mice is presented, featuring the marker, a positive control, and H_2O as a negative control (without DNA), along with three distinct offspring DNA samples: U846, U847 and U848. The H_2O Ctrl displayed a complete absence of bands. The results obtained reveal that all mice harbor the Cre gene (430 bp), while only mouse U847 a homozygous mutant iDTR allele indicated by a band approx. 300 bp in size. Mice U846 and U848 display heterozygosity for iDTR mutation, as evidenced by distinct bands at approx. 300 bp and 603 bp. Both homozygous and heterozygous mice are suitable candidates for further breeding to expand the cohorts, enabling future experiments.

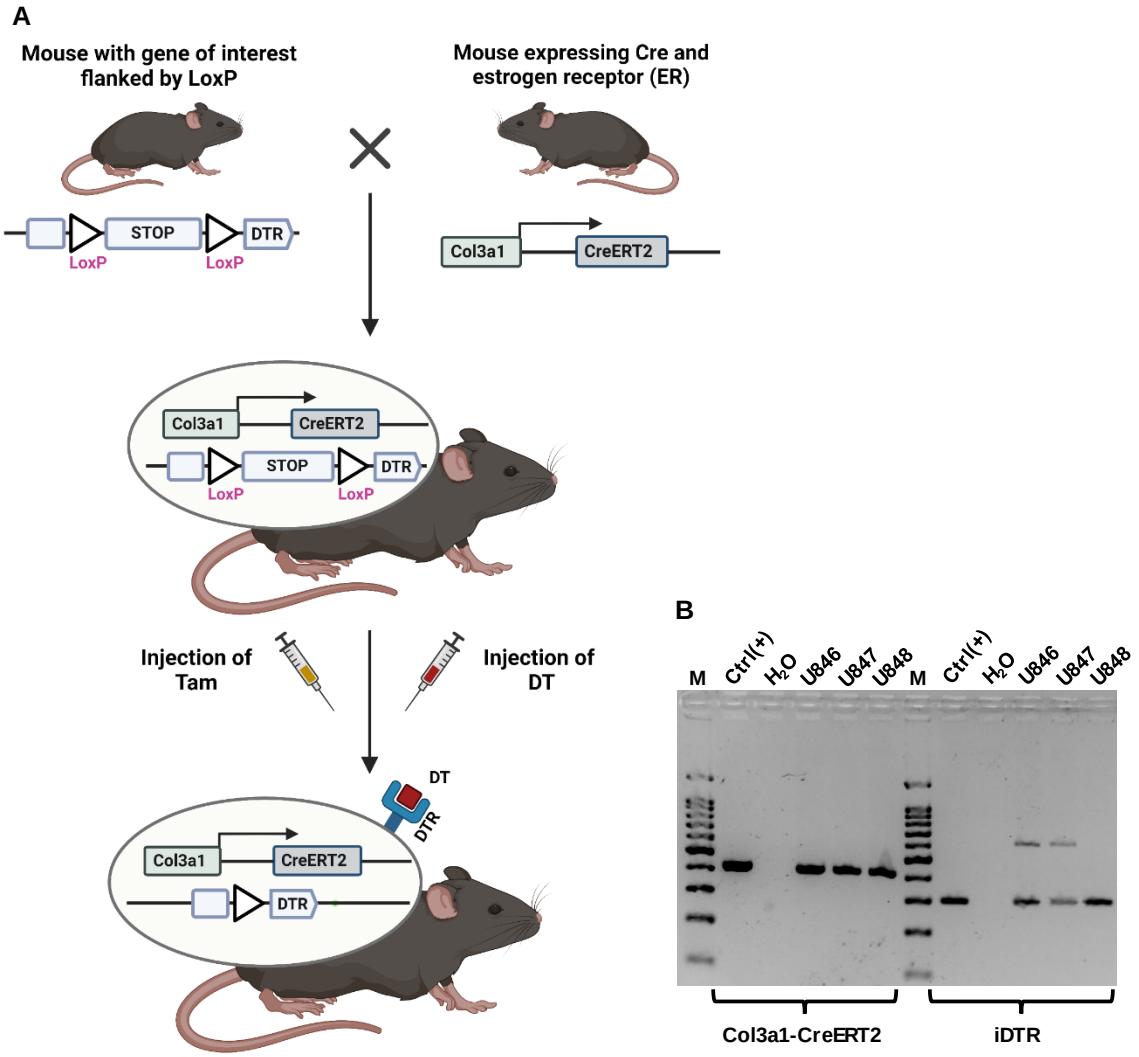

Figure 36: Generation and validation of a novel mouse model for targeted CAF depletion. A. Breeding strategy to create CAF-specific, diphtheria toxin (DT)-sensitive mice. Col3a1-CreERT2 mice, expressing tamoxifen-inducible Cre recombinase in CAFs, were crossed with iDTR mice carrying a *loxP*-flanked STOP cassette upstream of the diphtheria toxin receptor (DTR) gene. In offspring carrying both constructs, tamoxifen administration activates Cre, excising the STOP cassette and enabling DTR expression specifically in CAFs. Subsequent DT injection selectively depletes DTR-expressing CAFs. **B.** PCR genotyping results of offspring from the Col3a1-CreERT2 x iDTR cross. The gel shows DNA ladders (M), positive and negative (H_2O) controls, and three offspring samples (U846, U847, U848). All mice carry the Cre gene (430 bp band). U846 and U848 are heterozygous for the iDTR allele (bands at ~300 bp and 603 bp), while U847 shows homozygosity.

4 Discussion

In the ongoing battle against human disease, cancer is one of our most formidable adversaries. According to the WHO's 2022 data, a sobering picture emerges: cancer resulted in the premature loss of about 10 million lives globally, affirming its place as the second leading cause of death. This mortality burden is surpassed only by cardiovascular diseases, while infectious diseases remain a significant global health challenge as well. Beyond the devastating impact on human lives, cancer also imposes a tremendous economic burden on healthcare systems worldwide, as treatment costs continue to rise dramatically with the emergence of new therapies, placing significant financial strain on patients, families, and healthcare infrastructure. At the heart of cancer's complexity is the TME, a dynamic cellular system that plays a critical role in cancer development, progression, and resistance to treatment. The present study centers on exploring the complex dynamics of the TME in desmoplastic cancers, with a specific focus on lung cancer, HCC and PDAC. These aggressive cancer types are known for their dense stromal reaction, which creates significant barriers to both scientific understanding and effective treatment. My study aimed to further uncover especially the roles of CAFs and TAMs and defined novel pharmacological/immunological interventions in cancer progression. Therefore, various injection models to investigate tumor-stroma dynamics *in vivo* were established and used. A key aspect of this thesis involved our unique bi-transgenic mouse model for selective inactivation of TGF-β signaling in CAFs.

Other strategies encompassed the use of a Fra-2 ASO, which affects multiple processes, namely proliferation, ECM deposition and inflammation. Additionally, rapamycin, an mTOR inhibitor that interacts with several cellular pathways, was applied to treat HCC in an orthotopic mouse model. Both therapies were investigated for their potential to induce a phenotypic switch of TAMs towards the M1 phenotype. Moreover, the goal was to establish a novel Col3a1-CreERT2/iDTR mouse model for complete CAF depletion and laying the groundwork for future research in this field. In the following sections, the results of this thesis and the potential consequences for therapeutic concepts will be discussed.

4.1 Temporal dynamics of TGFβRII K.O. in CAFs: Impact on tumor growth and environment in a murine subcutaneous lung cancer model

In the initial *in vivo* experiment, the effect of TGFβRII K.O. uniquely in CAFs on tumor growth and ECM composition was investigated using our Col3a1-CreERT2/TGFβRII fl/fl mouse model

in the context of s.c. lung cancer. To elucidate temporal dynamics of TGF-β signaling disruption in CAFs, early and late tamoxifen administrations were performed.
One of the most striking findings was the differential impact of early vs late TGFβRII K.O. on tumor growth (Fig. 14). In the early tamoxifen group, we observed a significant reduction in tumor volume in the floxed mice compared to the control group. This effect was particularly strong in tumors derived from higher cell numbers ($7x10^5$ cells). This observation suggests that early disruption of TGF-β signaling in CAFs may interfere with critical processes in the initial stages of tumor establishment and growth.
Interestingly, the late tamoxifen group was less affected of TGFβRII K.O., where differences in tumor volumes between floxed and control mice were not statistically significant. It is possible that the early stages of tumor development are more dependent on TGF-β-mediated interactions between CAFs and tumor cells, while later stages may involve alternative signaling pathways or compensatory mechanisms that can partially overcome the loss of TGF-β signaling in CAFs.

The observed reduction in tumor growth following early TGFβRII knockout aligns with certain studies. For instance, the findings from Buenrostro *et al*. (2018) provide supporting evidence for the theory that TGF-β signaling may be more critical in the early stages of tumor development than later stages [161]. In their study examining TGF-β inhibition in breast cancer bone metastasis models, they observed that early TGF-β inhibition had more pronounced effects on myeloid cell populations and tumor burden compared to inhibition at later disease stages.
Specifically, the authors found that systemic TGF-β inhibition altered the expansion of immature and mature myeloid cell populations primarily in the early and middle stages of tumor-induced bone disease. However, these effects were not as evident in the late disease stage when extensive bone loss and tumor burden were already present. Furthermore, the study demonstrated that genetic deletion of TGF-β receptor II in myeloid cells ($TGF\beta RII^{MyeKO}$) resulted in significant reductions in tumor burden (and osteolytic lesions as well) compared to wild type controls. Importantly, these differences were prominent in earlier disease stages, while the effects became less significant as the disease progressed to later stages. These observations align with the hypothesis that early stages of tumor development may be more dependent on TGF-β-mediated interactions between stromal cells (in this case, myeloid cells) and tumor cells. As tumors progress to more advanced stages, they may develop alternative signaling pathways or compensatory mechanisms that can partially overcome the loss of

TGF-β signaling, explaining the diminished effects of TGF-β inhibition in later disease stages [161].
The temporal aspect of our findings adds an important layer of complexity to our understanding of TGF-β's role in the TME and suggests that the timing of therapeutic interventions targeting this pathway may be critical for achieving optimal anti-tumor effects.

The analysis of collagen deposition using Sirius Red staining revealed intriguing patterns (Fig. 15 and Fig.16). In both early and late tamoxifen groups, a higher collagen deposition was observed in tumor margins compared to tumor cores, regardless of TGFβRII status.
The impact of TGFβRII knockout on collagen deposition differed between the early and late tamoxifen groups. In the early TGFβRII deletion group, collagen levels were comparable between knockout and control tumors, with the knockout group showing slightly higher (though not statistically significant) collagen deposition in the tumor margin. Conversely, in the late tamoxifen group, a trend towards lower collagen deposition was found in the knockout tumors, particularly in the tumor core. These findings suggest that the relationship between TGF-β signaling in CAFs and collagen production is not straightforward and may be influenced by the stage of tumor progression.
TGF-β plays a multifaceted role in CAFs, simultaneously guiding collagen production and modulating fibroblast behavior. The observed differences between early and late intervention groups could be explained by a temporal shift in the predominant TGF-β responses: early deletion may primarily affect CAF activation and proliferation dynamics, while in later stages, its impact on matrix production and collagen deposition may become more prominent. This stage-dependent duality could contribute to the apparently contradictory effects observed in our model.
The maintenance or even slight increase in collagen levels in the early knockout group, despite reduced tumor growth, indicates that collagen production can be decoupled from tumor progression under certain conditions. This observation challenges the simplistic view of collagen/excess EMC as a universally pro-tumorigenic factor.
The trend towards reduced collagen deposition in the late tamoxifen group aligns more closely with the traditional view of TGF-β as a promoter of fibrosis and ECM production, usually in non-dividing (myo-)fibroblasts. However, the lack of statistical significance in this difference suggests the involvement of compensatory mechanisms or alternative pathways that can partially maintain collagen production in the absence of TGF-β signaling via TGFβRII in CAFs. Evidence from multiple sources implies that TGFβRI and non-canonical pathways can compensate for the loss of TGFβRII in our model, allowing partial TGF-β signaling to persist

despite the deletion of receptor II. This hypothesis is further supported by findings from Khalil and colleagues who demonstrated that the combined deletion of Tgfbr1/2 and Smad3 was necessary to significantly reduce cardiac fibrosis, whereas Smad2 deletion alone had minimal impact. Their study highlighted the dominance of Smad3 in mediating fibrotic responses and provided evidence that non-canonical pathways, such as MAPK signaling, contribute to TGF-β-driven fibroblast activity. Notably, transcriptomic analyses revealed that Tgfbr1/2 deletion altered gene expression profiles distinct from those affected by Smad2/3 deletion, indicating broader regulatory functions [162].

Mu *et al*. (2016) further support the concept of compensatory signaling in their analysis of epithelial TGF-β signaling in liver fibrosis. The study showed that the deletion of TGFβRII in liver epithelial cells surprisingly had no effect on the development of liver fibrosis across various mouse models. These findings suggest that alternative signaling pathways can be activated to maintain TGF-β-mediated fibrogenesis even when a central receptor of the canonical pathway is absent [163].

The Wnt/β-catenin signaling pathway emerges as a relevant mechanism that may contribute to collagen production in our TGFβRII knockout model. As reviewed by Somanader *et al*. (2024), TGF-β1 can influence the Wnt/β-catenin cascade through its non-canonical p38 MAPK pathway by antagonizing DKK-1 (a Wnt inhibitor) and inactivating GSK-3β. Conversely, the Wnt/β-catenin pathway can enhance TGF-β signaling, creating a positive feedback loop. This cross-talk between pathways could maintain pro-fibrotic signaling even when canonical TGF- β signaling is impaired due to TGFβRII deletion, potentially explaining our observations of continued collagen deposition [164].

Furthermore, the persistence of collagen type I expression despite TGFβRII knockout in CAFs might be partially explained by the contribution of cancer cell-derived collagen, as may occur in epithelial-mesenchymal transition (EMT), as also shown for HCC by our group [165]. Similarly, Chen *et al*. (2022) have shown that pancreatic cancer cells can produce collagen, even though with a distinct composition compared to fibroblast-derived collagen. As highlighted in this study, pancreatic cancer cells predominantly express the collagen α1(I) chain, forming homotrimeric collagen structures (α1(I)3)), in contrast to the heterotrimeric collagen (α1(I)2α2(I)) produced by normal fibroblasts. This cancer cell-derived α1(I) trimer collagen may play a role in this mechanism, though it is likely to have only a moderate impact [166]. While our study primarily focuses on CAF-mediated effects, we acknowledge that our experimental design cannot completely rule out collagen contributions from other cell types.

Nevertheless, our approach employs a highly specific Cre mouse model targeting active myofibroblasts, which is based on the biological principle that in soft tissue, procollagen I

expression is consistently accompanied by procollagen III expression. Osteoclasts represent the only exception to this principle, which is why they were intentionally excluded from our targeting approach.

To further validate our hypotheses regarding the temporal effects of TGF-β on CAF behavior, subsequent studies could employ double labeling of vimentin-positive fibroblasts with Ki67 to assess proliferation rates across different experimental conditions and timepoints, potentially revealing how TGF-β's effects on CAF proliferation vary throughout tumor progression.
Future studies investigating the expression of other growth factors and cytokines that drive proliferation—particularly PDGF-B, which has a stronger effect than PDGF-A—as well as CTGF, could offer valuable insights into potential compensatory mechanisms.

The expression of α-SMA, which indicates activated myofibroblasts, yielded also unexpected results (Fig. 17 and Fig. 18). In the early tamoxifen group, TGFβRII knockout mice demonstrated increased α-SMA expression both at the tumor margin and within the tumor core, challenging the traditional view of TGF-β as the primary driver of myofibroblast activation. Several hypotheses could explain this paradoxical increase in α-SMA expression.
As mentioned earlier regarding collagen production, TGF-β exhibits dichotomous effects on CAFs. This paradoxical increase in α-SMA expression can be explained by the opposing regulation of proliferation vs matrix synthesis by TGF-β in fibroblasts. TGF-β typically inhibits proliferation while promoting matrix synthesis in fibroblasts. When TGF-β signaling is disrupted through TGFβRII K.O., this balance may shift, potentially favoring proliferation of specific fibroblast subpopulations. Notably, α-SMA is a marker of a subpopulation of proliferating myofibroblasts, while vimentin-positive cells (excluding endothelial cells) represent the total fibroblast population. This suggests that TGFβRII K.O. may increase the proportion of proliferating myofibroblasts within the total fibroblast population.

Similar to observations regarding collagen deposition, the absence of classical TGF-β signaling could also lead to alternative fibrogenic signaling pathways. The Wnt pathway appears highly relevant, aligning with earlier discussions on its potential role in compensating for impaired TGF-β signaling. Future studies could test this hypothesis through PCR analysis examining the expression of LGR5/6 and Wnt1/Wnt3 as the primary mediators in this compensatory mechanism.

The absence of classical TGF-β signaling and the possible alternative fibrogenic signaling, e.g., via the Wnt pathway, in CAFs could also alter the overall composition of the stromal cell population, potentially favoring the expansion of a subset of fibroblasts that express high levels of α-SMA independently of TGF-β.

In contrast, the late tamoxifen group showed an opposite trend, with higher α-SMA expression in the control group compared to the knockout tumors, suggesting that the role of TGF-β signaling in maintaining the activated state of CAFs may become more prominent in later stages of tumor development.

While α-SMA expression is commonly used as a marker of CAF activation, it may not fully capture the diversity of these cells. Future research should incorporate additional markers such as FAP or PDGFR to gain a deeper understanding of how TGFβRII knockout impacts CAFs. Co-staining techniques could provide more detailed insights into the different CAF subtypes and their specific activities.

These first findings highlight the need for careful consideration of the timing of interventions, targeting the TGF-β pathway, leading us to the next experiment, using a consistent cell count and delayed administration of tamoxifen.

4.2 Effects of TGFβRII K.O in CAFs on tumor growth and immune infiltration in a murine subcutaneous lung cancer model

In the previous analysis of the TME in s.c. LuCa6 tumors, initial findings highlighted key aspects such as collagen distribution and α-SMA expression, important indicators of tumor-stroma interactions. Building on these results, the experiment was repeated with a more consistent design, using a uniform number of LuCa6 cells injected bilaterally into Col3a1-CreERT2/TGFβRII fl/fl mice, with an adjusted treatment protocol. Col3a1-CreERT2 mice with intact TGFβRII served as Ctrl.

Although minimal differences in tumor progression were noted initially (based on caliper measurements during the experiment), more distinct differences in tumor growth emerged by the end of the experiment. Interestingly, regardless of identical inoculation conditions, the tumors on each flank of individual mice displayed disparate growth patterns, resulting in asymmetrical sizes (Fig. 19). As a result, tumors were categorized as the lead tumor and its smaller contralateral tumor for further analysis, rather than distinguishing by the injection site. Multiple hypotheses will be proposed to explain the mechanisms behind the differing tumor growth patterns within a single host organism.

The difference in growth between lead and contralateral tumors may be attributed to local variations in the TME. Factors such as blood vessel density, ECM composition and stromal cell populations can vary even within the same animal, thus, influencing tumor growth [167]. Slight variations in the initial injection process, such as minor differences in the exact location or depth of injection, could impact the establishment of the tumor. Regions with better vascularization might support more rapid tumor growth, leading to the development of a lead tumor.

Another important aspect is the clonal evolution: even when injecting the same cell line, genetic or epigenetic changes can occur. Shifts in the surrounding milieu can significantly alter how these genetic changes affect the overall fitness of cancer cells, resulting in the development of more aggressive clones in one tumor compared to another [168].

Furthermore, the immune response to the tumors may differ. The lead tumor might have developed mechanisms to evade immune surveillance more effectively. Conversely, the immune response to the lead tumor might suppress the growth of the contralateral tumor through so-called concomitant immunity [169].

An additional concept, similar to Stephen Paget's "soil and seed" hypothesis in metastasis research, may also be relevant. The lead tumor may be more efficient at competing for nutrients and growth factors, potentially inhibiting the growth of the tumor on the opposite side [170]. "Seed" refers to the cancer cells themselves, which have varying metastatic potential. "Soil" represents the microenvironment of different organs or tissues, where not every tissue provides favorable conditions for metastasis growth. Although the hypothesis was originally developed for metastases, it can also be applied to the behavior of competing tumors in the same mouse.

Another significant mechanism, initially discovered through Judah Folkman’s groundbreaking research on tumor angiogenesis, involves the systemic production of anti-angiogenic factors by the lead tumor. This concept suggests that the lead tumor secretes basement membrane collagen-derived anti-angiogenic peptides, such as endostatin and tumstatin (derived from collagen IV, XVIII, and XV, respectively). These peptides enter the circulation and specifically inhibit angiogenesis in the contralateral tumor, effectively restricting its growth [171]. This systemic inhibition of angiogenesis represents a plausible explanation for the observed asymmetry in bilateral tumor models.

Lastly, mechanical stress also requires mention, as differences in local mechanical stresses between the two injection sites could also influence tumor growth [172].

Since bilateral injections were also performed in the previous experiment, the findings must be viewed with caution.
Nevertheless, taken all together, the inactivation of TGFβRII in CAFs resulted in a marked decrease (up to 50%) in tumor burden, with both volume and mass (Fig. 19C).

Similar to the previous experiment, there was no significant difference between the two cohorts in terms of collagen distribution (Fig. 20). As the potential reasons have already been mentioned in the previous chapter, they will not be discussed again. Regarding IHC, α-SMA levels remained also consistent across all experimental groups, showing no discernible variations (Fig. 21). However, the qPCR analysis revealed a significant upregulation of α-SMA transcripts in the floxed mice (Fig. 23A). This discrepancy between protein and mRNA levels reveals again the dichotomous nature of TGF-β signaling, highlighting its contrasting effects on proliferation (α-SMA expression) and matrix synthesis, as observed in the variable collagen deposition patterns across different tumor stages.
By using flow cytometry, immune cell infiltration and TME composition were further analyzed (Fig. 24). The analysis of immune cell populations within the tumors revealed a significant reduction in CD8+ T cells in the TGFβRII knockout group.
While blocking TGF-β signaling can enhance anti-tumor immunity, often leading to increased T cell infiltration and activation, one has to keep in mind that the K.O. of TGFβRII occurred only in CAFs, and not in the entire mouse. This change might have caused unexpected shifts in the secretion profile of CAFs and their interactions with other cells.
The study by Feig *et al*. on PDAC provides a compelling example of an alternative pathway. Their work demonstrated that CXCL12, produced by FAP+ CAFs, prevents T cell infiltration into tumor-affected areas. By inhibiting the CXCL12 receptor, they successfully redirected T cells towards cancer cells, enhancing the effectiveness of immunotherapies.
Therefore, we can hypothesize that the K.O. in our model may have altered other signaling pathways within CAFs. This could have led to changes in the production of various factors, including chemokines like CXCL12, CTGF, WNT proteins or others, ultimately resulting in the observed reduction of CD8+ T cells [173].
As mentioned above, smaller tumors likely have different vascularization patterns or metabolic profiles that could influence T cell recruitment and survival. Additionally, the change in CAF phenotype could affect their antigen-presenting capabilities or their ability to provide co-stimulatory signals to T cells [68].
The increased infiltration of CD4+ T cells in the TGFβRII knockout group further complicates the immune response in this mouse model. Similar findings were reported in other studies.

Özdemir *et al*. revealed that depleting CAFs in pancreatic cancer unexpectedly increased immunosuppression, evidenced by higher levels of immunosuppressive CD4+ FoxP3+ Tregs in mouse tumors [68]. Despite the significant differences observed in CD8+ and CD4+ T cell populations in the flow cytometric analysis between the groups, it's noteworthy that no significant difference was found in CD25 expression. This is particularly interesting given that CD25, the alpha chain of the IL-2 receptor, is often associated with T cell activation and is a characteristic marker of Tregs only when expressed at very high levels, while moderate CD25 expression is found on various activated T cells. The lack of difference in CD25 levels suggests that while the overall T cell populations were affected, the activation state might have remained constant across the groups [174]. Additionally, FoxP3, although typically associated with Tregs, also marks suppressive myeloid cells, which may influence the immune landscape.
The IHC results for CD4+ and FoxP3+ cells in both tumor margin and core regions showed only minimal differences between floxed and Ctrl group (Fig. 22B). Interestingly, the CD8+ IHC data partially aligns with the flow cytometry results, showing a trend towards increased CD8+ T cell infiltration in the floxed group, particularly in the tumor core where the difference was statistically significant (Fig. 22B and Fig. 24B). These differences highlight the importance of considering both overall immune cell numbers and their localization within the tumor. The enhanced CD8+ T cell presence in the tumor core of floxed mice, as revealed by IHC, suggests that while overall CD8+ numbers may be reduced (as per flow cytometry), their distribution within the tumor may be altered, potentially affecting their anti-tumor efficacy.

The analysis of macrophage populations did not reveal significant differences between the TGFβRII K.O. and control groups (Fig. 22A and 24B). The lack of observable changes in macrophage numbers suggests that TGF-β signaling in CAFs may not be a critical determinant of macrophage recruitment or polarization in this model. However, it is important to note that macrophage function can be altered without changes in overall numbers or surface marker expression. Besides, the number of dendritic cells and neutrophil granulocytes remained unchanged in both experiment groups, with no significant differences observed.
Although not significant, a slight shift towards a conventional M2-type macrophage polarization, particularly at the tumor margin, was observed in IHC analysis. As stated before, altered CAF signaling due to the TGFβRII K.O. could lead to changes in cytokine production, compensatory immunosuppressive mechanisms or shifts in the overall TME. But further investigations would be necessary.
The significant increase in vimentin expression (IHC) observed in the tumor core of floxed mice was an unexpected finding, as vimentin upregulation is typically associated with increased

invasiveness and metastatic potential [175] (Fig. 22C). Possible explanations despite TGF-β loss in CAFs include other mesenchymal-promoting pathways, such as Wnt, Hedgehog, or Notch signaling. Additionally, changes in tumor cellular composition or a stress response resulting from hypoxia or nutrient deprivation due to reduced tumor growth could also contribute to this observation.

The qPCR analysis revealed some notable findings. Increased transcripts of α-SMA and TGFβRII were observed in the knockout mice (Fig. 23A). Additionally, the maintenance or even increase in collagen transcript levels (*col1a1* and *col3a1*) in these mice supports the idea of compensatory mechanisms once again (Fig. 23B).
In conclusion, the present study demonstrates that the K.O. of TGFβRII in CAFs led to significant reduction in tumor growth in a s.c. murine lung carcinoma model. However, the underlying mechanisms appear to be more complicated, including unexpected changes in the composition of the ECM, activation of myofibroblasts and immune cell infiltration. While the results demonstrate the potential of such approaches to reduce tumor growth, they also highlight the need to carefully consider the far-reaching effects on the TME. The timing of TGF- β pathway disruption may be crucial for therapeutic outcomes, affecting clinical trial design and treatment protocols targeting this pathway. Moreover, advanced techniques like single-cell RNA sequencing, spatial transcriptomics, and multiplexed imaging could offer a more detailed view of the cellular and molecular changes resulting from TGFβRII K.O. in CAFs. Future studies could also focus on combination therapies, targeting both TGF-β signaling and other elements of the TME. For example, combining TGFβRII K.O. in CAFs with immune checkpoint inhibitors or therapies targeting other stromal components could potentially enhance anti-tumor effects via synergistic interactions. Additionally, therapies targeting other CAF-related signaling pathways, such as Wnt/β-catenin, Hedgehog, CTGF, and others, should be considered for their potential synergistic effects in modulating the TME and enhancing anti-tumor responses.

4.3 Synergistic effects of rapamycin and Fra-2 ASO combination therapy in orthotopic murine HCC

The following chapter addresses the efficacy of rapamycin, an mTOR inhibitor, and Fra-2 ASO in treating HCC using an orthotopic mouse model. The combination of these agents represents a multifaceted approach to HCC treatment, targeting not only cancer cell proliferation but also the TME to achieve a synergistic anti-tumor effect. Rapamycin was anticipated to suppress cell proliferation and tumor growth by inhibiting mTORC1, a key cellular pathway often

dysregulated in HCC. This pathway stimulates cell proliferation primarily by sensing protein and amino acid availability, making mTORC1 a central target in fasting-mimicking dietary approaches to cancer treatment. This inhibition was expected to impact various downstream processes involved in cell growth, metabolism, and survival. Additionally, in previous studies rapamycin has also shown potential in reprogramming TAMs from a tumor-promoting M2 phenotype to an anti-tumoral M1 phenotype, potentially enhancing its anti-cancer effects. Fra- 2 ASO, targeting a key member of the AP-1 transcription factor family, was hypothesized to modulate the TME by affecting both CAFs and TAMs. Fra-2 overexpression drives skin and lung fibrosis [176], [127]. Its inhibition was expected to have an anti-fibrotic effect, potentially reducing the desmoplastic reaction in HCC and improving drug delivery and efficacy and potentially also affect the TME in a beneficial way [177]. Thus, combination therapy was believed to offer a dual approach by directly inhibiting tumor cell proliferation while also modifying the TME, aiming to enhance overall therapeutic outcomes.

All treatment approaches demonstrated remarkable efficacy in reducing tumor burden, as evidenced by decreased liver weights and liver to body weight ratios. The roughly 50% reduction in these parameters compared to the untreated group is outstanding, bringing the treated mice close to the levels observed in wild type mice (Fig. 25B). The findings of the MU-Gal assay provided a further objective measurement of tumor burden, providing even more accurate intrahepatic insights and confirming previous findings (Fig. 26). A strong reduction in β-galactosidase activity in all treatment group was observed. The combination therapy might have changed the dynamics of the tumor response. Initially, the combined treatment may have a stronger anti-tumor effect, but an adaptation phase could follow, as suggested by the slight increase in β-galactosidase activity at measurement. Sharma *et al*. discovered a subpopulation of 'drug-tolerant' cancer cells with reduced drug sensitivity. This state is dynamically regulated within the cell population, representing a temporary survival strategy. These findings may explain the findings in the combination therapy group. The presence of such transiently drug-tolerant cells could account for the slightly higher β-galactosidase activity which were shown, reflecting the tumor's adaptive response to treatment [178]. Additionally, counteracting effects may arise in the combination therapy due to the distinct cellular targets: Fra-2 inhibition primarily affects macrophages and fibroblasts, while rapamycin acts on both cancer cells and immune cells in the TME, potentially creating complex interactions that partially offset their individual benefits.

The observed heterogeneity of HCC in the untreated Ctrl group, which is known from the literature, is also striking [179]. This heterogeneity highlights the importance of developing

targeted therapies that can address the diverse molecular landscapes of HCC tumors. However, the present model stands out with good homogeneity in comparison to other syngeneic and orthotopic HCC models, with the additional advantage of rapid development.

The analysis of serum toxicity markers (creatinine, total bilirubin, ALAT, and ASAT) suggested a favorable safety profile for all treatment regimens (Fig. 27). The absence of significant elevations in these markers, particularly for renal and hepatic function indicators, is encouraging for the potential clinical translation of these therapies.
However, the slightly elevated ALAT levels in the combination therapy group, while still within an acceptable range, warrant careful consideration. This elevation could indicate a mild hepatocellular stress response to the combined treatment. Previous studies, as a meta-analysis of everolimus, have reported similar findings of mTOR inhibitors, suggesting a need for careful monitoring of liver function during treatment [180].

Sirius Red staining, a well-established method for visualizing and quantifying collagen deposition in tissue sections, revealed a statistically significant decrease in fibrotic areas in all treatment groups compared to the untreated control (Fig. 28). This observation suggests that Rapa, Fra-2 ASO, and their combination therapy effectively mitigate the excessive ECM accumulation characteristic of liver fibrosis as a major predisposition of HCC.

To further elucidate the molecular mechanisms underlying these anti-fibrotic effects, the mRNA expression levels of two key collagens, *col1a1* and *col3a1*, which are primary components of the fibrotic ECM were examined. The qPCR analysis of Col1a1 revealed a striking nine-fold reduction in expression across all treatment groups compared to the untreated control (Fig. 33A). This substantial decrease in *col1a1* mRNA levels aligns with the histological findings and underscores the potent anti-fibrotic action of the investigated therapies at the transcriptional level. Similarly, the expression pattern of *col3a1* mirrored that of *col1a1*, albeit with less pronounced differences (Fig. 33B). While the reduction in *col3a1* mRNA levels did not reach statistical significance, the consistent trend of lower expression in all treatment groups, further supporting the anti-fibrotic effect of these treatments.
The observed effects on collagen expression are particularly noteworthy given the central role these proteins play in the progression of liver fibrosis. *Col1a1* and *col3a1* are primarily if not exclusively produced by activated hepatic stellate cells and myofibroblasts in response to chronic liver injury, such as that seen in HCC. The significant downregulation of these

collagens following treatment clearly demonstrates the modulation of the activation or function of these fibrogenic cell populations.

The immunological composition of the TME presents a more complex profile, particularly in relation to macrophage polarization and T cell populations. Contrary to the initial hypothesis of a shift towards an anti-tumoral M1 macrophage phenotype, both IHC and mRNA analyses demonstrated a heterogeneous expression pattern across various macrophage markers.
The IHC analysis showed a significant reduction in CD68+ macrophages across all treatment groups (Fig.30A). CD68 is widely recognized as a pan-macrophage marker, and its decreased expression indicates a general loss of macrophages in the TME following treatment. The combination therapy demonstrated the most pronounced effect, followed closely by Fra-2 ASO and rapamycin monotherapies. Interestingly, the analysis of YM1 expression, as mentioned before, typically associated with M2-like macrophages, revealed unexpected results (Fig. 30B). Contrary to the initial hypothesis, rapamycin treatment led to an increase in YM1 levels compared to the untreated control. In contrast, both Fra-2 ASO monotherapy and the combination treatment resulted in slight, non-significant decreases.
The qPCR analysis further complicated the picture of macrophage phenotypes in the TME. Rapamycin treatment led to elevated expression of M2-associated markers YM1, CD206 and IL-10 (Fig. 32C). It's influence on macrophage polarization seams more complex, potentially leading to mixed M1/M2 phenotypes rather than a clear shift. Worth noting, previous work from our group (Pickert G *et al*., manuscript submitted) has demonstrated that M2-type markers can be upregulated in early time inflammatory monocytes-macrophages.

The mTOR pathway, comprising two distinct complexes (mTORC1 and mTORC2), plays a crucial role in macrophage polarization. While rapamycin primarily inhibits mTORC1, its impact on mTORC2 can vary depending on temporal and contextual factors. This differential effect on the two complexes may contribute to the observed heterogeneity in macrophage phenotypes. Macrophage populations are heterogeneous by nature, and their subsets have different sensitivities to rapamycin. This diversity might lead to different responses within the same tissue. In addition, rapamycin may affect pathways beyond mTOR signaling, thereby contributing to the process of polarization.
The significantly enhanced expression of IL-10 in the treatment groups, particularly in the rapamycin therapy, suggests a potential immunomodulatory effect. However, it is essential to consider that other liver cell types may also secrete IL-10, making it difficult to definitively conclude that the elevated IL-10 levels are solely attributed to M2 macrophage polarization.

While IL-10 is often regarded as a marker for M2 polarization, particularly in cell culture systems, the *in vivo* situation in mice is considerably more complex. The liver is composed of a diverse array of cell types, including hepatocytes, regulatory T cells, dendritic cells, and B cells, all of which can contribute to the local cytokine milieu [181]. Thus, the observed increase in IL-10 in the treated group may reflect contributions from these various cellular sources rather than being exclusively indicative of M2 macrophage activity. Consequently, although qPCR offers valuable information regarding cytokine expression levels, it does not clearly specify the cellular sources of IL-10 within the liver microenvironment.

Moreover, the mRNA analysis revealed an unexpected outcome regarding Fra-2 expression (Fig. 32B). Surprisingly, Fra-2 ASO treatment did not lead to a significant downregulation of Fra-2 mRNA levels as initially hypothesized. This result could be attributed to several factors. One possibility is the activation of compensatory mechanisms that maintain Fra-2 levels in response to the ASO treatment, a phenomenon observed in other gene knockdown studies [182]. Additionally, the timepoint of analysis might not have captured the full dynamics of Fra- 2 modulation. The observation that rapamycin monotherapy led to increased Fra-2 levels while Fra-2 ASO did not achieve the anticipated downregulation may be explained by differential targeting of these treatments. Future investigations could explore the hypothesis that rapamycin predominantly affects cancer cells, while ASOs may be preferentially taken up by cells within the tumor microenvironment rather than by HCC cells themselves. This differential uptake pattern has been observed with other ASO therapeutics, where studies revealed preferential ASO accumulation in stromal and immune cells with limited uptake into tumor cells [183]. Testing this hypothesis would require studies using cell-specific markers and extended time-course analyses.

The iNOS expression pattern, with higher levels in the untreated control group compared to treatment groups is intriguing (Fig. 32A). While iNOS is typically associated with M1 macrophages and pro-inflammatory responses, its role in tumor biology is complex. Lechner *et al*. (2005) highlight that iNOS expression is observed in various human malignancies, often at higher levels compared to adjacent normal tissue. The effects of iNOS-derived NO on tumor development are multifaceted, capable of both promoting and inhibiting tumor growth depending on its concentration in the TME [184] . Regarding CD38 expression, a significant decrease in the untreated (Ctrl) group compared to the other groups was shown (Fig. 32A). However, CD38 also can be expressed on various immune cells, and its role in tumor immunity is multifaceted. The higher CD38 expression in the treatment groups, especially Rapa,

suggests these treatments may be modulating the immune cell composition or activation state in the TME, potentially towards a more anti-tumor phenotype.

Furthermore, IHC analysis of CD4+ T cells, FoxP3+ regulatory T cells, and Granzyme B+ cells did not reveal any statistically significant differences across the treatment groups, contrary to expectations for effective anti-tumor therapy (Fig. 31). This suggests that these aspects of the adaptive immune response were not significantly altered by our treatments.
The most notable finding was the significant difference in CD8+ cytotoxic T lymphocyte (CTL) populations (Fig. 31C). Surprisingly, the control group exhibited the highest percentage of CD8+ cells, significantly exceeding both the rapamycin and combination treatment groups. This counterintuitive result raises questions about the nature of the immune response in this HCC model. This unexpected pattern of CD8+ T cell infiltration could indicate that the treatments, especially rapamycin and the combination therapy, are altering the TME in ways that affect T cell recruitment or maintenance. Alternatively, these treatments might be inducing a more focused CTL response, with fewer but potentially more tumor-specific T cells present. It's important to note that the mere presence of CD8+ T cells does not necessarily indicate their functional state or tumor-specificity. The higher number of CD8+ cells in the control group might represent an ineffective accumulation of T cells, while lower numbers in treatment groups could potentially represent a more effective, targeted population of tumor-reactive CTLs. Further functional studies are needed to fully interpret these IHC findings and their implications for anti-tumor immunity in this HCC model.

Despite the fact that the results are promising, several limitations should be acknowledged. The use of a single HCC cell line (Dt81Hepa1-6/βgeo) in the orthotopic model may not fully capture the heterogeneity of human HCC. Future studies should consider the use of different cell lines or even patient-derived xenografts to better represent the diversity of HCC.

In conclusion, this experiment demonstrates the potential of combining rapamycin and Fra-2 ASO as a novel therapeutic approach for HCC, especially in HCC of longer duration and with a more pronounced immune suppression by the TME. This is the rule for human HCC, where TAMs are major cell types infiltrating most TMEs, accounting for 20-40% of immune cells [185].

Still, the significant reduction in tumor burden, coupled with anti-fibrotic effects, provides strong evidence for further investigation. Overall, the model is suitable for a fast investigation of therapies that may gain interest in the future.

4.4 Establishing novel murine models for HCC and PDAC research

As illustrated in the previous chapters, the development of effective therapies for HCC and PDAC remains an enormous challenge. To overcome this issue, researchers are working on preclinical models to mirror the diverse aspects of these tumor entities. This chapter details the efforts to establish novel mouse models, encompassing s.c. and orthotopic injection models, as well as a genetically engineered mouse model (GEMM) to study CAFs.

Although the cell lines used in this thesis had been previously characterized in the literature, it remains essential to conduct preliminary studies to determine the ideal seeding density and growth conditions under the unique parameters of one's own research environment. This approach ensures the reproducibility of results and allows for the optimization of experimental protocols, as the cell numbers and growth kinetics reported in published studies may not always be transferable due to variations in factors, namely culture conditions, mouse strains and other microenvironmental influences.

To develop further HCC models, the RIL-175 cell line was used. This approach became necessary due to the failure of Dt81Hepa1-6/βgeo cells to grow subcutaneously.

For the s.c. model, several concentrations (0.25 – 1x10^6) of RIL-175 cells into the right flank of C57BL/6 mice were injected and tumor growth monitored over 15 days. The results showed a clear concentration-dependent growth pattern, with higher cell numbers leading to more rapid tumor development (Fig. 34A). This model provides a valuable tool for rapid therapy screening, offering a straightforward method for measuring tumor volume.

To broaden the s.c. model, an orthotopic RIL-175 model was tested by injecting 0.5x10^6 cells intrasplenically into male C57BL/6 mice (Fig. 34B). However, this approach led to rapid tumor growth, requiring the euthanasia of all animals two weeks post-injection due to acute health complications. Despite this aggressive tumor growth, the model revealed significantly elevated liver weight and liver to body weight ratios in HCC-bearing mice compared to wild type controls. These findings confirm the suitability of the RIL-175 cell line for orthotopic HCC modeling. Nevertheless, further refinement with lower cell counts is needed to extend the experimental timeframe.

Establishing both s.c. and orthotopic RIL-175 models provides supplementary approaches for HCC research. The s.c. model offers ease of measurement and rapid screening capabilities, while the orthotopic model more closely mimics the liver microenvironment, thus, enhancing translational relevance. This dual strategy allows to benefit from each model.

Focusing on PDAC revealed the urgent need to explore the desmoplastic stromal response characteristic of this aggressive cancer type. In pursuit of this goal, subcutaneous injection models were established using four different cell lines: FC1242, FC1245, FC1199, and Hy15549 (Fig. 35).

The usage of cell lines derived from different GEMMs offers valuable insights into PDAC heterogeneity. The Hy15549 cell line, derived from Ptf1-Cre; LSL-KRAS-G12D; p53 Lox/+ mice, and the FC1242, FC1245, and FC1199 cell lines, isolated from K-rasLSL.G12D/+; Trp53R172H/+; Pdx-1-Cre mice, represent different genetic backgrounds. Notably, Ptf1-Cre predominantly targets exocrine and ductal cells, while Pdx1-Cre affects a broader pancreatic cell population, particularly endocrine cells including insulin-producing beta cells. This distinction allows for modeling PDAC arising from different cellular origins. Each cell line was injected into the right flank of C57BL/6 mice at concentrations of 1×10^5 and 1×10^6 cells. Tumor progression was assessed over time, revealing variations in growth patterns among the cell lines.
The FC1245 cell line demonstrated rapid growth and developed tumor ulceration by day 18, even at the lower cell concentration. Under these conditions, it was deemed unsuitable for further investigation due to the short experimental window and the presence of ulceration. Similarly, the FC1199 cell line, while showing promising growth characteristics, was excluded from subsequent experiments due to a high incidence of tumor ulceration. In contrast, both the Hy15549 and FC1242 cell lines demonstrated homogeneous growth patterns without significant ulceration, making them excellent candidates for future experiments. With an optimal experimental duration of 3-4 weeks, these lines enable a comprehensive assessment of therapeutic interventions and stromal interactions.

Finally, to further advance our understanding of the TME, particularly the role of CAFs, a novel mouse model was established (Fig. 36). This model allows the selective CAF depletion, enabling to study their functions and potential as therapeutic targets. This novel mouse strain was created by crossing the Col3a1-CreERT2 strain with the iDTR mouse strain. The resulting offspring carry a *lox*P-flanked STOP cassette upstream of the DTR gene. They also express a tamoxifen-inducible Cre recombinase specifically in CAFs. Upon Tam administration, the Cre recombinase is activated, excising the STOP cassette and enabling DTR expression in CAFs. Subsequent injection of DT selectively depletes these DTR-expressing CAFs. To confirm the successful establishment of the Col3a1-CreERT2/iDTR mouse strain, PCR genotyping was performed on the offspring. The analysis revealed that all mice carried the Cre gene. Both

homozygous and heterozygous mice for the iDTR mutation were identified and are suitable for further breeding to expand the cohorts. By enabling selective CAF depletion, this model allows precise investigation of their role in tumor progression, therapy resistance, and potential as targets for anti-tumor therapies.

In conclusion, the establishment of these diverse murine models for HCC and PDAC research marks a significant advancement in the ability to study these challenging malignancies. The subcutaneous and orthotopic RIL-175 models for HCC provide complementary systems for investigating tumor growth and therapeutic responses. The PDAC models, particularly those utilizing the Hy15549 and FC1242 cell lines, offer valuable tools for studying the desmoplastic stromal response characteristic of pancreatic cancer. Additionally, the development of the Col3a1-CreERT2/iDTR mouse strain enhances the capacity to conduct detailed studies on the role of CAFs in the TME.

Based on my work in this thesis, these models collectively strengthen our ability to conduct preclinical research on HCC and PDAC, potentially accelerating the development of more effective therapeutic strategies for these deadly cancers. By providing diverse platforms for studying tumor biology, drug efficacy, and stromal interactions, these models pave the way for more translational research and the identification of novel therapeutic targets. As we continue to refine and expand upon these models, we anticipate that they will play a crucial role in bridging the gap between basic cancer biology and clinical applications, ultimately leading to improved outcomes for patients suffering from HCC and PDAC.

4.5 Outlook

Building on the insights gained from this thesis, future research in the field of desmoplastic cancers holds promising avenues for exploration. The complex interplay between cancer cells, CAFs, and TAMs revealed in our studies opens up new possibilities for targeted therapies. Future research should focus on:

I. Further investigation into the temporal dynamics of TGF-β signaling and other in part compensatory signaling pathways in CAFs for more precise interventions.
II. Optimization of the rapamycin and Fra-2 ASO combination therapy and exploration of its potential in other cancer types.
III. Utilization of the novel murine models, especially the Col3a1-CreERT2/iDTR strain, for deeper studies of the TME.
IV. Application of advanced techniques like single-cell RNA sequencing for detailed characterization of stromal populations.
V. Development of innovative combination therapies targeting multiple components of the TME
VI. Long-term studies to understand the evolution of the TME over time and in response to therapies.

By continuing to uncover the complexities of desmoplastic cancers, we can move closer to developing personalized treatment approaches in order to improve outcomes for patients with these challenging malignancies.

5 Bibliography

[1] Cancer Today n.d. https://gco.iarc.who.int/today/ (accessed September 5, 2024).

[2] Ernst SM, Mankor JM, Van Riet J, Von Der Thüsen JH, Dubbink HJ, Aerts JGJV, et al. Tobacco Smoking-Related Mutational Signatures in Classifying Smoking-Associated and Nonsmoking-Associated NSCLC. J Thorac Oncol 2023;18:487–98. https://doi.org/10.1016/j.jtho.2022.11.030.

[3] McGlynn KA, London WT. The global epidemiology of hepatocellular carcinoma: present and future. Clin Liver Dis 2011;15:223–43, vii–x. https://doi.org/10.1016/j.cld.2011.03.006.

[4] Barone E, Corrado A, Gemignani F, Landi S. Environmental risk factors for pancreatic cancer: an update. Arch Toxicol 2016;90:2617–42. https://doi.org/10.1007/s00204-016-1821-9.

[5] Ricotti A, Sciannameo V, Balzi W, Roncadori A, Canavese P, Avitabile A, et al. Incidence and Prevalence Analysis of Non-Small-Cell and Small-Cell Lung Cancer Using Administrative Data. Int J Environ Res Public Health 2021;18:9076. https://doi.org/10.3390/ijerph18179076.

[6] Duma N, Santana-Davila R, Molina JR. Non–Small Cell Lung Cancer: Epidemiology, Screening, Diagnosis, and Treatment. Mayo Clin Proc 2019;94:1623–40. https://doi.org/10.1016/j.mayocp.2019.01.013.

[7] Seo J-S, Ju YS, Lee W-C, Shin J-Y, Lee JK, Bleazard T, et al. The transcriptional landscape and mutational profile of lung adenocarcinoma. Genome Res 2012;22:2109–19. https://doi.org/10.1101/gr.145144.112.

[8] Chapman AM, Sun KY, Ruestow P, Cowan DM, Madl AK. Lung cancer mutation profile of EGFR, ALK, and KRAS: Meta-analysis and comparison of never and ever smokers. Lung Cancer Amst Neth 2016;102:122–34. https://doi.org/10.1016/j.lungcan.2016.10.010.

[9] Fois SS, Paliogiannis P, Zinellu A, Fois AG, Cossu A, Palmieri G. Molecular Epidemiology of the Main Druggable Genetic Alterations in Non-Small Cell Lung Cancer. Int J Mol Sci 2021;22:612. https://doi.org/10.3390/ijms22020612.

[10] Kris MG, Gaspar LE, Chaft JE, Kennedy EB, Azzoli CG, Ellis PM, et al. Adjuvant Systemic Therapy and Adjuvant Radiation Therapy for Stage I to IIIA Completely Resected Non-Small-Cell Lung Cancers: American Society of Clinical Oncology/Cancer Care Ontario Clinical Practice Guideline Update. J Clin Oncol Off J Am Soc Clin Oncol 2017;35:2960–74. https://doi.org/10.1200/JCO.2017.72.4401.

[11] Van Schil PE, Balduyck B, De Waele M, Hendriks JM, Hertoghs M, Lauwers P. Surgical treatment of early-stage non-small-cell lung cancer. EJC Suppl EJC Off J EORTC Eur

Organ Res Treat Cancer Al 2013;11:110–22. https://doi.org/10.1016/j.ejcsup.2013.07.021.

[12] Knochelmann HM, Smith AS, Dwyer CJ, Wyatt MM, Mehrotra S, Paulos CM. CAR T Cells in Solid Tumors: Blueprints for Building Effective Therapies. Front Immunol 2018;9:1740. https://doi.org/10.3389/fimmu.2018.01740.

[13] Chmielewski M, Abken H. CAR T cells transform to trucks: chimeric antigen receptor-redirected T cells engineered to deliver inducible IL-12 modulate the tumour stroma to combat cancer. Cancer Immunol Immunother CII 2012;61:1269–77. https://doi.org/10.1007/s00262-012-1202-z.

[14] Fiori ME, Di Franco S, Villanova L, Bianca P, Stassi G, De Maria R. Cancer-associated fibroblasts as abettors of tumor progression at the crossroads of EMT and therapy resistance. Mol Cancer 2019;18:70. https://doi.org/10.1186/s12943-019-0994-2.

[15] Hu H, Piotrowska Z, Hare PJ, Chen H, Mulvey HE, Mayfield A, et al. Three subtypes of lung cancer fibroblasts define distinct therapeutic paradigms. Cancer Cell 2021;39:1531-1547.e10. https://doi.org/10.1016/j.ccell.2021.09.003.

[16] Chen C, Hou J, Yu S, Li W, Wang X, Sun H, et al. Role of cancer-associated fibroblasts in the resistance to antitumor therapy, and their potential therapeutic mechanisms in non-small cell lung cancer. Oncol Lett 2021;21:413. https://doi.org/10.3892/ol.2021.12674.

[17] Joshi RS, Kanugula SS, Sudhir S, Pereira MP, Jain S, Aghi MK. The Role of Cancer-Associated Fibroblasts in Tumor Progression. Cancers 2021;13:1399. https://doi.org/10.3390/cancers13061399.

[18] Liot S, Balas J, Aubert A, Prigent L, Mercier-Gouy P, Verrier B, et al. Stroma Involvement in Pancreatic Ductal Adenocarcinoma: An Overview Focusing on Extracellular Matrix Proteins. Front Immunol 2021;12:612271. https://doi.org/10.3389/fimmu.2021.612271.

[19] Powell EE, Wong VW-S, Rinella M. Non-alcoholic fatty liver disease. Lancet Lond Engl 2021;397:2212–24. https://doi.org/10.1016/S0140-6736(20)32511-3.

[20] Younossi ZM, Golabi P, Paik JM, Henry A, Van Dongen C, Henry L. The global epidemiology of nonalcoholic fatty liver disease (NAFLD) and nonalcoholic steatohepatitis (NASH): a systematic review. Hepatol Baltim Md 2023;77:1335–47. https://doi.org/10.1097/HEP.0000000000000004.

[21] Schuppan D, Surabattula R, Wang XY. Determinants of fibrosis progression and regression in NASH. J Hepatol 2018;68:238–50. https://doi.org/10.1016/j.jhep.2017.11.012.

[22] Younossi ZM, Wong G, Anstee QM, Henry L. The Global Burden of Liver Disease. Clin Gastroenterol Hepatol Off Clin Pract J Am Gastroenterol Assoc 2023;21:1978–91. https://doi.org/10.1016/j.cgh.2023.04.015.

[23] Llovet JM, Ricci S, Mazzaferro V, Hilgard P, Gane E, Blanc J-F, et al. Sorafenib in advanced hepatocellular carcinoma. N Engl J Med 2008;359:378–90. https://doi.org/10.1056/NEJMoa0708857.

[24] Forner A, Reig M, Bruix J. Hepatocellular carcinoma. Lancet Lond Engl 2018;391:1301–14. https://doi.org/10.1016/S0140-6736(18)30010-2.

[25] Villanueva A. Hepatocellular Carcinoma. N Engl J Med 2019;380:1450–62. https://doi.org/10.1056/NEJMra1713263.

[26] Kudo M, Finn RS, Qin S, Han K-H, Ikeda K, Piscaglia F, et al. Lenvatinib versus sorafenib in first-line treatment of patients with unresectable hepatocellular carcinoma: a randomised phase 3 non-inferiority trial. Lancet Lond Engl 2018;391:1163–73. https://doi.org/10.1016/S0140-6736(18)30207-1.

[27] Marrero JA, Kulik LM, Sirlin CB, Zhu AX, Finn RS, Abecassis MM, et al. Diagnosis, Staging, and Management of Hepatocellular Carcinoma: 2018 Practice Guidance by the American Association for the Study of Liver Diseases. Clin Liver Dis 2019;13:1. https://doi.org/10.1002/cld.802.

[28] Kudo M, Ueshima K, Chan S, Minami T, Chishina H, Aoki T, et al. Lenvatinib as an Initial Treatment in Patients with Intermediate-Stage Hepatocellular Carcinoma Beyond Up-To-Seven Criteria and Child-Pugh A Liver Function: A Proof-Of-Concept Study. Cancers 2019;11:1084. https://doi.org/10.3390/cancers11081084.

[29] Bruix J, Qin S, Merle P, Granito A, Huang Y-H, Bodoky G, et al. Regorafenib for patients with hepatocellular carcinoma who progressed on sorafenib treatment (RESORCE): a randomised, double-blind, placebo-controlled, phase 3 trial. The Lancet 2017;389:56–66. https://doi.org/10.1016/S0140-6736(16)32453-9.

[30] Kelley RK, Rimassa L, Cheng A-L, Kaseb A, Qin S, Zhu AX, et al. Cabozantinib plus atezolizumab versus sorafenib for advanced hepatocellular carcinoma (COSMIC-312): a multicentre, open-label, randomised, phase 3 trial. Lancet Oncol 2022;23:995–1008. https://doi.org/10.1016/S1470-2045(22)00326-6.

[31] Zhu AX, Kang Y-K, Yen C-J, Finn RS, Galle PR, Llovet JM, et al. Ramucirumab after sorafenib in patients with advanced hepatocellular carcinoma and increased α-fetoprotein concentrations (REACH-2): a randomised, double-blind, placebo-controlled, phase 3 trial. Lancet Oncol 2019;20:282–96. https://doi.org/10.1016/S1470-2045(18)30937-9.

[32] Finn RS, Qin S, Ikeda M, Galle PR, Ducreux M, Kim T-Y, et al. Atezolizumab plus Bevacizumab in Unresectable Hepatocellular Carcinoma. N Engl J Med 2020;382:1894–905. https://doi.org/10.1056/NEJMoa1915745.

[33] Angel P, Imagawa M, Chiu R, Stein B, Imbra RJ, Rahmsdorf HJ, et al. Phorbol ester-inducible genes contain a common cis element recognized by a TPA-modulated trans-acting factor. Cell 1987;49:729–39. https://doi.org/10.1016/0092-8674(87)90611-8.

[34] Kudo M, Okusaka T, Motomura K, Ohno I, Morimoto M, Seo S, et al. Ramucirumab after prior sorafenib in patients with advanced hepatocellular carcinoma and elevated alpha-fetoprotein: Japanese subgroup analysis of the REACH-2 trial. J Gastroenterol 2020;55:627–39. https://doi.org/10.1007/s00535-020-01668-w.

[35] Finn RS, Ryoo B-Y, Merle P, Kudo M, Bouattour M, Lim HY, et al. Pembrolizumab As Second-Line Therapy in Patients With Advanced Hepatocellular Carcinoma in KEYNOTE-240: A Randomized, Double-Blind, Phase III Trial. J Clin Oncol Off J Am Soc Clin Oncol 2020;38:193–202. https://doi.org/10.1200/JCO.19.01307.

[36] Abou-Alfa GK, Meyer T, Cheng A-L, El-Khoueiry AB, Rimassa L, Ryoo B-Y, et al. Cabozantinib in Patients with Advanced and Progressing Hepatocellular Carcinoma. N Engl J Med 2018;379:54–63. https://doi.org/10.1056/NEJMoa1717002.

[37] Siegel RL, Miller KD, Jemal A. Cancer statistics, 2020. CA Cancer J Clin 2020;70:7–30. https://doi.org/10.3322/caac.21590.

[38] Llovet JM, Kelley RK, Villanueva A, Singal AG, Pikarsky E, Roayaie S, et al. Hepatocellular carcinoma. Nat Rev Dis Primer 2021;7:1–28. https://doi.org/10.1038/s41572-020-00240-3.

[39] Siegel RL, Miller KD, Fuchs HE, Jemal A. Cancer statistics, 2022. CA Cancer J Clin 2022;72:7–33. https://doi.org/10.3322/caac.21708.

[40] Friedlander SYG, Chu GC, Snyder EL, Girnius N, Dibelius G, Crowley D, et al. Context-Dependent Transformation of Adult Pancreatic Cells by Oncogenic K-Ras. Cancer Cell 2009;16:379–89. https://doi.org/10.1016/j.ccr.2009.09.027.

[41] Kopp JL, von Figura G, Mayes E, Liu F-F, Dubois CL, Morris JP, et al. Identification of Sox9-dependent acinar-to-ductal reprogramming as the principal mechanism for initiation of pancreatic ductal adenocarcinoma. Cancer Cell 2012;22:737–50. https://doi.org/10.1016/j.ccr.2012.10.025.

[42] Cox AD, Fesik SW, Kimmelman AC, Luo J, Der CJ. Drugging the undruggable RAS: Mission possible? Nat Rev Drug Discov 2014;13:828–51. https://doi.org/10.1038/nrd4389.

[43] Bailey P, Chang DK, Nones K, Johns AL, Patch A-M, Gingras M-C, et al. Genomic analyses identify molecular subtypes of pancreatic cancer. Nature 2016;531:47–52. https://doi.org/10.1038/nature16965.

[44] Mueller S, Engleitner T, Maresch R, Zukowska M, Lange S, Kaltenbacher T, et al. Evolutionary routes and KRAS dosage define pancreatic cancer phenotypes. Nature 2018;554:62–8. https://doi.org/10.1038/nature25459.

[45] Orth M, Metzger P, Gerum S, Mayerle J, Schneider G, Belka C, et al. Pancreatic ductal adenocarcinoma: biological hallmarks, current status, and future perspectives of combined modality treatment approaches. Radiat Oncol 2019;14:141. https://doi.org/10.1186/s13014-019-1345-6.

[46] Maitra A, Hruban RH. Pancreatic cancer. Annu Rev Pathol 2008;3:157–88. https://doi.org/10.1146/annurev.pathmechdis.3.121806.154305.

[47] Ryan DP, Hong TS, Bardeesy N. Pancreatic adenocarcinoma. N Engl J Med 2014;371:1039–49. https://doi.org/10.1056/NEJMra1404198.

[48] Conroy T, Desseigne F, Ychou M, Bouché O, Guimbaud R, Bécouarn Y, et al. FOLFIRINOX versus gemcitabine for metastatic pancreatic cancer. N Engl J Med 2011;364:1817–25. https://doi.org/10.1056/NEJMoa1011923.

[49] Von Hoff DD, Ervin T, Arena FP, Chiorean EG, Infante J, Moore M, et al. Increased Survival in Pancreatic Cancer with nab-Paclitaxel plus Gemcitabine. N Engl J Med 2013;369:1691–703. https://doi.org/10.1056/NEJMoa1304369.

[50] Hall WA, Goodman KA. Radiation therapy for pancreatic adenocarcinoma, a treatment option that must be considered in the management of a devastating malignancy. Radiat Oncol 2019;14:114. https://doi.org/10.1186/s13014-019-1277-1.

[51] Roeder F. Neoadjuvant radiotherapeutic strategies in pancreatic cancer. World J Gastrointest Oncol 2016;8:186–97. https://doi.org/10.4251/wjgo.v8.i2.186.

[52] Ribas A, Wolchok JD. Cancer immunotherapy using checkpoint blockade. Science 2018;359:1350–5. https://doi.org/10.1126/science.aar4060.

[53] Garon EB, Rizvi NA, Hui R, Leighl N, Balmanoukian AS, Eder JP, et al. Pembrolizumab for the treatment of non-small-cell lung cancer. N Engl J Med 2015;372:2018–28. https://doi.org/10.1056/NEJMoa1501824.

[54] Le DT, Durham JN, Smith KN, Wang H, Bartlett BR, Aulakh LK, et al. Mismatch-repair deficiency predicts response of solid tumors to PD-1 blockade. Science 2017;357:409–13. https://doi.org/10.1126/science.aan6733.

[55] Zhao P, Li L, Jiang X, Li Q. Mismatch repair deficiency/microsatellite instability-high as a predictor for anti-PD-1/PD-L1 immunotherapy efficacy. J Hematol OncolJ Hematol Oncol 2019;12:54. https://doi.org/10.1186/s13045-019-0738-1.

[56] Quail DF, Joyce JA. Microenvironmental regulation of tumor progression and metastasis. Nat Med 2013;19:1423–37. https://doi.org/10.1038/nm.3394.

[57] Walker C, Mojares E, Del Río Hernández A. Role of Extracellular Matrix in Development and Cancer Progression. Int J Mol Sci 2018;19:3028. https://doi.org/10.3390/ijms19103028.

[58] Hinz B, Phan SH, Thannickal VJ, Galli A, Bochaton-Piallat M-L, Gabbiani G. The Myofibroblast: One Function, Multiple Origins. Am J Pathol 2007;170:1807–16. https://doi.org/10.2353/ajpath.2007.070112.

[59] Kalluri R, Zeisberg M. Fibroblasts in cancer. Nat Rev Cancer 2006;6:392–401. https://doi.org/10.1038/nrc1877.

[60] Biffi G, Tuveson DA. Diversity and Biology of Cancer-Associated Fibroblasts. Physiol Rev 2021;101:147–76. https://doi.org/10.1152/physrev.00048.2019.

[61] Moretti L, Stalfort J, Barker TH, Abebayehu D. The interplay of fibroblasts, the extracellular matrix, and inflammation in scar formation. J Biol Chem 2022;298:101530. https://doi.org/10.1016/j.jbc.2021.101530.

[62] Kochetkova M, Samuel MS. Differentiation of the tumor microenvironment: are CAFs the Organizer? Trends Cell Biol 2022;32:285–94. https://doi.org/10.1016/j.tcb.2021.11.008.

[63] Sahai E, Astsaturov I, Cukierman E, DeNardo DG, Egeblad M, Evans RM, et al. A framework for advancing our understanding of cancer-associated fibroblasts. Nat Rev Cancer 2020;20:174–86. https://doi.org/10.1038/s41568-019-0238-1.

[64] Fiori ME, Di Franco S, Villanova L, Bianca P, Stassi G, De Maria R. Cancer-associated fibroblasts as abettors of tumor progression at the crossroads of EMT and therapy resistance. Mol Cancer 2019;18:70. https://doi.org/10.1186/s12943-019-0994-2.

[65] Orimo A, Gupta PB, Sgroi DC, Arenzana-Seisdedos F, Delaunay T, Naeem R, et al. Stromal Fibroblasts Present in Invasive Human Breast Carcinomas Promote Tumor Growth and Angiogenesis through Elevated SDF-1/CXCL12 Secretion. Cell 2005;121:335–48. https://doi.org/10.1016/j.cell.2005.02.034.

[66] Pietras K, Pahler J, Bergers G, Hanahan D. Functions of Paracrine PDGF Signaling in the Proangiogenic Tumor Stroma Revealed by Pharmacological Targeting. PLOS Med 2008;5:e19. https://doi.org/10.1371/journal.pmed.0050019.

[67] Liu L, Liu L, Yao HH, Zhu ZQ, Ning ZL, Huang Q. Stromal Myofibroblasts Are Associated with Poor Prognosis in Solid Cancers: A Meta-Analysis of Published Studies. PLOS ONE 2016;11:e0159947. https://doi.org/10.1371/journal.pone.0159947.

[68] Özdemir BC, Pentcheva-Hoang T, Carstens JL, Zheng X, Wu C-C, Simpson TR, et al. Depletion of carcinoma-associated fibroblasts and fibrosis induces immunosuppression and accelerates pancreas cancer with reduced survival. Cancer Cell 2014;25:719–34. https://doi.org/10.1016/j.ccr.2014.04.005.

[69] Miyai Y, Esaki N, Takahashi M, Enomoto A. Cancer-associated fibroblasts that restrain cancer progression: Hypotheses and perspectives. Cancer Sci 2020;111:1047–57. https://doi.org/10.1111/cas.14346.

[70] Calon A, Lonardo E, Berenguer-Llergo A, Espinet E, Hernando-Momblona X, Iglesias M, et al. Stromal gene expression defines poor-prognosis subtypes in colorectal cancer. Nat Genet 2015;47:320–9. https://doi.org/10.1038/ng.3225.

[71] Gabrilovich DI. Myeloid-Derived Suppressor Cells. Cancer Immunol Res 2017;5:3–8. https://doi.org/10.1158/2326-6066.CIR-16-0297.

[72] Tanaka A, Sakaguchi S. Regulatory T cells in cancer immunotherapy. Cell Res 2017;27:109–18. https://doi.org/10.1038/cr.2016.151.

[73] Mariathasan S, Turley SJ, Nickles D, Castiglioni A, Yuen K, Wang Y, et al. TGFβ attenuates tumour response to PD-L1 blockade by contributing to exclusion of T cells. Nature 2018;554:544–8. https://doi.org/10.1038/nature25501.

[74] DeNardo DG, Ruffell B. Macrophages as regulators of tumour immunity and immunotherapy. Nat Rev Immunol 2019;19:369–82. https://doi.org/10.1038/s41577-019-0127-6.

[75] Vitale I, Manic G, Coussens LM, Kroemer G, Galluzzi L. Macrophages and Metabolism in the Tumor Microenvironment. Cell Metab 2019;30:36–50. https://doi.org/10.1016/j.cmet.2019.06.001.

[76] Hu H, Hang J-J, Han T, Zhuo M, Jiao F, Wang L-W. The M2 phenotype of tumor-associated macrophages in the stroma confers a poor prognosis in pancreatic cancer. Tumour Biol J Int Soc Oncodevelopmental Biol Med 2016;37:8657–64. https://doi.org/10.1007/s13277-015-4741-z.

[77] Yamaguchi T, Fushida S, Yamamoto Y, Tsukada T, Kinoshita J, Oyama K, et al. Tumor-associated macrophages of the M2 phenotype contribute to progression in gastric cancer with peritoneal dissemination. Gastric Cancer 2016;19:1052–65. https://doi.org/10.1007/s10120-015-0579-8.

[78] Cortese N, Carriero R, Laghi L, Mantovani A, Marchesi F. Prognostic significance of tumor-associated macrophages: past, present and future. Semin Immunol 2020;48:101408. https://doi.org/10.1016/j.smim.2020.101408.

[79] Ping Q, Yan R, Cheng X, Wang W, Zhong Y, Hou Z, et al. Cancer-associated fibroblasts: overview, progress, challenges, and directions. Cancer Gene Ther 2021;28:984–99. https://doi.org/10.1038/s41417-021-00318-4.

[80] Kuzet S-E, Gaggioli C. Fibroblast activation in cancer: when seed fertilizes soil. Cell Tissue Res 2016;365:607–19. https://doi.org/10.1007/s00441-016-2467-x.

[81] Zhang W, Bouchard G, Yu A, Shafiq M, Jamali M, Shrager JB, et al. GFPT2-Expressing Cancer-Associated Fibroblasts Mediate Metabolic Reprogramming in Human Lung Adenocarcinoma. Cancer Res 2018;78:3445–57. https://doi.org/10.1158/0008-5472.CAN-17-2928.

[82] Bu L, Baba H, Yoshida N, Miyake K, Yasuda T, Uchihara T, et al. Biological heterogeneity and versatility of cancer-associated fibroblasts in the tumor microenvironment. Oncogene 2019;38:4887–901. https://doi.org/10.1038/s41388-019-0765-y.

[83] Kalluri R. The biology and function of fibroblasts in cancer. Nat Rev Cancer 2016;16:582–98. https://doi.org/10.1038/nrc.2016.73.

[84] Louault K, Li R-R, DeClerck YA. Cancer-Associated Fibroblasts: Understanding Their Heterogeneity. Cancers 2020;12:3108. https://doi.org/10.3390/cancers12113108.

[85] Hawinkels LJ a. C, Paauwe M, Verspaget HW, Wiercinska E, van der Zon JM, van der Ploeg K, et al. Interaction with colon cancer cells hyperactivates TGF-β signaling in cancer-associated fibroblasts. Oncogene 2014;33:97–107. https://doi.org/10.1038/onc.2012.536.

[86] Wu X, Chen X, Zhou Q, Li P, Yu B, Li J, et al. Hepatocyte growth factor activates tumor stromal fibroblasts to promote tumorigenesis in gastric cancer. Cancer Lett 2013;335:128–35. https://doi.org/10.1016/j.canlet.2013.02.002.

[87] Kojima Y, Acar A, Eaton EN, Mellody KT, Scheel C, Ben-Porath I, et al. Autocrine TGF-beta and stromal cell-derived factor-1 (SDF-1) signaling drives the evolution of tumor-promoting mammary stromal myofibroblasts. Proc Natl Acad Sci U S A 2010;107:20009–14. https://doi.org/10.1073/pnas.1013805107.

[88] Omary MB, Lugea A, Lowe AW, Pandol SJ. The pancreatic stellate cell: a star on the rise in pancreatic diseases. J Clin Invest 2007;117:50–9. https://doi.org/10.1172/JCI30082.

[89] Yin C, Evason KJ, Asahina K, Stainier DYR. Hepatic stellate cells in liver development, regeneration, and cancer. J Clin Invest 2013;123:1902–10. https://doi.org/10.1172/JCI66369.

[90] Mishra PJ, Mishra PJ, Humeniuk R, Medina DJ, Alexe G, Mesirov JP, et al. Carcinoma-associated fibroblast-like differentiation of human mesenchymal stem cells. Cancer Res 2008;68:4331–9. https://doi.org/10.1158/0008-5472.CAN-08-0943.

[91] Quante M, Tu SP, Tomita H, Gonda T, Wang SSW, Takashi S, et al. Bone marrow-derived myofibroblasts contribute to the mesenchymal stem cell niche and promote tumor growth. Cancer Cell 2011;19:257–72. https://doi.org/10.1016/j.ccr.2011.01.020.

[92] Jotzu C, Alt E, Welte G, Li J, Hennessy BT, Devarajan E, et al. Adipose tissue-derived stem cells differentiate into carcinoma-associated fibroblast-like cells under the influence of tumor-derived factors. Anal Cell Pathol Amst 2010;33:61–79. https://doi.org/10.3233/ACP-CLO-2010-0535.

[93] Bochet L, Lehuédé C, Dauvillier S, Wang YY, Dirat B, Laurent V, et al. Adipocyte-derived fibroblasts promote tumor progression and contribute to the desmoplastic reaction in breast cancer. Cancer Res 2013;73:5657–68. https://doi.org/10.1158/0008-5472.CAN-13-0530.

[94] Rhim AD, Mirek ET, Aiello NM, Maitra A, Bailey JM, McAllister F, et al. EMT and dissemination precede pancreatic tumor formation. Cell 2012;148:349–61. https://doi.org/10.1016/j.cell.2011.11.025.

[95] Potenta S, Zeisberg E, Kalluri R. The role of endothelial-to-mesenchymal transition in cancer progression. Br J Cancer 2008;99:1375–9. https://doi.org/10.1038/sj.bjc.6604662.

[96] Huang X, He C, Hua X, Kan A, Mao Y, Sun S, et al. Oxidative stress induces monocyte-to-myofibroblast transdifferentiation through p38 in pancreatic ductal adenocarcinoma. Clin Transl Med 2020;10:e41. https://doi.org/10.1002/ctm2.41.

[97] Dulauroy S, Di Carlo SE, Langa F, Eberl G, Peduto L. Lineage tracing and genetic ablation of ADAM12(+) perivascular cells identify a major source of profibrotic cells during acute tissue injury. Nat Med 2012;18:1262–70. https://doi.org/10.1038/nm.2848.

[98] Rinkevich Y, Mori T, Sahoo D, Xu P-X, Bermingham JR, Weissman IL. Identification and prospective isolation of a mesothelial precursor lineage giving rise to smooth muscle cells and fibroblasts for mammalian internal organs, and their vasculature. Nat Cell Biol 2012;14:1251–60. https://doi.org/10.1038/ncb2610.

[99] Dzobo K, Senthebane D, Dandara C. The Tumor Microenvironment in Tumorigenesis and Therapy Resistance Revisited. Cancers 2023;15:376. https://doi.org/10.3390/cancers15020376.

[100] Massagué J, Sheppard D. TGF-β signaling in health and disease. Cell 2023;186:4007–37. https://doi.org/10.1016/j.cell.2023.07.036.

[101] Nixon BG, Gao S, Wang X, Li MO. TGFβ control of immune responses in cancer: a holistic immuno-oncology perspective. Nat Rev Immunol 2023;23:346–62. https://doi.org/10.1038/s41577-022-00796-z.

[102] Heldin C-H, Moustakas A. Signaling Receptors for TGF-β Family Members. Cold Spring Harb Perspect Biol 2016;8:a022053. https://doi.org/10.1101/cshperspect.a022053.

[103] Zhang W, Jiang Y, Wang Q, Ma X, Xiao Z, Zuo W, et al. Single-molecule imaging reveals transforming growth factor-beta-induced type II receptor dimerization. Proc Natl Acad Sci U S A 2009;106:15679–83. https://doi.org/10.1073/pnas.0908279106.

[104] Shi Y, Hata A, Lo RS, Massagué J, Pavletich NP. A structural basis for mutational inactivation of the tumour suppressor Smad4. Nature 1997;388:87–93. https://doi.org/10.1038/40431.

[105] Massagué J. TGFβ signalling in context. Nat Rev Mol Cell Biol 2012;13:616–30. https://doi.org/10.1038/nrm3434.

[106] Derynck R, Budi EH. Specificity, versatility, and control of TGF-β family signaling. Sci Signal 2019;12:eaav5183. https://doi.org/10.1126/scisignal.aav5183.

[107] Hill CS. Transcriptional Control by the SMADs. Cold Spring Harb Perspect Biol 2016;8:a022079. https://doi.org/10.1101/cshperspect.a022079.

[108] Lee MK, Pardoux C, Hall MC, Lee PS, Warburton D, Qing J, et al. TGF-beta activates Erk MAP kinase signalling through direct phosphorylation of ShcA. EMBO J 2007;26:3957–67. https://doi.org/10.1038/sj.emboj.7601818.

[109] Moustakas A, Heldin C-H. Mechanisms of TGFβ-Induced Epithelial–Mesenchymal Transition. J Clin Med 2016;5:63. https://doi.org/10.3390/jcm5070063.

[110] Wculek SK, Dunphy G, Heras-Murillo I, Mastrangelo A, Sancho D. Metabolism of tissue macrophages in homeostasis and pathology. Cell Mol Immunol 2022;19:384–408. https://doi.org/10.1038/s41423-021-00791-9.

[111] Westman J, Grinstein S, Marques PE. Phagocytosis of Necrotic Debris at Sites of Injury and Inflammation. Front Immunol 2019;10:3030. https://doi.org/10.3389/fimmu.2019.03030.

[112] Gordon S, Plüddemann A. Macrophage Clearance of Apoptotic Cells: A Critical Assessment. Front Immunol 2018;9:127. https://doi.org/10.3389/fimmu.2018.00127.

[113] Kawasaki T, Kawai T. Toll-like receptor signaling pathways. Front Immunol 2014;5:461. https://doi.org/10.3389/fimmu.2014.00461.

[114] Takeuchi O, Akira S. Pattern recognition receptors and inflammation. Cell 2010;140:805–20. https://doi.org/10.1016/j.cell.2010.01.022.

[115] Medzhitov R. Recognition of microorganisms and activation of the immune response. Nature 2007;449:819–26. https://doi.org/10.1038/nature06246.

[116] Newton K, Dixit VM. Signaling in innate immunity and inflammation. Cold Spring Harb Perspect Biol 2012;4:a006049. https://doi.org/10.1101/cshperspect.a006049.

[117] Nathan CF, Murray HW, Wiebe ME, Rubin BY. Identification of interferon-gamma as the lymphokine that activates human macrophage oxidative metabolism and antimicrobial activity. J Exp Med 1983;158:670–89. https://doi.org/10.1084/jem.158.3.670.

[118] Mills CD, Kincaid K, Alt JM, Heilman MJ, Hill AM. M-1/M-2 macrophages and the Th1/Th2 paradigm. J Immunol Baltim Md 1950 2000;164:6166–73. https://doi.org/10.4049/jimmunol.164.12.6166.

[119] Orecchioni M, Ghosheh Y, Pramod AB, Ley K. Macrophage Polarization: Different Gene Signatures in M1(LPS+) vs. Classically and M2(LPS–) vs. Alternatively Activated Macrophages. Front Immunol 2019;10:1084. https://doi.org/10.3389/fimmu.2019.01084.

[120] Rőszer T. Understanding the Mysterious M2 Macrophage through Activation Markers and Effector Mechanisms. Mediators Inflamm 2015;2015:816460. https://doi.org/10.1155/2015/816460.

[121] Fuchs AL, Costello SM, Schiller SM, Tripet BP, Copié V. Primary Human M2 Macrophage Subtypes Are Distinguishable by Aqueous Metabolite Profiles. Int J Mol Sci 2024;25:2407. https://doi.org/10.3390/ijms25042407.

[122] Kuznetsova AB, Kolesova EP, Parodi A, Zamyatnin AA, Egorova VS. Reprogramming Tumor-Associated Macrophage Using Nanocarriers: New Perspectives to Halt Cancer Progression. Pharmaceutics 2024;16:636. https://doi.org/10.3390/pharmaceutics16050636.

[123] Eferl R, Wagner EF. AP-1: a double-edged sword in tumorigenesis. Nat Rev Cancer 2003;3:859–68. https://doi.org/10.1038/nrc1209.

[124] Glover JN, Harrison SC. Crystal structure of the heterodimeric bZIP transcription factor c-Fos-c-Jun bound to DNA. Nature 1995;373:257–61. https://doi.org/10.1038/373257a0.

[125] Halazonetis TD, Georgopoulos K, Greenberg ME, Leder P. c-Jun dimerizes with itself and with c-Fos, forming complexes of different DNA binding affinities. Cell 1988;55:917–24. https://doi.org/10.1016/0092-8674(88)90147-x.

[126] Tulchinsky E. Fos family members: regulation, structure and role in oncogenic transformation. Histol Histopathol 2000;15:921–8. https://doi.org/10.14670/HH-15.921.

[127] Birnhuber A, Biasin V, Schnoegl D, Marsh LM, Kwapiszewska G. Transcription factor Fra-2 and its emerging role in matrix deposition, proliferation and inflammation in chronic lung diseases. Cell Signal 2019;64:109408. https://doi.org/10.1016/j.cellsig.2019.109408.

[128] Artlett CM. The IL-1 family of cytokines. Do they have a role in scleroderma fibrosis? Immunol Lett 2018;195:30–7. https://doi.org/10.1016/j.imlet.2017.11.012.

[129] Sahin H, Wasmuth HE. Chemokines in tissue fibrosis. Biochim Biophys Acta BBA - Mol Basis Dis 2013;1832:1041–8. https://doi.org/10.1016/j.bbadis.2012.11.004.

[130] Stephenson ML, Zamecnik PC. Inhibition of Rous sarcoma viral RNA translation by a specific oligodeoxyribonucleotide. Proc Natl Acad Sci U S A 1978;75:285. https://doi.org/10.1073/pnas.75.1.285.

[131] Bennett CF, Swayze EE. RNA Targeting Therapeutics: Molecular Mechanisms of Antisense Oligonucleotides as a Therapeutic Platform. Annu Rev Pharmacol Toxicol 2010;50:259–93. https://doi.org/10.1146/annurev.pharmtox.010909.105654.

[132] Kole R, Krainer AR, Altman S. RNA therapeutics: beyond RNA interference and antisense oligonucleotides. Nat Rev Drug Discov 2012;11:125–40. https://doi.org/10.1038/nrd3625.

[133] Bennett CF, Baker BF, Pham N, Swayze E, Geary RS. Pharmacology of Antisense Drugs. Annu Rev Pharmacol Toxicol 2017;57:81–105. https://doi.org/10.1146/annurev-pharmtox-010716-104846.

[134] Lieberman J. Tapping the RNA world for therapeutics. Nat Struct Mol Biol 2018;25:357–64. https://doi.org/10.1038/s41594-018-0054-4.

[135] Havens MA, Hastings ML. Splice-switching antisense oligonucleotides as therapeutic drugs. Nucleic Acids Res 2016;44:6549–63. https://doi.org/10.1093/nar/gkw533.

[136] Disterer P, Al-Shawi R, Ellmerich S, Waddington SN, Owen JS, Simons JP, et al. Exon Skipping of Hepatic APOB Pre-mRNA With Splice-switching Oligonucleotides Reduces LDL Cholesterol In Vivo. Mol Ther 2013;21:602–9. https://doi.org/10.1038/mt.2012.264.

[137] Siva K, Covello G, Denti MA. Exon-skipping antisense oligonucleotides to correct missplicing in neurogenetic diseases. Nucleic Acid Ther 2014;24:69–86. https://doi.org/10.1089/nat.2013.0461.

[138] Scotti MM, Swanson MS. RNA mis-splicing in disease. Nat Rev Genet 2016;17:19–32. https://doi.org/10.1038/nrg.2015.3.

[139] Geary RS, Norris D, Yu R, Bennett CF. Pharmacokinetics, biodistribution and cell uptake of antisense oligonucleotides. Adv Drug Deliv Rev 2015;87:46–51. https://doi.org/10.1016/j.addr.2015.01.008.

[140] Crooke ST, Witztum JL, Bennett CF, Baker BF. RNA-Targeted Therapeutics. Cell Metab 2018;27:714–39. https://doi.org/10.1016/j.cmet.2018.03.004.

[141] Liao H, Wang S, Wang X, Dai DZ, Zhang Y, Zhu C, et al. Imaging-Assisted Antisense Oligonucleotide Delivery for Tumor-Targeted Gene Therapy. Chem Biomed Imaging 2024;2:313–30. https://doi.org/10.1021/cbmi.4c00012.

[142] Laplante M, Sabatini DM. mTOR signaling in growth control and disease. Cell 2012;149:274–93. https://doi.org/10.1016/j.cell.2012.03.017.

[143] Faivre S, Kroemer G, Raymond E. Current development of mTOR inhibitors as anticancer agents. Nat Rev Drug Discov 2006;5:671–88. https://doi.org/10.1038/nrd2062.

[144] Zhao Y, Liu Y, Zhou L, Du G-S, He Q. Trends of rapamycin in survival benefits of liver transplantation for hepatocellular carcinoma. World J Gastrointest Surg 2021;13:953–66. https://doi.org/10.4240/wjgs.v13.i9.953.

[145] Sarbassov DD, Ali SM, Sengupta S, Sheen J-H, Hsu PP, Bagley AF, et al. Prolonged rapamycin treatment inhibits mTORC2 assembly and Akt/PKB. Mol Cell 2006;22:159–68. https://doi.org/10.1016/j.molcel.2006.03.029.

[146] Li J, Kim SG, Blenis J. Rapamycin: one drug, many effects. Cell Metab 2014;19:373–9. https://doi.org/10.1016/j.cmet.2014.01.001.

[147] Hasskarl J. Everolimus. Recent Results Cancer Res Fortschritte Krebsforsch Progres Dans Rech Sur Cancer 2014;201:373–92. https://doi.org/10.1007/978-3-642-54490-3_23.

[148] Hudes G, Carducci M, Tomczak P, Dutcher J, Figlin R, Kapoor A, et al. Temsirolimus, Interferon Alfa, or Both for Advanced Renal-Cell Carcinoma. N Engl J Med 2007;356:2271–81. https://doi.org/10.1056/NEJMoa066838.

[149] Pópulo H, Lopes JM, Soares P. The mTOR Signalling Pathway in Human Cancer. Int J Mol Sci 2012;13:1886–918. https://doi.org/10.3390/ijms13021886.

[150] Aslam Jr M, Khan Jr MA, Qureshi MA, Celik S, Senkowski Jr MS, Weng SY, et al. Rapamycin Promotes Tumoricidal Immunity in Murine HCC Via M1-Type Macrophage and Dendritic Cell Polarization and Enhancement of Cytotoxic T Cells. HEPATOLOGY, vol. 68, WILEY 111 RIVER ST, HOBOKEN 07030-5774, NJ USA; 2018, p. 204A-204A.

[151] Saul MC, Philip VM, Reinholdt LG, Chesler EJ. High-Diversity Mouse Populations for Complex Traits. Trends Genet 2019;35:501–14. https://doi.org/10.1016/j.tig.2019.04.003.

[152] Breschi A, Gingeras TR, Guigó R. Comparative transcriptomics in human and mouse. Nat Rev Genet 2017;18:425–40. https://doi.org/10.1038/nrg.2017.19.

[153] Fernandez JL, Årbogen S, Sadeghinia MJ, Haram M, Snipstad S, Torp SH, et al. A Comparative Analysis of Orthotopic and Subcutaneous Pancreatic Tumour Models: Tumour Microenvironment and Drug Delivery. Cancers 2023;15:5415. https://doi.org/10.3390/cancers15225415.

[154] Stribbling SM, Beach C, Ryan AJ. Orthotopic and metastatic tumour models in preclinical cancer research. Pharmacol Ther 2024;257:108631. https://doi.org/10.1016/j.pharmthera.2024.108631.

[155] Ray MK, Fagan SP, Brunicardi FC. The Cre–loxP System: A Versatile Tool for Targeting Genes in a Cell- and Stage-Specific Manner. Cell Transplant 2000;9:805–15. https://doi.org/10.1177/096368970000900607.

[156] Kim H, Kim M, Im S-K, Fang S. Mouse Cre-LoxP system: general principles to determine tissue-specific roles of target genes. Lab Anim Res 2018;34:147–59. https://doi.org/10.5625/lar.2018.34.4.147.

[157] Rosigkeit S, Kruchem M, Thies D, Kreft A, Eichler E, Boegel S, et al. Definitive evidence for Club cells as progenitors for mutant Kras/Trp53-deficient lung cancer. Int J Cancer 2021;149:1670–82. https://doi.org/10.1002/ijc.33756.

[158] Erstad DJ, Sojoodi M, Taylor MS, Ghoshal S, Razavi AA, Graham-O'Regan KA, et al. Orthotopic and heterotopic murine models of pancreatic cancer and their different responses to FOLFIRINOX chemotherapy. Dis Model Mech 2018;11:dmm034793. https://doi.org/10.1242/dmm.034793.

[159] Siegl D, Kruchem M, Jansky S, Eichler E, Thies D, Hartwig U, et al. A PCR protocol to establish standards for routine mycoplasma testing that by design detects over ninety percent of all known mycoplasma species. iScience 2023;26:106724. https://doi.org/10.1016/j.isci.2023.106724.

[160] Molokanova O, Schönig K, Weng S-Y, Wang X, Ohngemach S, Nikolaev A, et al. Inducible ablation of TGFß receptor type 2 limited to hepatic stellate cells potently inhibits liver fibrosis and attenuates inflamation. J Hepatol 2018;68:S391.

[161] Buenrostro D, Kwakwa KA, Putnam NE, Merkel AR, Johnson JR, Cassat JE, et al. Early TGF-β inhibition in mice reduces the incidence of breast cancer induced bone disease in a myeloid dependent manner. Bone 2018;113:77–88. https://doi.org/10.1016/j.bone.2018.05.008.

[162] Khalil H, Kanisicak O, Prasad V, Correll RN, Fu X, Schips T, et al. Fibroblast-specific TGF-β–Smad2/3 signaling underlies cardiac fibrosis. J Clin Invest n.d.;127:3770–83. https://doi.org/10.1172/JCI94753.

[163] Mu X, Pradere J-P, Affò S, Dapito DH, Friedman R, Lefkovitch JH, et al. Epithelial Transforming Growth Factor-β Signaling Does Not Contribute to Liver Fibrosis but Protects Mice From Cholangiocarcinoma. Gastroenterology 2016;150:720–33. https://doi.org/10.1053/j.gastro.2015.11.039.

[164] Somanader DVN, Zhao P, Widdop RE, Samuel CS. The involvement of the Wnt/β-catenin signaling cascade in fibrosis progression and its therapeutic targeting by relaxin. Biochem Pharmacol 2024;223:116130. https://doi.org/10.1016/j.bcp.2024.116130.

[165] Yoshida S, Kornek M, Ikenaga N, Schmelzle M, Masuzaki R, Csizmadia E, et al. Sublethal heat treatment promotes epithelial-mesenchymal transition and enhances the malignant potential of hepatocellular carcinoma. Hepatology 2013;58:1667. https://doi.org/10.1002/hep.26526.

[166] Chen Y, Yang S, Tavormina J, Tampe D, Zeisberg M, Wang H, et al. Oncogenic collagen I homotrimers from cancer cells bind to α3β1 integrin and impact tumor microbiome and immunity to promote pancreatic cancer. Cancer Cell 2022;40:818-834.e9. https://doi.org/10.1016/j.ccell.2022.06.011.

[167] Junttila MR, de Sauvage FJ. Influence of tumour micro-environment heterogeneity on therapeutic response. Nature 2013;501:346–54. https://doi.org/10.1038/nature12626.

[168] Greaves M, Maley CC. CLONAL EVOLUTION IN CANCER. Nature 2012;481:306–13. https://doi.org/10.1038/nature10762.

[169] Janssen LME, Ramsay EE, Logsdon CD, Overwijk WW. The immune system in cancer metastasis: friend or foe? J Immunother Cancer 2017;5:79. https://doi.org/10.1186/s40425-017-0283-9.

[170] Langley RR, Fidler IJ. The seed and soil hypothesis revisited - the role of tumor-stroma interactions in metastasis to different organs. Int J Cancer J Int Cancer 2011;128:2527–35. https://doi.org/10.1002/ijc.26031.

[171] Folkman J. Tumor Angiogenesis: Therapeutic Implications. N Engl J Med 1971;285:1182–6. https://doi.org/10.1056/NEJM197111182852108.

[172] Northey JJ, Przybyla L, Weaver VM. Tissue force programs cell fate and tumor aggression. Cancer Discov 2017;7:1224–37. https://doi.org/10.1158/2159-8290.CD-16-0733.

[173] Feig C, Jones JO, Kraman M, Wells RJB, Deonarine A, Chan DS, et al. Targeting CXCL12 from FAP-expressing carcinoma-associated fibroblasts synergizes with anti–PD-L1 immunotherapy in pancreatic cancer. Proc Natl Acad Sci U S A 2013;110:20212–7. https://doi.org/10.1073/pnas.1320318110.

[174] Mohr A, Atif M, Balderas R, Gorochov G, Miyara M. The role of FOXP3+ regulatory T cells in human autoimmune and inflammatory diseases. Clin Exp Immunol 2019;197:24–35. https://doi.org/10.1111/cei.13288.

[175] Satelli A, Li S. Vimentin in cancer and its potential as a molecular target for cancer therapy. Cell Mol Life Sci CMLS 2011;68:3033–46. https://doi.org/10.1007/s00018-011-0735-1.

[176] Eferl R, Hasselblatt P, Rath M, Popper H, Zenz R, Komnenovic V, et al. Development of pulmonary fibrosis through a pathway involving the transcription factor Fra-2/AP-1. Proc Natl Acad Sci U S A 2008;105:10525–30. https://doi.org/10.1073/pnas.0801414105.

[177] Milde-Langosch K, Janke S, Wagner I, Schröder C, Streichert T, Bamberger A-M, et al. Role of Fra-2 in breast cancer: influence on tumor cell invasion and motility. Breast Cancer Res Treat 2008;107:337–47. https://doi.org/10.1007/s10549-007-9559-y.

[178] Sharma SV, Lee DY, Li B, Quinlan MP, Takahashi F, Maheswaran S, et al. A chromatin-mediated reversible drug tolerant state in cancer cell subpopulations. Cell 2010;141:69–80. https://doi.org/10.1016/j.cell.2010.02.027.

[179] Ma L, Hernandez MO, Zhao Y, Mehta M, Tran B, Kelly M, et al. Tumor Cell Biodiversity Drives Microenvironmental Reprogramming in Liver Cancer. Cancer Cell 2019;36:418-430.e6. https://doi.org/10.1016/j.ccell.2019.08.007.

[180] Yamanaka K, Petrulionis M, Lin S, Gao C, Galli U, Richter S, et al. Therapeutic potential and adverse events of everolimus for treatment of hepatocellular carcinoma – systematic review and meta-analysis. Cancer Med 2013;2:862–71. https://doi.org/10.1002/cam4.150.

[181] Iyer SS, Cheng G. Role of Interleukin 10 Transcriptional Regulation in Inflammation and Autoimmune Disease. Crit Rev Immunol 2012;32:23–63.

[182] El-Brolosy MA, Stainier DYR. Genetic compensation: A phenomenon in search of mechanisms. PLOS Genet 2017;13:e1006780. https://doi.org/10.1371/journal.pgen.1006780.

[183] Proia TA, Singh M, Woessner R, Carnevalli L, Bommakanti G, Magiera L, et al. *STAT3* Antisense Oligonucleotide Remodels the Suppressive Tumor Microenvironment to Enhance Immune Activation in Combination with Anti–PD-L1. Clin Cancer Res 2020;26:6335–49. https://doi.org/10.1158/1078-0432.CCR-20-1066.

[184] Lechner M, Lirk P, Rieder J. Inducible nitric oxide synthase (iNOS) in tumor biology: the two sides of the same coin. Semin Cancer Biol 2005;15:277–89. https://doi.org/10.1016/j.semcancer.2005.04.004.

[185] Cheng K, Cai N, Zhu J, Yang X, Liang H, Zhang W. Tumor-associated macrophages in liver cancer: From mechanisms to therapy. Cancer Commun Lond Engl 2022;42:1112–40. https://doi.org/10.1002/cac2.12345.

Acknowledgement

An dieser Stelle gebührt mein herzlichster Dank allen Menschen, die mich auf meinem Weg begleitet und unterstützt haben.

Mein ganz besonderer Dank gilt Prof. Dr. Dr. Detlef Schuppan, der mir die Möglichkeit gab, diese Doktorarbeit zu verwirklichen und mich herzlich in seiner Arbeitsgruppe aufnahm. Währenddessen unterstützte und förderte er mich nicht nur durch sein medizinisch-naturwissenschaftliches Fachwissen, sondern inspirierte mich auch, selbst Medizin zu studieren und stand mir bei diesem Vorhaben in besonderem Maße zur Seite.

Anschließend möchte ich mich bei Sebastian bedanken, der mich im ersten Jahr meiner Dissertation betreut hat. Seine sorgfältige Einführung in die Durchführung von Mausversuchen legte den Grundstein für meine experimentelle Arbeit. Außerdem danke ich ihm für die einzigartige Chance, als Nebenprojekt an seiner Publikation mitzuwirken. Zudem bedanke ich mich für seine Korrekturen und generell seinen stets tiefgreifenden fachlichen Input.

Besonderer Dank gilt Dr. Ernesto Bockamp, dessen Tür für mich stets offenstand und der mir mit wertvollen Ratschlägen zu laborexperimentellen und fachspezifischen Fragen jederzeit zur Seite stand.

Mein besonderer Dank gilt Herrn Prof. Dr. Thomas Hankeln, der sich freundlicherweise bereit erklärt hat, als Zweitbetreuer zu fungieren, sowie Herrn Prof. Dr. Walter Stöcker, der die Rolle des Zweitgutachters übernimmt.

Mein Dank gilt dem TARC und seinen Tierpflegern für ihre unverzichtbare Hilfe.

Meine Wertschätzung gilt allen - sowohl aktuellen als auch ehemaligen - Mitgliedern des TIMs, die eine großartige Arbeitsumgebung und unvergessliche Erinnerungen geschaffen haben. Besonderer Dank gilt dabei „The Surgeons“ Sandrine und Hicham, mit denen selbst die längsten OP-Tage zu einem echten Spaß wurden. Ein herzliches Dankeschön an Doro und Dominik für den wertvollen Wissensaustausch sowie die bereichernden und zugleich unterhaltsamen Momente, die unseren Arbeitsalltag so angenehm gemacht haben. Herzlichen Dank auch an Nicola und Johannes, meinen liebsten Office-Buddies und Topline-Researchern.

Von Herzen danke ich all meinen Freunden für ihre aufmunternden Worte und, wenn nötig, die willkommene Ablenkung während meiner Promotion. Ein besonderer Dank gilt dabei meinen Freundinnen Cinja, Dunja, Luisa und Nele, deren unermüdlicher Beistand entscheidend zur Fertigstellung dieser Arbeit beigetragen hat – mit euch ist alles „Nicht schlimm“! Ein riesiges Dankeschön auch an den Mainzer Stammtisch für die vielen schönen Abende.

Meiner Mama und meinem Bruder gilt mein tiefster Dank für ihre unendliche Unterstützung und Motivation – мы не привыкли отступать!

Curriculum Vitae

Emma Eichler

Personal Information

Date and Place of Birth: October 19, 1992 in Tumen, Russia
Address: Rheinallee 52, 55118 Mainz, Germany
Mobile: +49 17620662587
E-Mail: eeichler@uni-mainz.de

Education

Mar 2020 - Present | **Doctoral Studies (Dr. rer. nat.)**
University Medical Center Mainz, Institute of Translational Immunology
Dissertation title: The role of the tumor microenvironment in the progression of desmoplastic cancers in subcutaneous and orthotopic injection models

Oct 2021 - Present | **Medical Studies (Second Degree)**
Rheinische Friedrich-Wilhelms University of Bonn
First Medical Examination successfully completed in April 2025

Apr 2017 - Sept 2019 | **Master of Science in Biological Sciences**
Julius-Maximilian University of Würzburg
Focus: Cellular Oncology, Microbiology & Infection Biology
Thesis title: Generating knockout and point mutation cell models for two deubiquitinase genes that play an important role in the pathogenesis of Cushing´s disease using CRISPR/Cas9 technology (Grade: 1.0)

Oct 2013 - Dec 2016 | **Bachelor of Science in Biological Sciences**
Technische Universität Kaiserslautern
Thesis title: Characterization of two ferredoxin-dependent bilin reductases in *Galdieria sulphuraria* (Grade: 1.3)

Mar 2012 | **Abitur**
Hofenfels-Gymnasium, Zweibrücken

Skills & Qualifications

Animal Research: Translational Animal Research Center (TARC) Module 4 certified

Languages: German & Russian (native), English (good knowledge)

Computer Skills: Microsoft Office applications (advanced)

Conference Contributions

Jun 2024 | **Poster Presentation**
2nd Extracellular Matrix Pharmacology Congress, Copenhagen
A syngeneic and orthotopic HCC mouse model to demonstrate high efficacy of combination therapies that modulate the ECM and immune microenvironment

Jul 2023 | **Poster Presentation**
2nd International Symposium on Immune Evasion in Malignant & Chronic Infectious Diseases, Höhr-Grenzhausen
Novel mouse model for the specific knockout of TGFβRII in Cancer-associated fibroblasts

Jun 2022 | **Oral Presentation**
1st Extracellular Matrix Pharmacology Congress, Copenhagen
Novel mouse model for the specific knockout of TGFβRII in Cancer-associated fibroblasts

Publications

Kaps L, Huppertsberg A, Choteschovsky N, Klefenz A, Durak F, Schrörs B, Diken M, **Eichler E**, Rosigkeit S, Schmitt S, Leps C, Schulze A, Foerster F, Bockamp E, De Geest BG, Koynov K, Räder HJ, Tenzer S, Marini F, Schuppan D, Nuhn L. pH-degradable, bisphosphonate-loaded nanogels attenuate liver fibrosis by repolarization of M2-type macrophages. Proc Natl Acad Sci U S A. 2022 Mar 22;119(12)

Rosigkeit S, Kruchem M, Thies D, Kreft A, **Eichler E**, Boegel S, Jansky S, Siegl D, Kaps L, Pickert G, Haehnel P, Kindler T, Hartwig UF, Guerra C, Barbacid M, Schuppan D, Bockamp E. Definitive evidence for Club cells as progenitors for mutant Kras/Trp53-deficient lung cancer. Int J Cancer. 2021 Nov 1;149(9):1670-1682

Siegl D, Kruchem M, Jansky S, **Eichler E**, Thies D, Hartwig U, Schuppan D, Bockamp E. A PCR protocol to establish standards for routine mycoplasma testing that by design detects over ninety percent of all known mycoplasma species. iScience. 2023 Apr 26;26(5):106724.

Krüger S, **Eichler E**, Strobel L, Schubert-Unkmeir A, Johswich KO. Differential influences of complement on neutrophil responses to Neisseria meningitidis infection. Pathog Dis. 2018 Nov 1;76(8).

Mainz, April 2025

Statutory Declaration

I hereby confirm that I have authored this thesis independently, that I have not used other than the declared sources / resources, and that I have explicitly marked all material which has been quoted either literally or by content from the used sources. The thesis has not yet been presented to any other examination board in this or a comparable form.

Mainz, April 15, 2025

Emma Eichler